An improved and robust finite element model for simulation of cold-formed steel built-up beams

Harsh Hemant Birwadkar

A thesis submitted in fulfillment of the requirements

for the degree of Master of Engineering

Main supervisor: Dr. Zhiyuan (Arthur) Fang

Co-supervisors: Parsa Yazdi, Prof. James Lim, and Dr. Krishanu Roy

School of Engineering

The University of Waikato

New Zealand

THE UNIVERSITY OF
WAIKATO
Te Whare Wānanga o Waikato

2024

ABSTRACT

Cold-formed steel (CFS) built-up sections are increasingly utilized in structural applications due to their lightweight properties, high strength-to-weight ratio, and enhanced moment capacity, which can be further improved by adding stiffeners to the webs or flanges. Accurately determining the moment capacity of these sections is important for practical use. This can be achieved through experimental testing or finite element analysis (FEA) using a four-point bending setup. However, conducting full-scale experimental tests is both expensive and time-consuming, and developing a full-scale finite element (FE) model to replicate these tests can be computationally intensive.

To address these challenges, this study introduces an accurate, efficient, and robust numerical method that replicates the behaviour of CFS built-up sections, applicable to both back-to-back and face-to-face configurations. The proposed numerical methodology demonstrates excellent agreement with available test results in terms of moment capacity and failure modes, highlighting its potential for determining the moment capacity of built-up sections. The study further investigates two cross-sectional types—stiffened nested and unstiffened nested—to evaluate their behaviour and moment capacity.

The proposed simplified model was subsequently used in an extensive parametric study to determine the moment capacity of stiffened and unstiffened nested sections. Parameters considered in the study include varying section thicknesses (0.75 mm to 3.00 mm), web depths (150 mm to 600 mm), section configurations (nested and stiffened nested), and screw spacings (75 mm, 150 mm, and 300 mm). Given that existing design standards, such as those from the American Iron and Steel Institute (AISI 2016) and the Australian/New Zealand Standards (AS/NZS 2018), lack specific guidelines for calculating the moment capacity of these sections, this research aims to fill that gap. Furthermore, to simulate practical scenarios, models

incorporating screws in the webs (screw-web model) were developed and compared against the simplified model. The results of the parametric study revealed that the moment capacity of the built-up sections is significantly influenced by section thickness, web depth, and section configuration. Screw spacing, however, had a less significant impact. Notably, the moment capacity of the screw-web model was lower than that of the simplified model, emphasizing the importance of bimoment and warping deformation in connection design.

The study concludes that the developed simplified model provides a computationally efficient tool for predicting the moment capacity of built-up beams, offering valuable insights for designers and engineers. Additionally, the nested section configuration is recommended for achieving higher moment capacity compared to the stiffened nested section.

Keywords: Cold-formed steel, built-up beams, finite-element model, simplified model, moment capacity

PREFACE

This thesis is submitted to the University of Waikato, New Zealand, in partial fulfilment of the requirements for a master's degree in civil engineering. The work presented here has not been submitted for any degree or diploma at any other institution. To the best of my knowledge, this thesis contains no material previously published or written by others, except where proper citation is provided.

ACKNOWLEDGEMENTS

First and foremost, I extend my deepest gratitude to my main supervisor, Dr. Zhiyuan (Arthur) Fang, and my co-supervisors, Parsa Yazdi, Professor James B.P. Lim, and Dr. Krishanu Roy, for their unwavering support and guidance throughout my research journey. Their invaluable insights and mentorship have been instrumental in the successful completion of my thesis and have significantly contributed to my development as an independent researcher.

I am profoundly thankful to Shubham Tiwari and Dinesh Lakshmanan Chandramohan for their constant encouragement and unwavering support, which have been vital to my progress. I also wish to acknowledge the encouragement and support provided by Kushal Gosh and Bikram Paul, whose contributions have been a cornerstone of this journey.

My heartfelt appreciation goes to my friends and well-wishers in New Zealand, whose encouragement has been a source of strength throughout this endeavour. Special thanks to Maria Fe Glorieta B. Opulencia, Gagan Sengundham Dinesh, Gowrava Mohanswamy, Vivekanandan Sivaji, and Puviyarasan Velayudham for their unwavering support.

I owe a profound debt of gratitude to my family – my father, Hemant Birwadkar; my mother, Mansi Birwadkar; my cousin, Shrinivas Khedekar; and my extended family in New Zealand and India – whose unconditional love, encouragement, and support have been my foundation throughout this journey.

Lastly, I am grateful to the University of Waikato and the School of Engineering for providing the necessary computing resources and research assistance that enabled this work. Special thanks to Sophia Rodrigues for her invaluable help and assistance during laboratory testing, which played a crucial role in this research. Finally, I would like to extend my sincere thanks to Formsteel™ for their generous support in providing the samples required for this study.

NOTATION

Cold-Formed Steel	CFS
Face-To-Face	FTF
Back-To-Back	BTB
American Iron and Steel Institute	AISI
Australian and New Zealand Standards	AS/NZS
Finite element	FE
Finite element analysis	FEA
Finite element modelling	FEM
Direct Strength Method	DSM
Effective Width Method	EWM
Genetic algorithms	GA
Hot Rolled Steel	HRS
Cross-section	C/S
Young's modulus	E
True stress	σ_t
True strain	ε_t
Engineering stress	σ_e
Engineering strain	ε_e
Megapascal	MPa

Kilo-Newton Metre	kN · m
Kilo-Newton	kN
Millimetres	mm
Metre	m
Thickness	t
Yield stress	f_y
Local buckling stress	f_{ol}
Distortional buckling stress	f_{od}
Imperfection magnitude for local buckling	S_{ol}
Imperfection magnitude for distortional buckling	S_{od}
Reference point	RP
Radius	R
Length	l
Screw spacing	s
Moment capacity from FEA	M_{FEA}
Elastic lateral-torsional buckling moment	M_o
Yield moment	M_y
Nominal member moment capacity for lateral-torsional buckling	M_{be}
Nominal member moment capacity for local buckling	M_{bl}
Non-dimensional slenderness used to determine M_{bl}	λ_l

Nominal member moment capacity for distortional buckling	M_{bd}
Non-dimensional slenderness used to determine M_{bd}	λ_d
Elastic local buckling moment	M_{ol}
Elastic distortional buckling moment	M_{od}
Buckling resistance moment	$M_{b,Rd}$
Reduction factor for lateral-torsional buckling	χ_{LT}
Partial factor for resistance of members to instability	γ_{M1}
Elastic critical moment for lateral-torsional buckling	M_{cr}

TABLE OF CONTENTS

LIST OF FIGURES

LIST OF TABLES

Chapter 1 – Introduction

1.1 Background

In recent decades, the use of cold-formed steel (CFS) sections in structural applications has gained significant popularity due to their numerous advantages over hot-rolled steel (HRS). These benefits include lightweight construction, recyclability, a high strength-to-weight ratio, durability, ease of installation, and greater flexibility in manufacturing a variety of cross-sectional profiles and sizes [1-3] . However, Meza et al. reported that due to their thinner walls, the ultimate capacity of CFS members is often limited by phenomena such as local and distortional buckling, sometimes in conjunction with global buckling [3]. Therefore, joining sections through welding or fasteners provides a practical solution, allowing for the creation of built-up sections with various cross-sectional geometries, as illustrated in Figure 1-1. These built-up sections offer significant advantages, such as reducing susceptibility to certain buckling modes, enhancing torsional resistance, and doubling the moment capacity compared to single-channel sections.

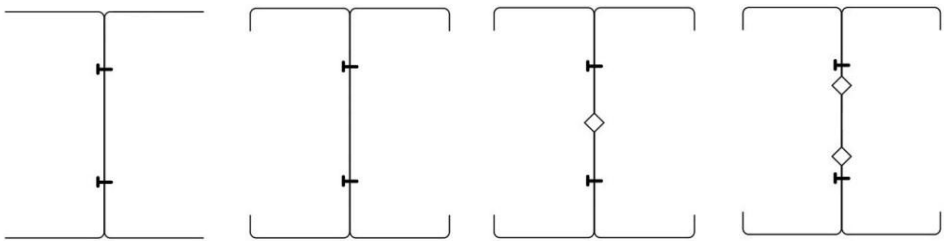

(a) Different cold-formed BTB built-up sections

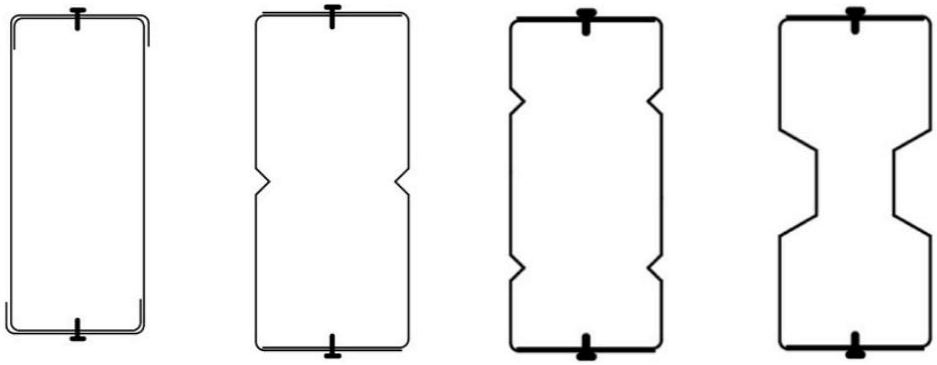

(b) Different cold-formed FTF built-up sections

Figure 1-1: Examples of built-up sections [4].

Moreover, the use of such built-up beams is common in lightweight portal frames, as shown in Figure 1-2. A typical practice involves fabricating rafters and columns by connecting two channel sections back-to-back (BTB), creating a doubly symmetric cross-section with enhanced capacity [5-8]. Similarly, face-to-face (FTF) built-up sections provide greater moment capacity compared to single-channel sections.

(a) Beam-column connection (b) CFS built-up sections used for portal frames

Figure 1-2: Portal frames made by Formsteel™ [7].

1.2 Problem statement

With the increasing demand for strength, built-up sections have become more popular than single-channel sections. However, due to the complex geometrical configurations of built-up beam sections, it is crucial to determine their moment capacity before on-site implementation. Typically, this requires either experimental testing or finite element analysis (FEA). Experimental methods face challenges such as logistical issues, ensuring accurate setups, and the potential for human error. Likewise, modelling the entire test setup in FE software requires careful attention, calibration, and considerable computational resources.

Currently, no alternative methods have been proposed to address these challenges. Therefore, a robust and computationally efficient approach must be developed to reduce computational demands and accurately predict the moment capacity of complex FTF and BTB built-up sections.

1.3 Aim and scope of this research

Specific objectives of this work are listed below:

1. To develop nonlinear FE models that simulate the structural behaviour of CFS built-up beams under four-point bending. These FE models will be developed based on the measured cross-section dimensions and material properties reported in the literature, with geometric imperfections incorporated according to the literature and design guidelines. The FE models will then be validated by comparing them to the failure modes and moment capacities obtained from experimental tests documented in the literature.
2. The validated FE model will be used to develop a computationally efficient simplified model that replicates the failure modes and moment capacities of the built-up section. To verify its accuracy, the simplified model will be compared with the experimental results reported in the literature and the full four-point bending FE model.
3. The validated simplified FE model will be employed to conduct an extensive parametric study. Investigating the influence of various factors such as web depth, thickness of the sections, screw spacing, and the arrangement of single channel sections in a built-up section on the moment capacity under bending.
4. To recommend the most effective design shape among the stiffened nested and nested built-up beams studied, based on the results of the parametric study.

1.4 Outline of the thesis

The thesis is structured into the following six chapters:

Chapter 1 provides a brief overview of the background, problem statement, aim, and scope of the research, along with an outline of the thesis.

Chapter 2 provides a comprehensive review of prior studies on CFS single-channel sections, built-up box sections, and optimisation techniques and algorithms applied to concrete structures, HRS, and CFS. The literature review on CFS built-up beams reveals a lack of specific guidelines for determining the moment capacities of these sections in both FTF and BTB configurations. Furthermore, despite the growing use of built-up beams, researchers have yet to develop a simplified or optimised approach for determining their moment capacity.

Chapter 3 offers a brief overview of the modelling technique used to develop the FE model for a four-point bending test setup. Additionally, the FE model was validated against the test results reported by Dai et al. [7], showing that the moment capacity and failure mode of the developed FE model closely matched the experimental results.

Chapter 4 details the procedure used to simplify the four-point bending model. The process began by reducing the four-point model to a pure bending model, which was then further simplified. The FE results for both the pure bending and simplified models showed strong agreement with the FE results of the four-point bending model presented in Chapter 3, as well as the experimental data. Additionally, the study was extended to develop a model simulating a beam-column or beam-beam connection, aimed at determining the actual strength of built-up sections in connections.

Chapter 5 outlines the application of the developed simplified model to various configurations of BTB and FTF built-up sections.

Chapter 6 presents a parametric investigation involving 190 models featuring two types of built-up sections: stiffened nested and nested sections. The study considered parameters including thicknesses ranging from 0.75 to 3.00 mm, screw spacings of 75, 150, and 300 mm, and web depths varying from 150 mm to 600 mm. Based on the parameters studied, conclusions were drawn regarding the following aspects: the impact of changes in web depth (w_d), the effect of section thickness (t), the positioning of the single-channel section within the built-up section, screw spacing (s), and the placement of screws along the web in the longitudinal direction.

Chapter 7 provides a concise summary of the thesis, along with detailed conclusions based on the parametric study and the influence of various parameters. It also addresses the limitations of the current study and offers recommendations derived from the findings. Furthermore, the chapter discusses potential future research directions related to this work.

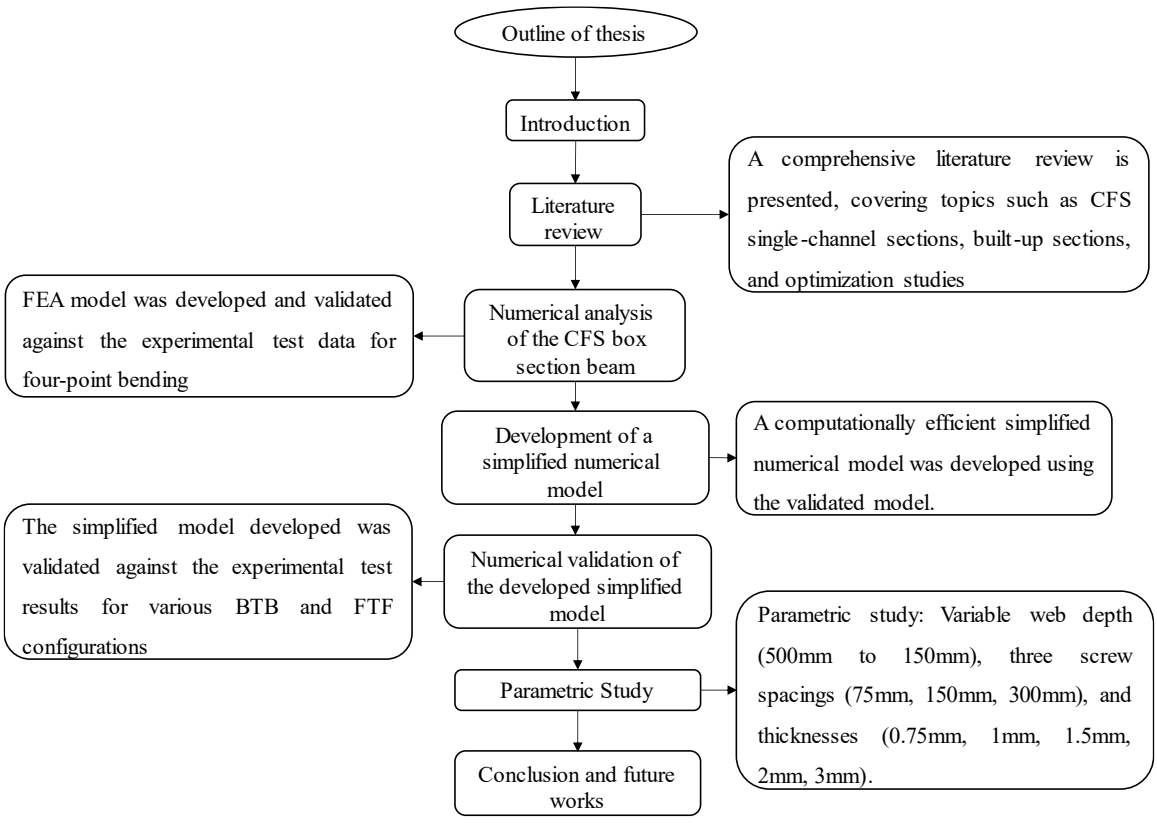

Figure 1-3: Flowchart for the outline of the thesis.

Chapter 2 – Literature Review

2.1 Introductory remarks

This chapter provides a thorough literature review on the behaviour of CFS built-up beams under bending. The review is divided into five primary sections, addressing the behaviour of CFS single channel sections, built-up sections, optimisation studies, and parametric studies. The review highlights a gap in the existing literature regarding the influence of various parameters on moment capacity, underscoring the limited research dedicated to developing a simplified model for determining the moment capacity of built-up beams under bending.

2.2 Previous studies on behaviour of CFS single channel section under bending

Numerous studies in the literature have examined the moment capacity of CFS channel sections. Chen et al. [8] conducted a comprehensive investigation utilizing both experimental and numerical analyses on the moment capacity of cold-formed channel beams, considering various configurations such as edge-stiffened web holes (Figure 2-1 (a)), un-stiffened web holes (Figure 2-1 (b)), and plain webs. The study reported a total of 215 results, including 16 four-point bending tests and 199 FEA simulations. A parametric study was conducted for varying beam lengths, fillet radius, stiffener length, and hole diameter. The study showed that the edge-stiffened web holes increases the moment capacity whereas the unstiffened web holes decreases the moment capacity with respect to plain channel sections.

The study evaluated the precision of design guidelines according to AISI-2016 [9] and AS/NZS 4600:2018 [10] by comparing test and FEA results with the calculated moment capacities for CFS channel beams without web holes. These standards accurately predicted the moment capacity for such beams. In contrast, for CFS channel beams with web holes, the

design equations by Moen and Schafer [11] were found to be overly conservative for beams with un-stiffened and edge-stiffened web holes, respectively.

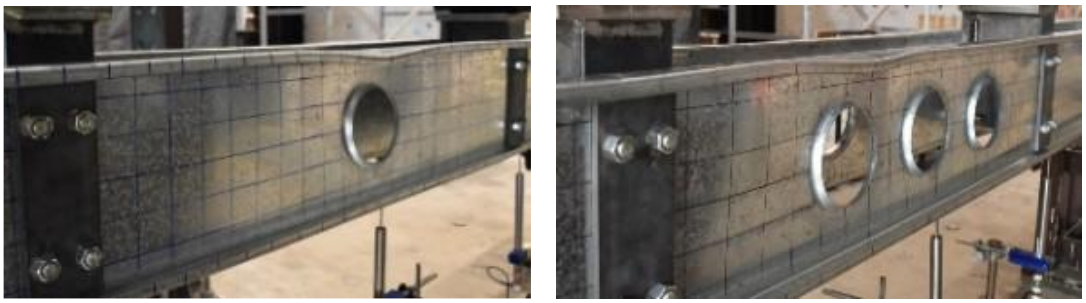

(a) Edge stiffened web holes

(b) Unstiffened web holes

Figure 2-1 Failure modes of CFS channel beams with holes under bending [8].

Moen et al. [14-15], Zhao et al. [13], Yu et al. [17-18], and Thirunavukkarasu et al. [16] conducted experimental and numerical research that introduced the Direct Strength Method (DSM) for developing equations to determine the moment capacity of CFS channel sections. Their work provides key insights into the structural behaviour of these sections with unstiffened circular web holes. Building on this foundation, Degtyareva et al. [20-21] investigated how unstiffened slotted web holes affect moment capacity.

Although existing research extensively covers CFS channel sections with unstiffened circular web holes, there is a significant lack of studies on sections with edge-stiffened circular web holes subjected to four-point bending. Chen et al. [8], Yu [19], and Dai et al. [20] have addressed this gap through a combination of experimental and numerical investigations,

revealing that sections with edge-stiffened circular web holes exhibit enhanced moment capacity compared to those with plain webs.

2.3 Previous studies on CFS built-up box sections under bending

Chea et al. [21] conducted thorough testing involving 16 full-scale experiments under four-point bending conditions. Their investigation encompassed several parameters including thickness, connection spacing, web height, and flange width-to-thickness ratio. Subsequently, the test outcomes as shown in Figure 2-2 were verified through FEA modelling, revealing a variation of -14% to +12% when compared with the experimental results. Additionally, they concluded that increasing the section thickness and screw spacings would lead to an increase in the flexural capacity of beam.

Figure 2-2: Four-point bending test on built-up beam [21].

In 2017, Wang and Young [22] presented a numerical investigation aiming to determine the moment capacities of CFS built-up sections featuring circular web holes under four-point bending. They developed FE analysis models for three section types: I-sections, BTB sections, and FTF sections connected at the lips. For simulating screw connections and reducing computational time, they adopted a simplified method where tie constraints were applied between connected nodes. Their findings indicated that FEA accurately predicted test results depicted in Figure 2-3. They also found that web holes had a more pronounced effect on beam

strengths in built-up closed sections compared to built-up open sections. Additionally, they observed that while the DSM formulae in the North American Specification [23] accurately predicted the design strengths for built-up open-section beams with holes, these formulae were somewhat conservative for closed-section beams with holes.

Figure 2-3: Four-point bending test with experimental and numerical analysis [22].

In 2018, Wang and young [24] conducted an experimental (shown in the Figure 2-4) and numerical study on CFS built-up beams, examining both BTB and FTF connections. They subjected a total of 35 sections to four-point bending tests, employing various screw arrangements with self-tapping screws. Their findings indicated that FE models effectively predicted experimental outcomes across different screw arrangements. Moreover, they validated both FEA and test results against DSM outcomes. Finally, they highlighted that the spacing of screws significantly influenced the moment capacities of built-up closed sections, furthermore, they proposed modified DSM equations for local buckling failure since the design strengths determined by AISI-2016 [9] were found to be conservative.

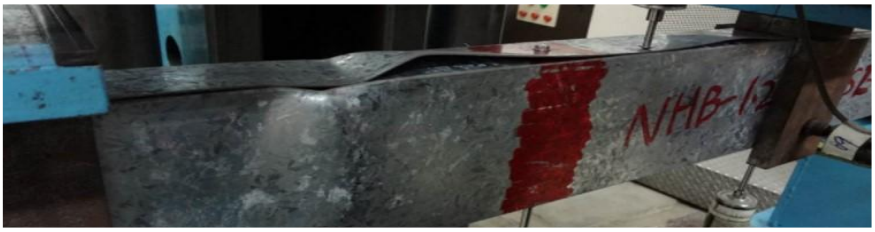

Figure 2-4: Four-point bending test with experimental and numerical analysis on the built-up beam [24].

Wang and Young [25] in 2016, carried out an extensive study on built-up sections under four-point and three-point bending in which the sections were assembled with self-tapping screws either located in flanges or webs. In this study, the experimental results were validated with FEA models accompanied by a parametric study which was further validated with DSM according to North American Specification [23]. The FE and experimental results were found in good agreement in terms of the ultimate moment and failure modes. Furthermore, they also concluded that there was no failure in the screws. Finally, they carried out a reliability analysis to verify the reliability of the design equations which they have proposed in their paper.

In 2019, Anbarasu [26] conducted a numerical investigation (Figure 2-5) based on the experimental tests performed by Wang and Young [25] to validate the accuracy of FEA predictions. Additionally, Anbarasu utilized a similar modelling technique to conduct an extensive parametric study under four-point bending, comprising 114 models, which were subsequently validated with DSM predictions. Anbarasu's findings indicated that the modified DSM equations proposed by Wang & Young [25] underestimated the flexural strength of CFS built-up beams comprised of sigma sections. Considering both current design standards and the proposed equations by Wang & Young [25], Anbarasu suggested alternative equations that are deemed more reliable and safer. Lastly, Anbarasu suggested that further calibrations could enhance the design equations.

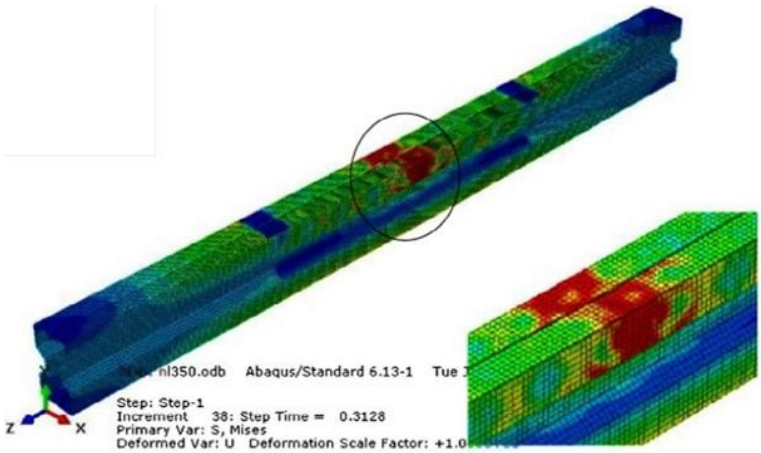

Figure 2-5: Numerical simulation of four-point bending test on built-up beam [26].

In 2024, Dai et al. [7] conducted experimental and numerical analyses on CFS built-up box beams under four-point bending, performing 13 full-scale tests to determine the moment capacities of novel CFS sections with identical stiffened channels joined by self-tapping screws. The tests involved sections with web depths of 270mm and 500mm and thicknesses of 1.15mm and 1.95mm. Measurements of local and global geometric imperfections were taken, and the experimental setup included lateral restraints and a spreader loading beam to apply load. Three beam lengths were examined: 3000mm, 4000mm, and 5000mm. Results showed that the deeper sections (500mm) had higher flexural capacity than shallower sections (270mm), largely due to their larger cross-sectional area and thickness. Screw spacing effects varied across different cross-sections, and increased restrained lengths reduced flexural capacity.

To validate the experimental results, Dai et al. [7] developed a nonlinear elastoplastic FEA model. A parametric study with 200 models examined variables like section thickness, screw spacing, and unrestrained length. Findings indicated section thickness significantly impacts flexural capacity, with deeper sections more sensitive to thickness changes. Screw spacing beyond 300mm had minimal effect on flexural capacity. Comparisons with DSM predictions revealed conservative estimates for local buckling but unconservative for global buckling, prompting Dai et al. [7] to propose new predictive equations. Reliability analysis confirmed these new equations' accuracy. Overall, FEA was found to accurately predict experimental, emphasizing section thickness over screw spacing in influencing flexural capacity.

Figure 2-6: Four-point bending test [7].

2.4 Previous studies on optimisation

2.4.1 Summary of optimisation studies on concrete structures

Various optimisation techniques have been applied to enhance the design and cost-efficiency of reinforced concrete structures. Sahab et al. [27] utilized a hybrid algorithm combining genetic algorithms (GA) and the Hook and Jeeves method to optimize construction costs in flat slab buildings. Kohoutkova and Broukalova [28] optimized fibre-reinforced concrete (FRC) mixtures to improve structural performance. Eleftheriadis et al. [29] integrated BIM with a multi-objective GA to optimise cost and carbon emissions in structural design. Afshari et al. [30] compared six multi-objective optimization algorithms for RC beams, identifying derivative-free optimisation as the most effective. Whitworth et al. employed GA to minimize embodied energy in composite floor plates. Pierott et al. [31] used a GA-based model to optimise reinforced concrete beam dimensions and reinforcement layouts, achieving significant cost reductions.

2.4.2 Optimisation study on retrofitting of HRS sections to CFS sections

In 2023, Chobe et al. [32] conducted a numerical study, illustrated in Figure 2-7, to explore how retrofitting Hot-Rolled Steel (HRS) with Cold-Formed Steel (CFS) can improve the torsional rigidity of structural members and reduce Lateral-Torsional Buckling (LTB). They first validated their experimental results with finite element (FE) modelling before performing

a parametric study involving 600 models with varying CFS channel thicknesses, intermediate spot weld spacings, slenderness ratios, and cross-sectional dimensions of the HRS beam. Using a Machine Learning (ML) technique known as Symbolic Regression (SR), they developed an equation to predict the increase in moment capacity based on these parameters. The study offers a straightforward design approach for selecting the appropriate CFS channel thickness and spot weld spacing to achieve the desired moment capacity improvement. Furthermore, the ML method highlighted the benefits of using GA for analysing complex structural engineering problems to find optimal design solutions.

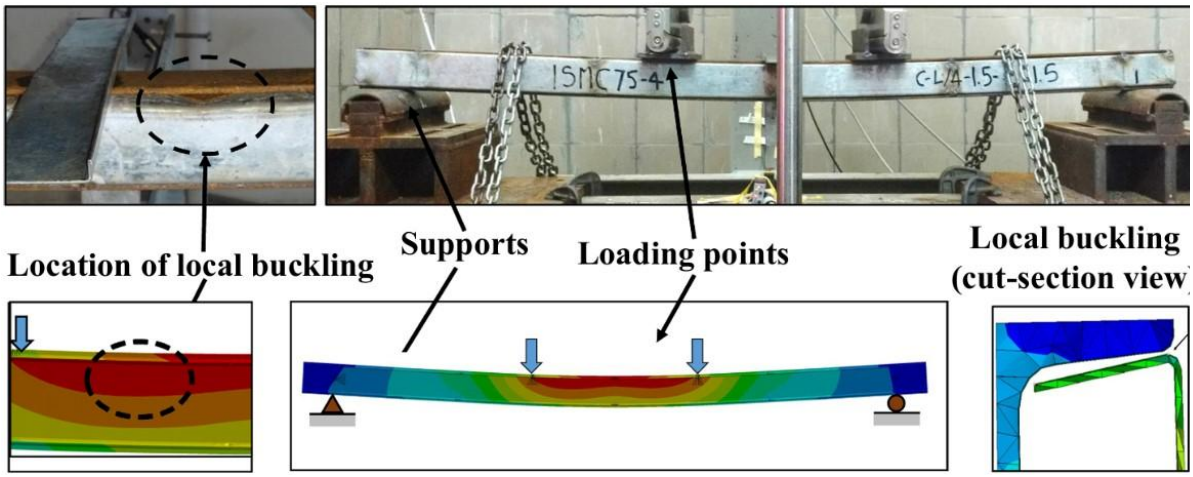

Figure 2-7: Comparison of the experimental and FEA results [32].

2.4.3 Previous studies on optimisation of CFS structures

In 2022, Liang et al. [33] presented a review paper that examined 160 studies on methodologies for the structural optimisation of CFS members and the thermal performance of CFS sections. The review concluded that numerous studies focus on optimising the cross-sections of CFS members, which included single channel sections, FTF sections, BTB sections, and gapped BTB sections, as shown in Figure 2-8, to enhance their structural performance. These studies incorporate various constraints to simulate real-world conditions and consider different loading scenarios. The review also found that GA are the most adopted optimisation algorithm for CFS structures.

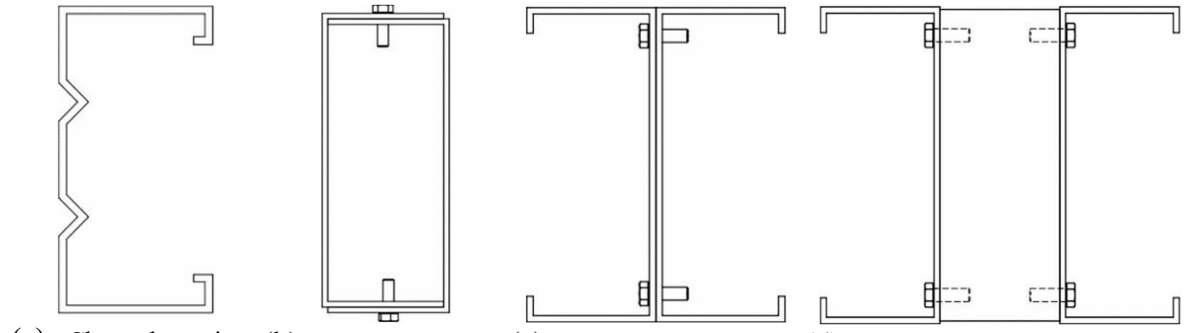

(a) Channel section with two web stiffeners and return lips (b) FTF connected box-section (c) BTB built-up I-section (d) BTB gapped channel sections

Figure 2-8: Optimal sections developed by Liang et al [33].

In 2019, Mojtabaei et al. [34] conducted a study to optimize the shape of a single channel section under Serviceability Limit State (SLS) and Ultimate Limit State (ULS) loading conditions, aiming to maximize flexural capacity and minimize deflection using the Big Bang and Big Crunch (BB-BC) optimisation methodology. The study evaluated 12 CFS cross-sectional prototypes under both SLS and ULS conditions. FEA, accounting for material non-linearity and initial geometric imperfections, was performed for each case and the results were compared to those from Eurocode-3 [35]. The study concluded that ULS optimisation yielded less efficient results than SLS for single-channel sections. Additionally, incorporating intermediate stiffeners in the web did not significantly improve performance, whereas adding stiffeners in the flange resulted in notable improvements.

In 2016, Ye et al. [36] conducted a comprehensive investigation on the practical optimisation of CFS beams using a PSO method. The optimisation methodology included material, section, manufacturing, and design constraints. Six different CFS channels were selected for optimisation based on flexural strength, as determined by the effective width-based provisions of Eurocode 3 [35]. This led to significant improvement in the flexural strength of sections (Figure 2-9) considering the same amount of material suggesting the robustness of optimisation methodology for practical applications.

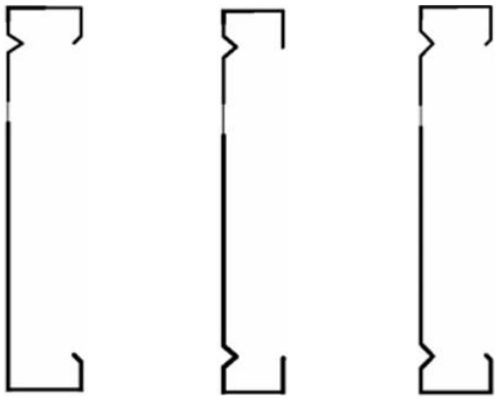

*The bold lines indicate the effective part of the sections

Figure 2-9: Optimal cross-sections of beams [36].

In 2019, Parastesh et al. [37] conducted a study to optimize symmetric Cold-Formed Steel (CFS) beam-column members for improved moment capacity using Genetic Algorithms (GA). They chose symmetric sections to avoid geometric impracticalities, suitable for both FTF and BTB configurations. The optimization process incorporated various manufacturing and construction constraints. A total of 132 beam-column sections were optimized considering three factors: eccentric loading for pure compression and bending, element length, and the complexity of cross-section shapes. Strengths for compression and bending moments were evaluated using the DSM with CUFSM software, accounting for local, distortional, and global buckling modes. The findings revealed that more complex shapes did not necessarily yield better design solutions. Increased eccentricity typically led to a broader range of optimal sections, particularly when distortional buckling was the dominant mode in short and intermediate-length beam columns, as shown in Figure 2-10.

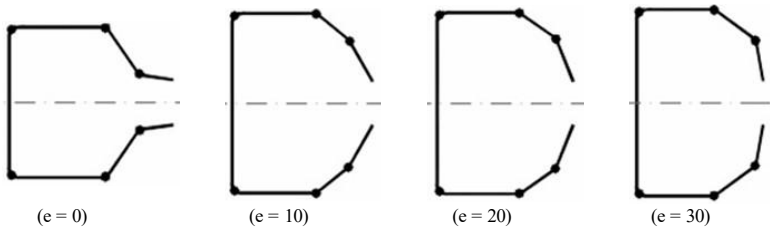

*e = eccentricity

Figure 2-10: Optimised sections for different eccentricities [37].

In 2022, Laím et al.[38] conducted a study focused on optimizing closed built-up CFS sections under compression. They developed a framework that combined FEM and PSO algorithms. To achieve an optimal solution, they considered three parameters: the height, thickness, and length of the built-up section. The study offered design predictions for the optimal columns using both the European Code and the North American Specification, and these predictions were compared with numerical results. The findings emphasized the impact of different parameters—such as steel thickness, cross-section height, and column length—on the optimal solution of the studied objective function, which was the resistance-to-weight ratio. Among these parameters, steel thickness was found to have the most significant influence.

In 2021, Mojtabaei et al. [39] developed a practical methodology for optimizing Cold-Formed Steel (CFS) beam-column members of varying lengths and thicknesses, subjected to different axial compression and bending moment combinations, while maintaining consistent material usage. They used a Genetic Algorithm (GA) to maximize the resistances of CFS members according to Eurocode 3 [35]. The optimization began with six prototype cross-sections, including both single (Figure 2-11-a) and built-up (Figure 2-11-b) channel sections, with variations allowed in their dimensions and edge stiffener configurations. Standard commercially available single and BTB-lipped channel sections were used as benchmarks to evaluate the efficiency of the optimized sections. The study demonstrated notable improvements in capacity over the initial cross-sections and provided insights into the material efficiency achievable with different cross-sectional shapes under combined loading conditions, ranging from pure bending to pure compression.

(a) Single channel sections (b) Built-up sections

Figure 2-11: Different geometries of section used by Mojtabaei et al [39].

In 2020, Phan et al. [40] presented an optimisation study carried out with a combination of FEA and GA. The primary objective of the study was to demonstrate an alternative analytical design approach using EWM Eurocode 3 [35]. The parameters considered for the optimisation included three different bolt group lengths, variable beam lengths (refer Figure 2-12), and variable plate thicknesses. The study concluded that a shorter bolt-group length can decrease the flexural strength of Cold-Formed Steel (CFS) bolted connections, whereas a longer bolt-group length typically results in a moment capacity close to the flexural strength of the CFS channel section.

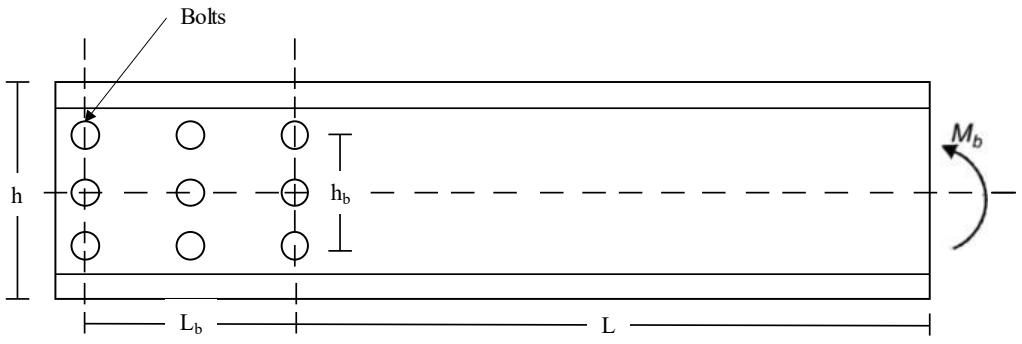

*h = web depth; h_b = depth of bolt group; L = beam length; L_b = length of bolt group

Figure 2-12: Representation of bolt assembly [40].

In 2021, Mojtabaei et al. [41] presented an optimisation framework aimed at developing more efficient CFS bolted moment connections with enhanced energy dissipation capacity and

ductility. To achieve this, a PSO algorithm was linked to ABAQUS for finite FE analysis, incorporating experimentally validated FE models of the connections. Five different CFS beam cross-sectional shapes were selected, with key design variables including their relative dimensions, the location of intermediate stiffeners, and the inclination of the lip stiffeners as shown in Figure 2-13.

The results indicate that adjusting the relative dimensions of the lipped-channel beam section can enhance the flexural strength, energy dissipation capacity, and ductility of connections compared to conventional lipped-channel beam sections. However, optimizing the angle of the lips yields only minimal improvements in structural performance. Additionally, the study found that optimizing Cold-Formed Steel (CFS) bolted moment connections under cyclic loading produces the same optimal sections and trends in energy dissipation and ductility as those achieved under monotonic loading. This suggests that effective optimization under monotonic loading can reduce computational costs while achieving similar performance outcomes.

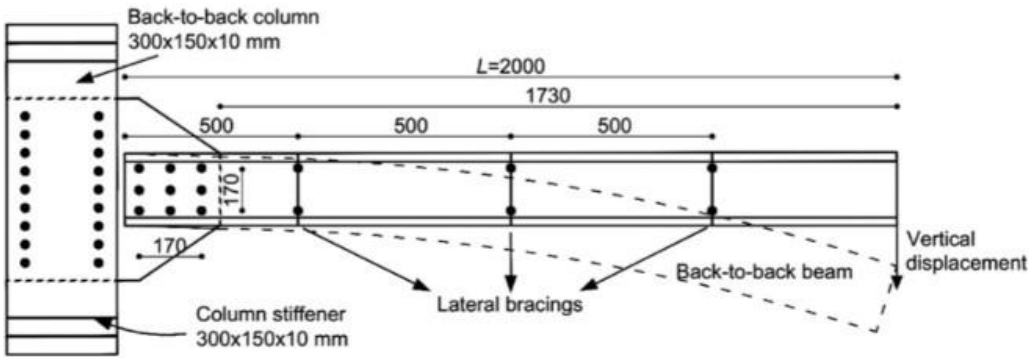

Figure 2-13: Schematic of bolted moment connection used in the optimization process [41].

In 2024, Qadir et al. [42] presented a study focused on optimising the flexural strength of cold-rolled steel sections through experimental testing, FEM, and design optimization. FE models, validated against experimental data from four-point beam bending tests, showed strong

agreement in ultimate moment capacities and load-displacement curves. The optimisation aimed to quantify the effects of geometry and cold working, proposing optimal designs that resulted in significant improvements. The study found that cold working significantly increased the ultimate strength of optimized sections. The optimisation process led to substantial enhancements in both distortional buckling and ultimate strength, achieving increase for both channel sections, and for zed sections (Refer Figure 2-14) compared to standard sections.

The inclusion of flange stiffeners greatly enhanced the flexural strengths of the sections. The optimisation process highlighted the critical impact of stiffener geometry and cold working on flexural strength, suggesting that these factors should be carefully considered in the design process for optimal performance. In conclusion, the study provided a comprehensive approach to optimizing the flexural strength of cold-rolled steel sections by integrating experimental testing, FE modelling, and optimisation techniques. The findings emphasized the significant benefits of including stiffeners and considering cold working effects, leading to substantial improvements in structural performance.

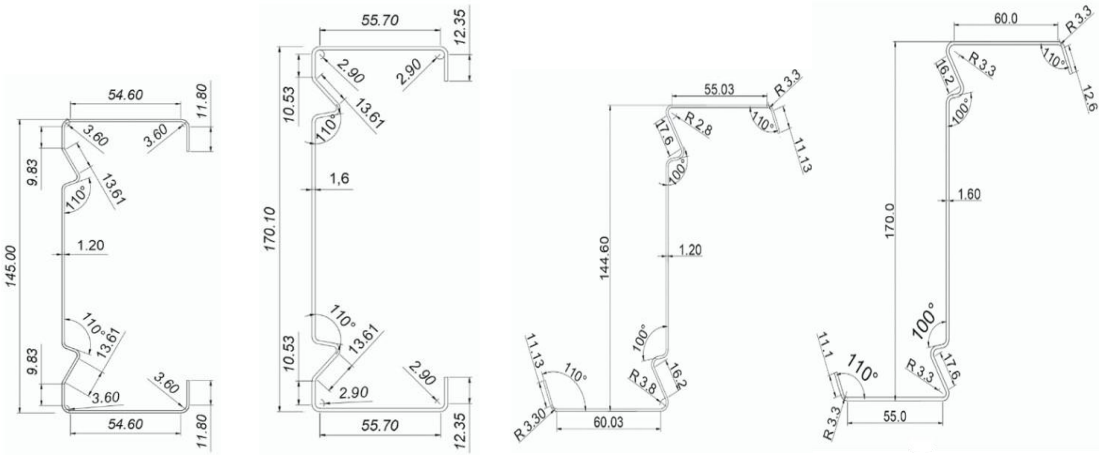

(a) Channel section (b) Zed section

Figure 2-14: Cross-section used by Qadir et al [42].

2.5 Design standards

2.5.1 Effective width method

The Effective Width Method (EWM), as specified in Eurocode 3 [35] and AS/NZS (2018) [10], is used to determine the design strengths of cold-formed built-up members. The method is based on the concept that the cold-formed elements near the corners of the cross-section are the key load-bearing parts of the entire section. This cross-section comprises several components, such as the web, flange, and lip. The empirical effective width of each element is determined using reduction factors that depend on the geometric properties of the cross-section and other general properties. Once these effective widths are established, the effective cross-sectional area can be calculated, which is essential for determining the member capacities. However, the method requires considering multiple parameters, making it very difficult to use. The formulae for determining the moment capacity of the built-up beams are provided in Table 2-1. [4]

2.5.2 Direct Strength Method

A widely adopted method for determining the member strengths of cold-formed members in the AISI (2016) [9] and AS/NZS (2018) [10] design standards is the Direct Strength Method (DSM), with the relevant equations provided in Table 2-1. The DSM, as recommended by AISI (2016) [9] and AS/NZS (2018) [10], has gained significant popularity in recent years. Unlike the EWM, where individual effective coefficients must be calculated for each element to determine the effective width, the DSM relies on gross-sectional properties to assess member strength. This makes DSM a more computationally efficient option compared to other design methods. Moreover, DSM accounts for the effect of fastener spacing, resulting in more accurate calculations. [4]

Table 2-1: Equations from current design guidelines

Standard code	Year	Equations
AISI [9] & AS/NZS [10]	2016 & 2018	Lateral-torsional buckling: For $M_o < 0.56M_y$, $M_{be} = M_o$ For $0.56M_y \leq M_o \leq 2.78M_y$, $M_{be} = \frac{10}{9} M_y \left(1 - \frac{10M_y}{36M_o}\right) \lambda_d \leq \lambda_{d2}$ For $M_o > 2.78M_y$, $M_{be} = M_y$ Local buckling: For $\lambda_l \leq 0.776$, $M_{bl} = M_{be}$ For $\lambda_l > 0.776$, $M_{bl} = \left[1 - 0.15 \left(\frac{M_{ol}}{M_{be}}\right)^{0.4}\right] \left(\frac{M_{ol}}{M_{be}}\right)^{0.4} M_{be}$ Distortional buckling: For $\lambda_d \leq 0.673$, $M_{bd} = M_y$ For $\lambda_d > 0.673$, $M_{bd} = \left[1 - 0.22 \left(\frac{M_{od}}{M_y}\right)^{0.5}\right] \left(\frac{M_{od}}{M_y}\right)^{0.5} M_y$
Eurocode – 3[35]	2006	Flexural strength: $M_{b,Rd} = \frac{\chi_{LT} W_{eff} f_y}{\gamma_{M1}}$ $\chi_{LT} = \frac{1}{\varphi_{LT} + \sqrt{{\varphi_{LT}}^2 - {\overline{\lambda}_{LT}}^2}}$ $\overline{\lambda}_{LT} = \sqrt{\frac{A_{eff}\, f_y}{M_{cr}}}$

2.6 Summary of previous parametric studies

In 2021, Kartik and Anbarasu [43] carried out an extensive parametric study on 108 FE models made up of cold-formed ferritic stainless steel (CFFSS) closed built-up beam composed of lipped channel sections orientated FTF using FEA software ABAQUS [44]. Before carrying out the parametric study a numerical validation for four-point bending was carried out with the available experimental test data. The parameters taken into consideration were thirteen different sections, with varying plate slenderness, using two different materials, with three different material properties and wall thicknesses as presented in Table 2-2.

Table 2-2: Parameters considered by Kartik and Anbarasu [43].

Sr. No.	Parameters
1	Thirteen different cross-sections with variable web depth (H), flange width (B), depth of lip (D_{lip})

Sr. No.	Parameters
	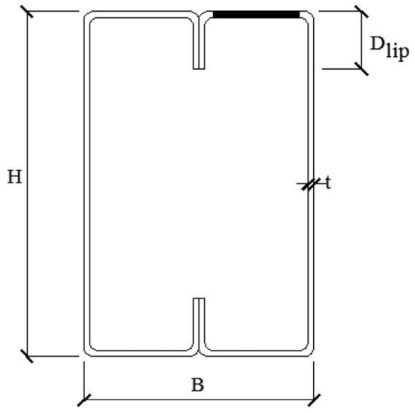
2	Three different thicknesses (t): 1.0mm, 1.6mm, 2.0mm
3	Three different material grades

In 2019, Roy et al. [45] conducted a study on the experimental and numerical analysis of the axial capacity of CFS built-up box sections. They validated their experimental test results by creating Nonlinear FE models in ABAQUS [44]. Following validation, they conducted a numerical parametric study on 148 models to examine the impact of fastener spacing on the axial capacity of built-up CFS box sections. The study considered two different cross-sections as shown in Table 2-3, varied the number of fasteners (3, 5, and 10), and included column lengths ranging from stub (300 mm) to slender (2000 mm) to cover a wide range of slenderness.

Table 2-3: Parameters considered by Roy et al. [45].

Sr. No.	Parameters
1	Two different cross-section properties with variable web depth (w_d), flange width (b_f), depth of lip (c), thickness (t), and radius of curvature (R)

Sr. No.	Parameters
	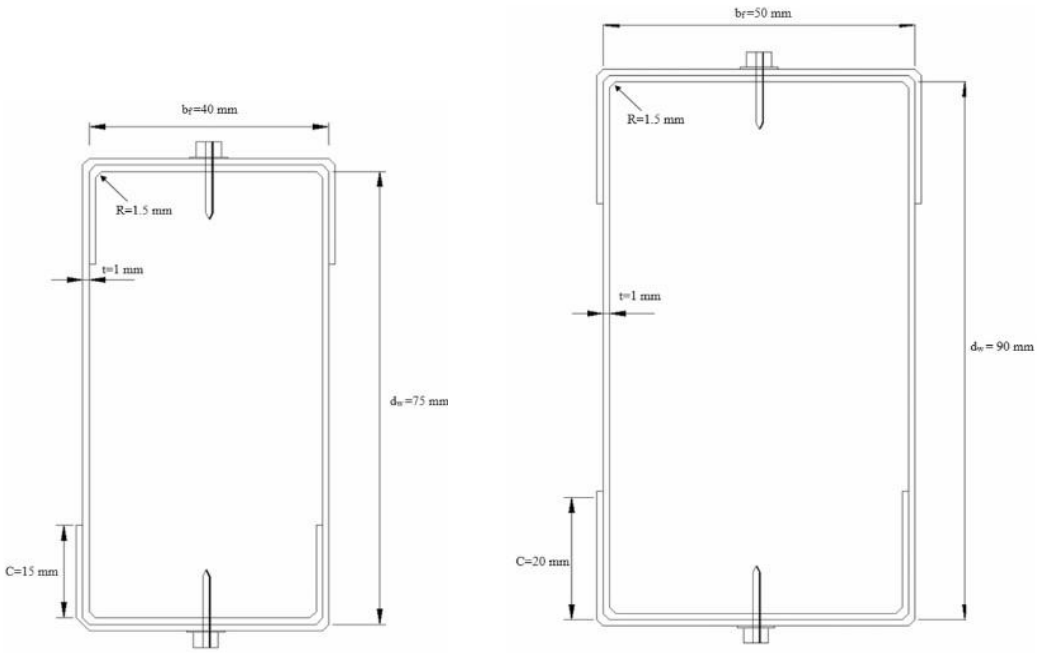
2	Number of fasteners: 3, 5, and 10
3	The length of the column varied from: 300, 500, 1000, and 2000mm

In 2023, Dai et al. [46] conducted a study on the web crippling resistance of CFS box sections through both experimental and numerical modelling and proposed a deep belief network. To validate the test results, FE models were developed, and these validated models were subsequently used for a parametric study. The FEA revealed that the web crippling resistance showed negligible difference whether actual screws were modelled, or connector elements were used. Consequently, connector elements were used for the parametric study. The study investigated the effects of section thickness, yield strength, bearing length, and screw spacing on the web crippling resistance of stiffened box sections under interior-two-flange (ITF) and end-two-flange (ETF) loading conditions as shown in Table 2-4.

Table 2-4: Parameters considered by Dai et al. [46].

Sr. No.	Parameters
1	Two different cross-sections (Refer to the image below)
2	Variable section thickness from 0.95mm to 2.95mm
3	Yield strength varied from 350 MPa to 450 MPa.
4	Ratio of beam length to flange width varied from 0.5 and 3.0.
5	Screw spacing was studied from 25mm to 500mm

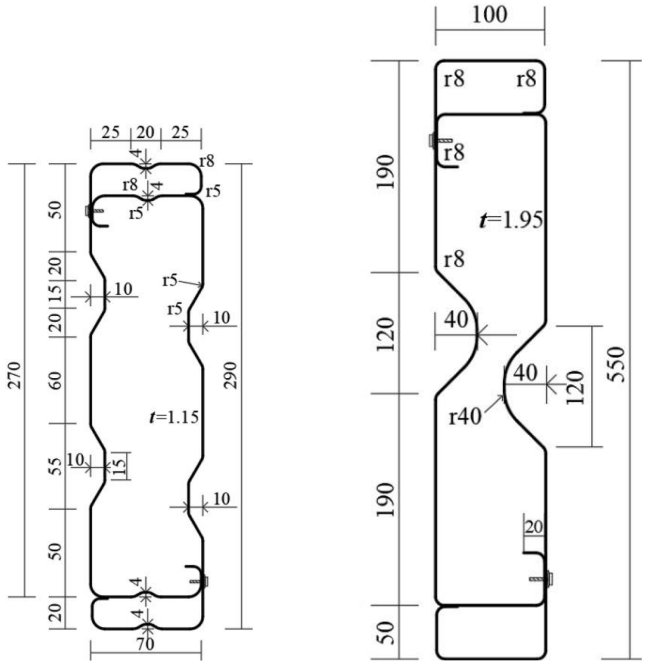

2.7 Summary

The literature review reveals that researchers have employed three main approaches to determine the moment capacity of cold-formed steel (CFS) sections: experimental testing, finite element analysis (FEA), or a combination of both. Additionally, optimisation efforts have primarily focused on cross-sectional and material optimization.

However, for built-up sections with various cross-sectional geometries, there is a notable lack of specific design guidelines for determining moment capacity. Researchers have often

compared their results with existing guidelines and developed their equations for calculating capacities. Despite these efforts, none have proposed a simplified methodology capable of efficiently determining moment capacity while reducing computational time. To address this gap, a numerically inexpensive model could be developed to calculate moment capacity across different cross-sectional dimensions.

Chapter 3 – Numerical analysis of the cold-formed steel box section beam

3.1 Introduction

To investigate the ultimate moment capacity of CFS built-up beams, numerical analysis was performed using ABAQUS [44]. The FE model was developed based on the centre line dimensions of the cross sections of the built-up beams. The FE models developed in this study were initially validated against experimental tests conducted by Dai et al. [7] on CFS built-up beams under four-point bending as shown in Figure 3-1. In the FEA modelling, connections between beams and between beams and lateral restraints were established using a "Cartesian" beam connector. Initially, the model was developed without considering any imperfections, resulting in a 10.67% difference between the FEA and test results for the maximum bending moment. Geometric imperfections were then incorporated as described by Schafer et al. [47], reducing the percentage difference to 2.71%. As shown in the Figure 3-7, the experimental and FEA results are 39.5 kN · m [7] and 40.6 kN · m, respectively.

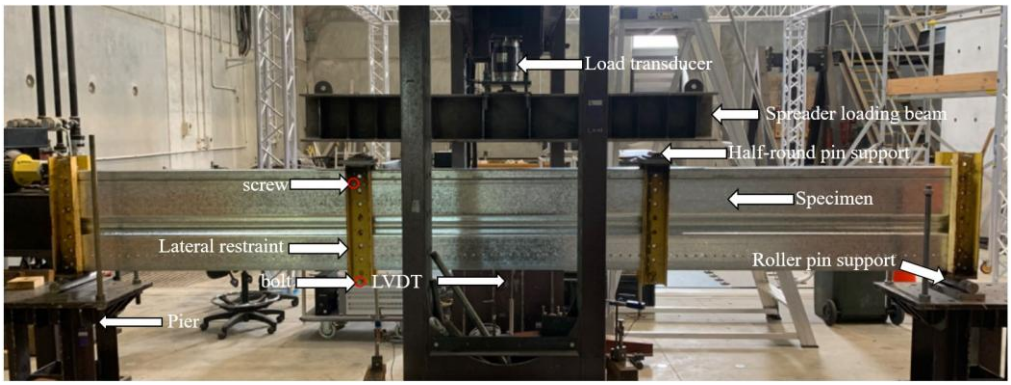

Figure 3-1: Experimental setup of four-point bending setup [7].

3.2 Modelling of geometry

To accurately replicate the four-point bending test setup used by Dai et al. [7], four distinct parts were created in ABAQUS [44]. The geometric details are provided in Table 2-4. These parts were named as follows (refer to Figure 3-2): BeamL (representing the left side of the built-up beam), BeamR (representing the right side of the built-up beam), End (the support block at the far ends of the beam), and LB (the loading block used to apply displacement to the

beam). The final geometry (assembling BeamL and BeamR together) and the complete test setup (assembling BeamL, BeamR, End, and LB together) were created by connecting the parts using appropriate connectors as described in Section 3.6. The assembly is shown in Figure 3-3.

(a) Isometric and side view of view BeamL

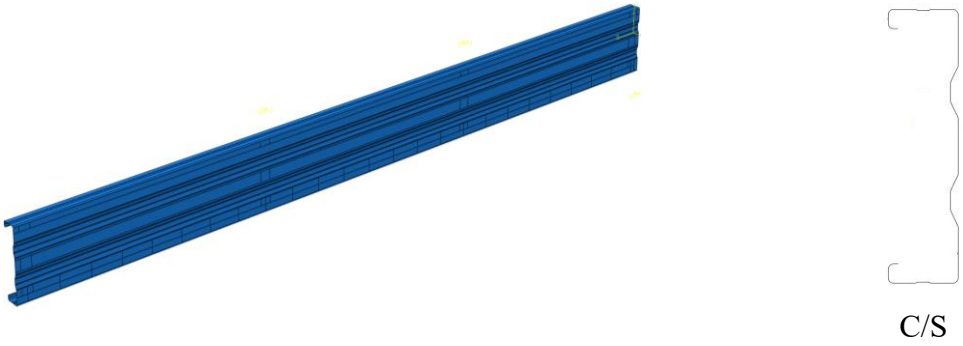

(b) Isometric and side view of view BeamR

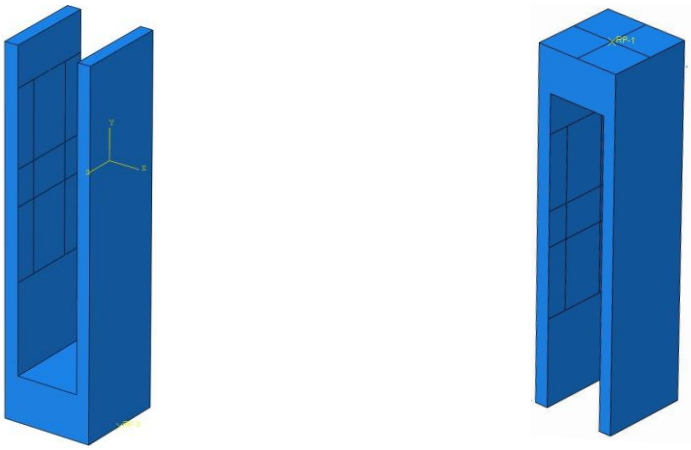

(c) End (d) LB

Figure 3-2: Numerical setup for FEA.

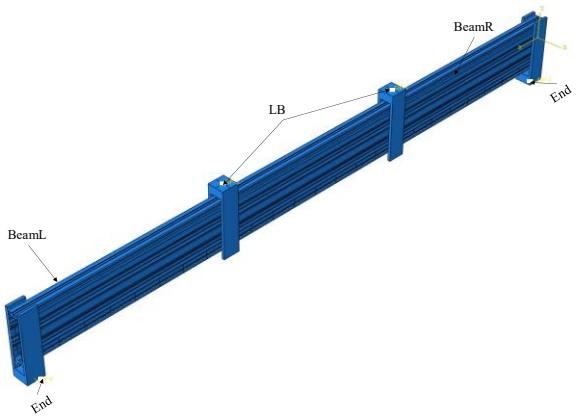

Figure 3-3*:* Assembly of the parts to resemble the four-point bending setup.

3.3 Material modelling

The nonlinear properties of the CFS material were included in the FE models based on the measured stress-strain curves obtained from the flat tensile coupon tests conducted by Dai et al. [7] as shown in Figure 3-4. To this end, equations (1) and (2) were used to convert an engineering stress-strain relationship to a true one in ABAQUS [44].

$$\sigma_t = \sigma_e(1 + \varepsilon_e) \tag{1}$$

$$\varepsilon_t = ln(1 + \varepsilon_e) - \frac{\sigma_t}{E} \tag{2}$$

where E is Young's modulus; σ_t refers to true stress; ε_t is true strain; σ_e indicates engineering stress; and indicates engineering strain.

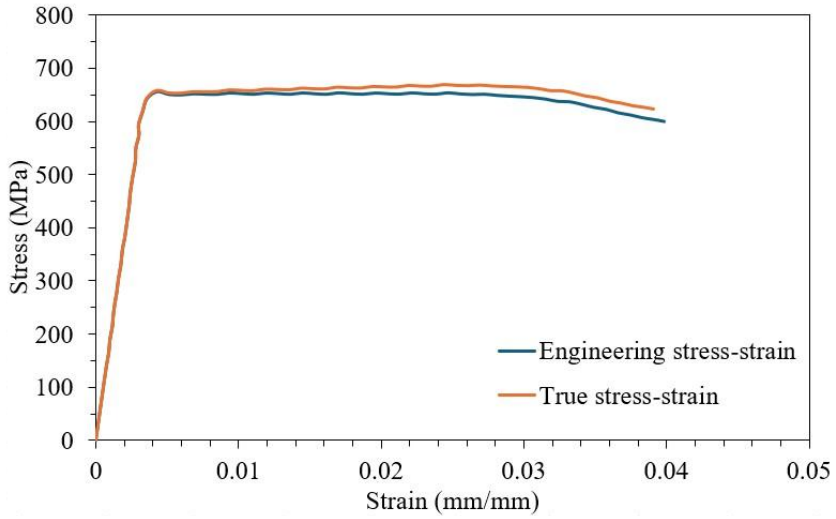

Figure 3-4: True and engineering stress-strain curve.

3.4 Analysis methods

Two methods of analysis were employed in the present study: (1) elastic buckling analysis and (2) non-linear analysis using static general incorporating artificial damping factor. For the buckling analysis, a similar model was used with modified boundary conditions by applying a concentrated unit load along the z-axis. The eigenvalues from the first mode were then incorporated into the model to conduct the non-linear analysis.

Significant convergence challenges arose during the FE analysis of CFS built-up beams in ABAQUS [44], leading to premature termination and prolonged program running times. These challenges stemmed from considering material, geometric, and contact nonlinearities in the model. Despite the problem being well-defined and the surfaces initially in contact, ABAQUS [44] failed to reach a convergent solution in the initial analysis step. Various conventional attempts were made to address the issue, such as reducing the initial step size, refining the mesh, and adjusting contact parameters, but were unsuccessful.

Ultimately, the problem was resolved by introducing artificial damping to the model, which did not compromise solution accuracy. An adaptive automatic stabilization scheme, consistent with the method proposed by Wang and Young [25], was employed throughout the study. Two general static steps were conducted, following this nonlinear solution approach. The "Static General" analysis step was utilized for the numerical simulation of the four-point bending test. In the first step, a small displacement load was applied to the built-up beam models to establish contact between master and slave surfaces gradually. This aimed to stabilize unstable quasi-static problems and convergence issues, aided by artificial damping with a default damping factor value of 0.00015. In the subsequent step, the full specified displacement load was applied until the collapse of the built-up beams. This approach, incorporating large displacements and a damping factor, utilized initial, minimum, and maximum increments of

0.001, 1e-9, and 0.1, respectively. The modelling approach effectively utilized the automatic stabilization algorithm in the two steps to address convergence problems in the current study.

3.5 Surface contact and constraints

To simulate the interaction between two overlapping sigma channel sections in a built-up box, “Surface-to-surface” interaction was employed. The contact properties were defined with frictionless tangential behaviour, and “Hard Contact” was set in the normal direction with a coefficient of friction of 0.2 to prevent any penetration between individual parts. Additionally, a simplified approach was used to join the two channel sections by employing “Cartesian” beam connectors (refer to Figure 3-5 and Figure 3-6(b)) between two nodes to represent the screw connections. This approach was chosen over modelling the screws with three-dimensional solid elements for two main reasons: (1) no failure in the screw connections was observed in the experimental results reported by Dai et al. [7], and (2) the complex of meshing screws in 3D can lead to significant convergence challenges in FEA.

For developing the interaction between the built-up beam and the lateral restraints, a similar “Surface-to-surface” interaction was implemented. Additionally, to represent the screws used in the experimental setup, a “Cartesian” beam connector was utilized as shown in Figure 3-5.

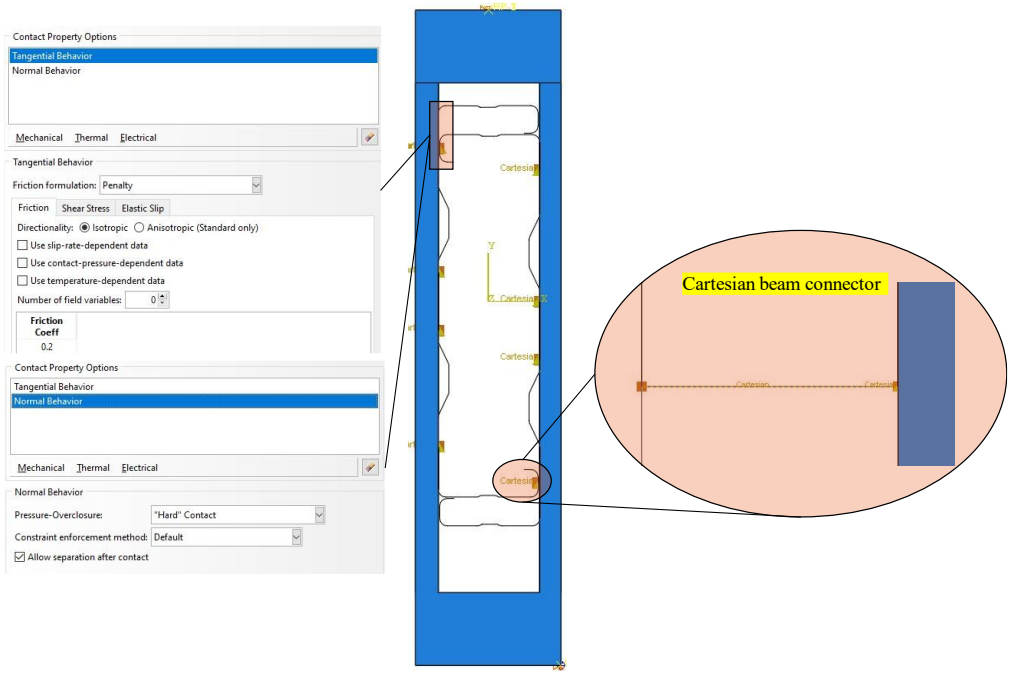

Figure 3-5: Contact properties and cartesian beam connector arrangement.

3.6 Loading and boundary conditions

As depicted in Figure 3-6(b), reference points were assigned at the midpoints on the top surface of the supports located beneath the loader beam. To simulate the experimental boundary conditions, displacements along the x and z axes and rotations around the y and z axes were restrained. For the two lateral restraints positioned towards the ends, displacements along the x and y axes, and rotations around the y and z axes were restrained to simulate a pin-ended boundary condition.

3.7 FE Mesh

The four-noded quadrilateral S4R shell elements were utilized to simulate CFS components. Three-dimensional solid elements (C3D8R) were used to simulate the lateral restraints. A 15×15 mm mesh size (length by width) was applied for CFS built-up box sections. A 20×20 mm mesh size was used when modelling the lateral restraints. Similar mesh sizes have been adopted in previous studies[7]. A finer mesh was applied to corner regions (see Figure 3-6 (a)) to enable accurate predictions for the flexural capacity of the CFS built-up stiffened box sections.

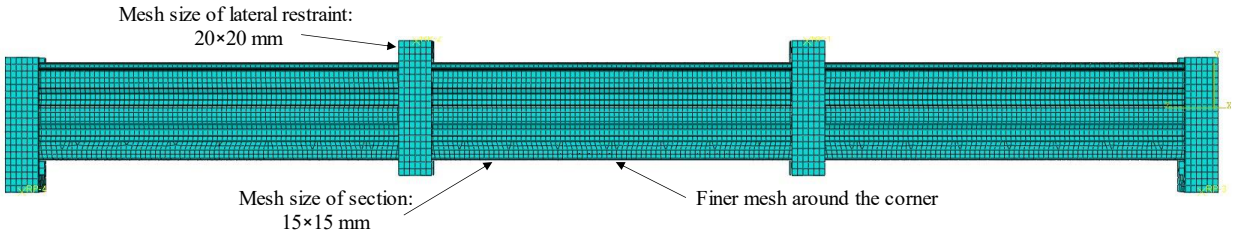

(a) FE Meshing details

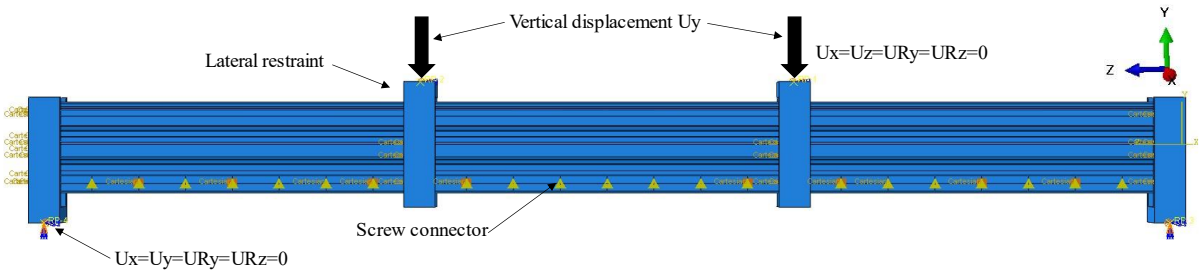

(b) Loading and boundary condition

Figure 3-6: Four-point bending setup.

3.8 Geometrical Imperfections

CFS sections, due to their thin walls, are prone to geometric imperfections. Measuring these imperfections is essential, as they affect both the local and global behaviour of CFS members [48]. Consequently, a sensitivity study was conducted, revealing that the local geometric imperfections of the built-up box section in this study were significant. First, elastic buckling modes were obtained from an eigenvalue buckling analysis in ABAQUS [44], where a unit load was applied to the beam model at the same loading points used in the tests. The lowest local buckling mode was identified and then scaled by the actual measured magnitude of the initial local geometric imperfection [24][48]. The moment capacity of the beam model, accounting for local geometric imperfections was found to be lower than that without considering these imperfections, as shown in Figure 3-8. The magnitudes of initial geometric imperfections were determined according to AS/NZS 4600:2018 [10]. The imperfection magnitude for local buckling was determined using equation (3), and the imperfection magnitude for distortional buckling was determined using equation (4).

$$S_{ol} = 0.3t\sqrt{\frac{f_y}{f_{ol}}} \quad (3)$$

$$S_{od} = 0.3t\sqrt{\frac{f_y}{f_{od}}} \quad (4)$$

Where t means thickness; f_y means yield stress; f_{ol} means local buckling stress; f_{od} means distortional buckling stress of the CFS built-up section. The geometric imperfection magnitudes used in FE models of CFS built-up stiffened box sections were scaled to the measured values. To incorporate the geometrical imperfections in FE models following keywords need to be added to the input file of ABAQUS [44], *IMPERFECTION, FILE=BUCKLE (i.e. Name of the Abaqus Output Database file), STEP=1.

3.9 Residual stresses

Residual stresses in CFS sections differ significantly from those in hot-rolled sections. In CFS sections, membrane residual stress is negligible compared to flexural residual stress, which is the reverse of the situation in HRS. In a cold-formed section, flexural residual stress is distributed linearly across the thickness, with compression on the inside surface and tension on the outside [48]. These residual stresses can be incorporated into an FE model as an initial state using the ABAQUS (*INITIAL CONDITIONS, TYPE=STRESS) option. However, previous studies have demonstrated that residual stresses have a negligible effect on the ultimate moment capacity of CFS beams [48][49][50]. Therefore, the present study did not consider residual stress to avoid complexity in modelling.

3.10 FE Validation

The validation has been carried out based on the test conducted by Dai et al. [7]. Figure 3-7 illustrates the moment-displacement relationship of the specimens determined from the FEA, showcasing results both with and without imperfections, alongside the experimental test data. The FEA predictions for the CFS built-up stiffened box sections demonstrate reasonable

agreement with the experimental test data. Figure 3-8 displays the deformed shapes of the stiffened box sections as determined by the FEA. Both the initial stiffness and maximum flexural capacity predicted by the FEA closely match the experimental results.

The initial stiffness was calculated using the reference point on the top surface of the restraints. For calculating the maximum force, the reference node on the farther end was considered. To determine the maximum flexural capacity, the maximum force obtained from the FEA results was multiplied by the pure-bending length. The maximum force was found to be 33.83 kN, and with a pure-bending length of 1.2 m, the resulting moment was 40.6 kN · m. The experimental result for the validated model was 39.5 kN · m, resulting in a percentage difference of 2.75%.

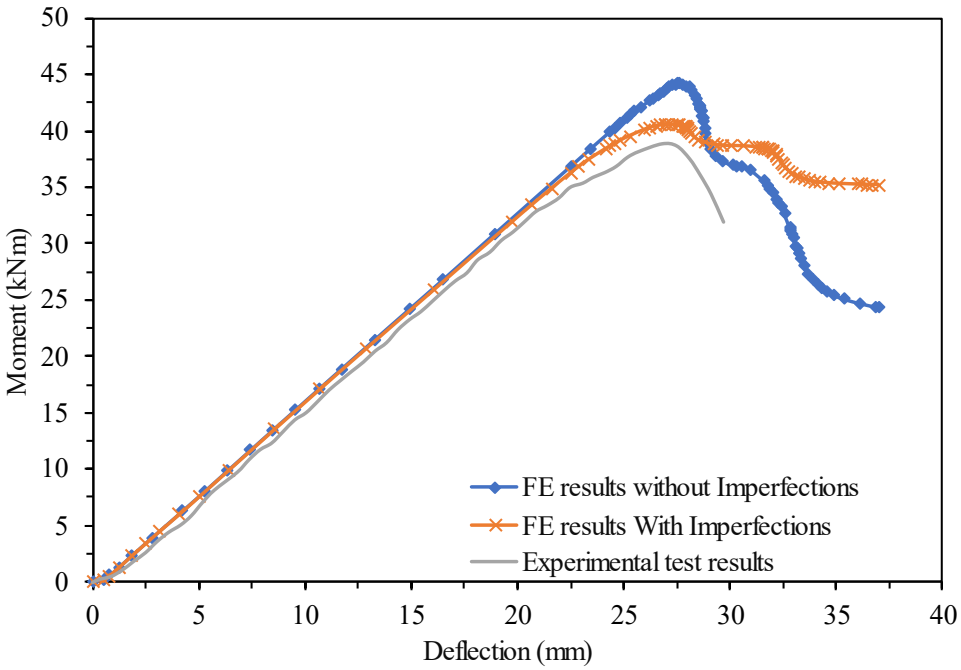

Figure 3-7: Comparison between Experimental results and FEA results.

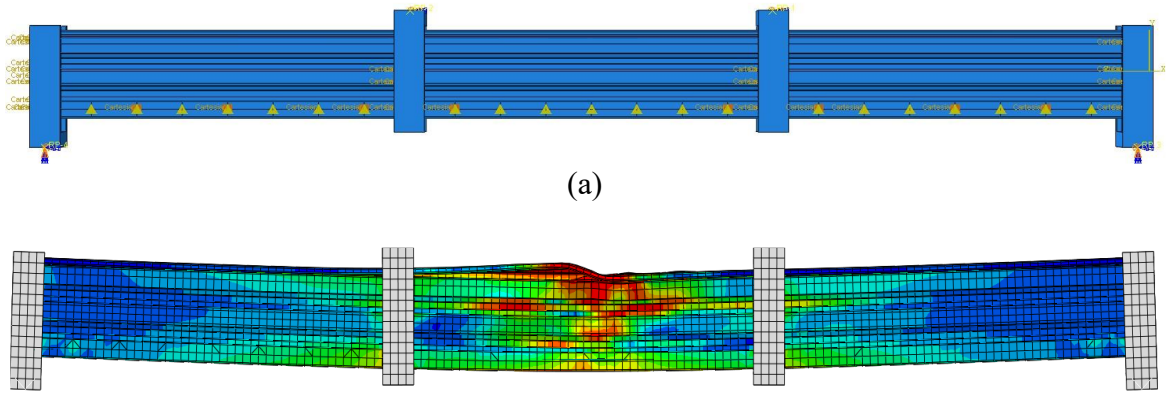

(a)

(b)

Figure 3-8: Deformed shape.

3.11 Concluding remark

This chapter discusses the development of the FE model for built-up box sections subjected to four-point bending. The FE model incorporates material non-linearity and imperfections. The developed model has been validated against the test setup in terms of the moment-displacement curve and deformed shape. Additionally, the four-point bending model will be used in the next chapter to develop a simplified model.

Chapter 4 – Development of a simplified numerical model

4.1 Introduction

This chapter shows the development of a computationally inexpensive simplified numerical model developed in ABAQUS [44] to reduce the complexity of the four-point bending model. The accuracy of the proposed model was evaluated by comparing the FEA results with the analysis results presented in Chapter 3. The simplified model was derived from the pure-bending model, which itself was developed from the four-point bending model (Figure 4-1 (a-c)). The subsequent sections detail the modelling techniques used to develop the simplified FE model.

4.2 Pure-bending model

To develop the simplified numerical model shown in Figure 4-1 (c), two key steps were undertaken. Initially, a pure-bending model was developed as illustrated in Figure 4-2 (b), which was then further simplified to produce the final simplified model as shown in Figure 4-2 (c) .

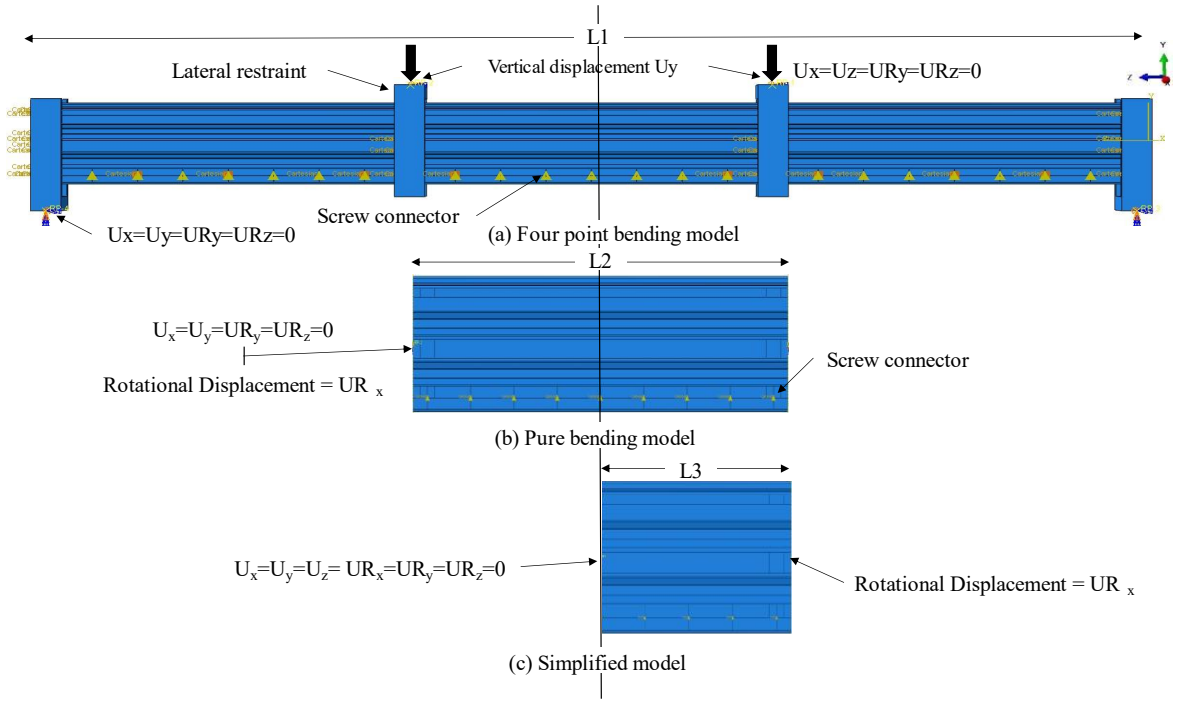

Figure 4-1: Steps for development of simplified model from four-point bending model.

The pure-bending model was validated against the experimental and FEA results presented in Chapter 3. The FE model for pure bending was developed in Abaqus [10]. The three lengths depicted in Figure 4-1 are as follows: L_1 = (3600 + 200) mm, L_2 = (1200 + 100) mm, and L_3 = (600 + 50) mm. In these measurements, 3600, 1200, and 600 represent the bending lengths, while 200, 100, and 50 denote the widths of the support blocks, respectively.

4.2.1 Introduction to pure-bending model

To reduce the complexity of the four-point bending model and decrease computational time, a pure-bending model was developed that represented only one-fourth of the original four-point bending setup, as shown in Figure 4-2. This model had an overall length of 1300 mm, comprising 1200 mm for the main section and an additional 100 mm at each end to accommodate the supports. The number of screws used to connect the single channel sections was reduced by 62.5% compared to the four-point bending model. Specifically, while the four-point bending model required 24 screws spaced at 150 mm for connections, the pure bending model needed only 9 screws.

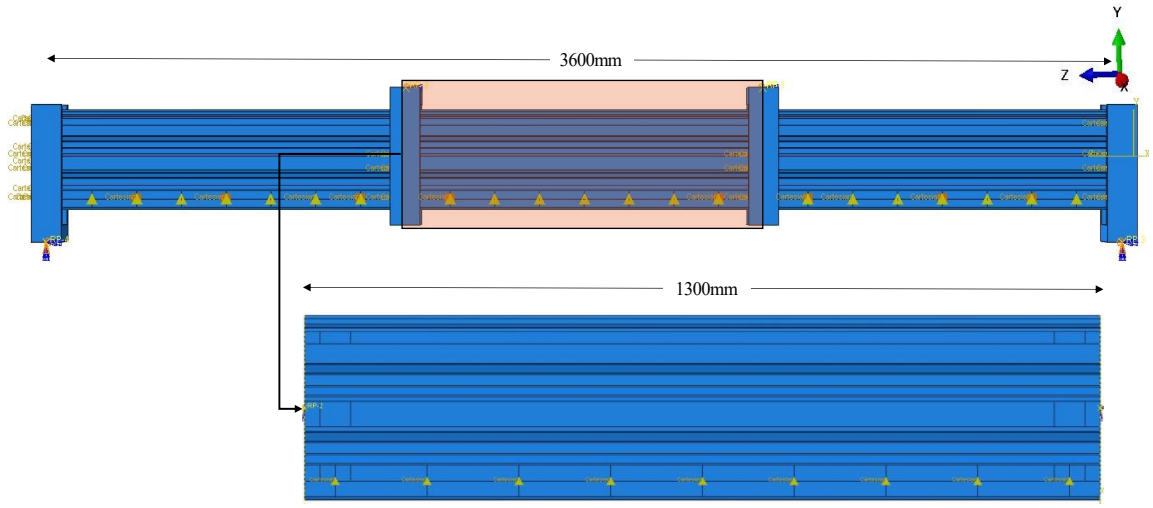

Figure 4-2: Pure-bending model.

4.2.2 Numerical study on pure-bending model

The numerical model used for the pure-bending study was identical to the model described in section 3.2, except that the support and loading blocks were removed for

simplification. The material properties were sourced from the test data provided by Dai et al. [7]. Additionally, the stiffened single-channel sections, as shown in Figure 3-2, were positioned FTF. The analysis method and interaction properties outlined in Sections 3.5 and 3.6 were similarly applied.

The four-node shell element S4R, which features six degrees of freedom (three translational and three rotational) per node with reduced integration, was used to discretize the CFS built-up beams. As shown in Figure 4-3, a fine mesh with dimensions of 5×5 mm (length by width) was applied to the CFS built-up beam sections.

To simulate the interaction between two overlapping sigma channel sections in a built-up box, the interaction properties described in Section 3.6 were utilized.

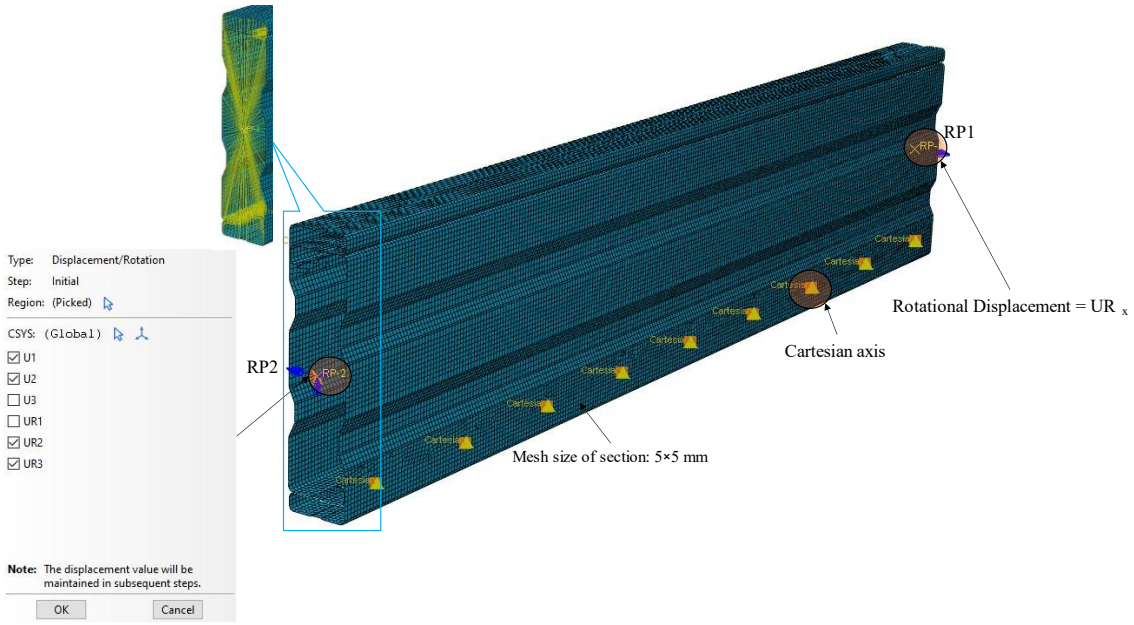

Figure 4-3: Loading and boundary conditions for the pure-bending model.

4.2.3 Loading and boundary conditions

As shown in Figure 4-3, reference points (RP1 and RP2) were assigned at the midpoints on both ends of the section. These points were coupled to the edges of the section as shown in Figure 4-3, ensuring that one entire side of the section was connected to each reference point.

Various combinations were tested to match the boundary conditions of the four-point bending test. The boundary conditions that produced results most consistent with both FEA and experimental data were adopted. To replicate the experimental boundary conditions, displacements along the x and y axes, and rotations around the y and z axes, were restrained. To simulate the pure-bending condition, a rotational displacement was applied in the UR_X direction for both reference points.

4.2.4 FE Validation

The pure-bending model developed possessed similar geometric properties to the four-point bending model as shown in Table 2-4. As illustrated in Figure 4-6, the moment capacity of the pure-bending model was 39.85 kN · m with imperfection, compared to 40.6 kN · m from the four-point bending model and 39.5 kN · m from the experimental results presented by Dai et al. [7]. The percentage difference between the moment capacity of the pure-bending model compared to the four-point bending FE model and test data is 1.86% and 0.88%, respectively. Based on the comparison of moment capacity, it can be concluded that the pure-bending model can accurately predict the test results presented in Dai et al.'s study [7].

4.3 Simplified model

After validating the pure-bending model, a further simplified version was developed to reduce both complexity and simulation time. This simplified model, as illustrated in Figure 4-1 (c), uses only half of the pure-bending model. As shown in Figure 4-4, this model has a length of 650 mm, which includes 600 mm of the main section and an additional 50 mm at one end for support. The number of screws was reduced to less than half of those required for the pure-bending model. Specifically, the pure-bending model used 9 screws spaced at 150 mm, while the simplified model required only 5 screws, representing a 44.44% reduction. Overall, the reduction in the number of screws from the four-point bending model to the simplified model

amounts to 79.17%. The results of numerical modelling and finite element (FE) validation for the simplified model are discussed in the preceding sections.

4.3.1 Numerical study on the simplified model

The modelling techniques for the pure-bending model, as described in Section 4.2.2, were similarly applied. As shown in Figure 4-5, reference points (RP1 and RP2) were assigned at the midpoints on both ends of the section. These points were coupled to the edges of the section, as illustrated in Figure 4-3, ensuring that one entire side of the section was connected to each reference point. The boundary conditions that produced results most consistent with both the FEA results for both the four-point bending and pure-bending models, as well as the experimental data, were adopted.

The boundary condition in the simplified model has been considered with one side as fixed and on another side, bending has been applied. To incorporate the cantilever boundary condition, RP1 was restrained in all three directions for both displacements and rotations. A rotational displacement was applied in the UR_X direction at RP2.

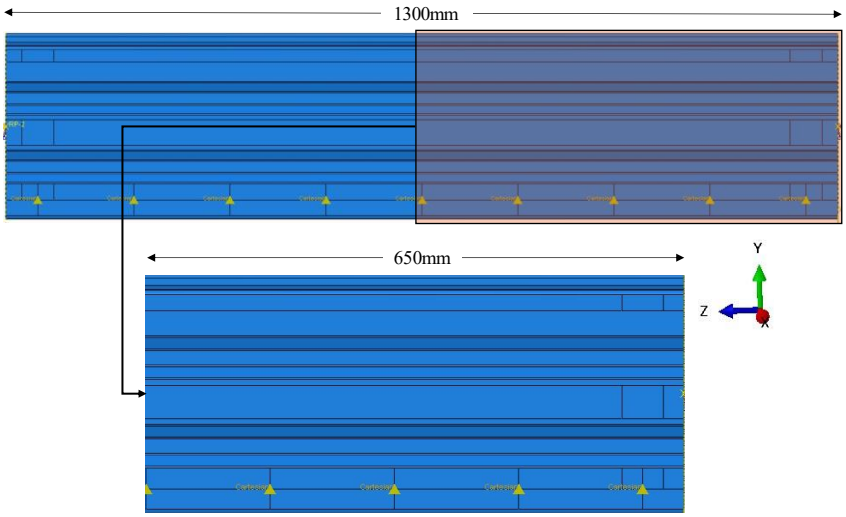

Figure 4-4: Simplified model.

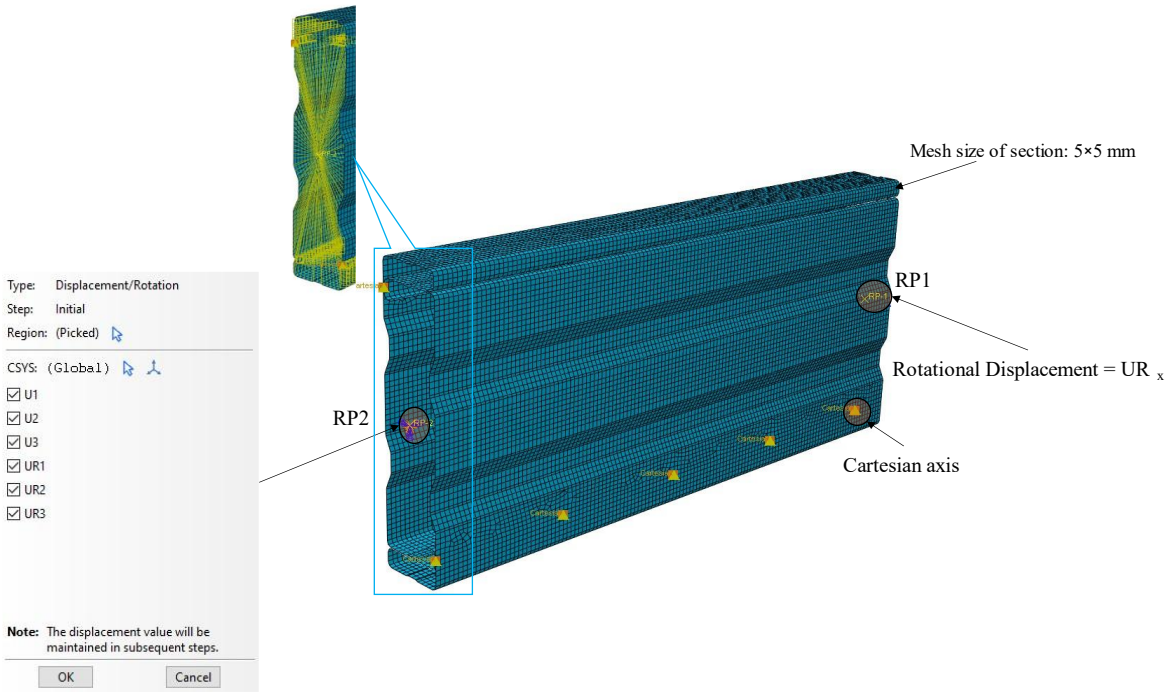

Figure 4-5: Loading and boundary conditions for the simplified model.

4.3.2 FE validation for the simplified model

The simplified model developed possessed similar geometric properties to the four-point bending model as shown in Table 2-4. As illustrated in Figure 4-6, the moment capacity of the simplified model was 39.00 kN · m with imperfection, compared to 40.6 kN · m from the four-point bending model and 39.5 kN · m from the experimental results presented by Dai et al. [7]. The percentage difference between the moment capacity of the simplified model compared to the pure-bending FE model and test data is 2.16% and 1.27 %, respectively. The slight difference in percentage, although negligible, is attributed to the simplified boundary and loading conditions applied in the simplified model. Based on the comparison of moment capacity and deformed shape presented in Figure 4-6 and Figure 4-7 respectively, it can be concluded that the simplified model can accurately predict the test results presented in Dai et al.'s study [7].

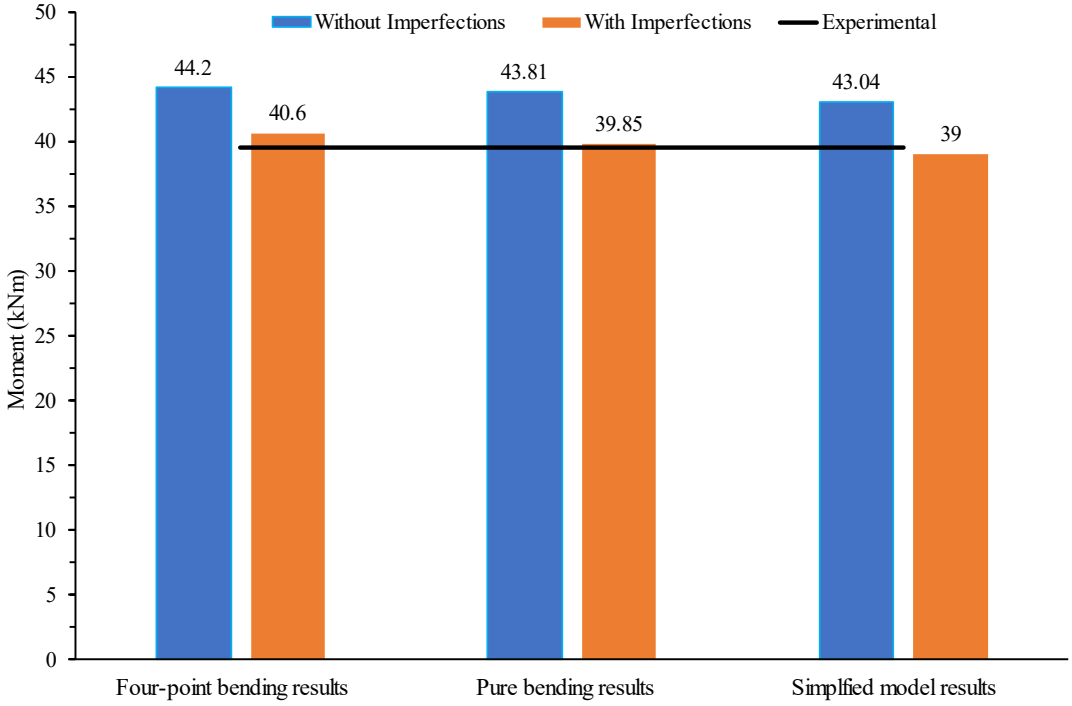

Figure 4-6: Comparison of moment capacities for all cases.

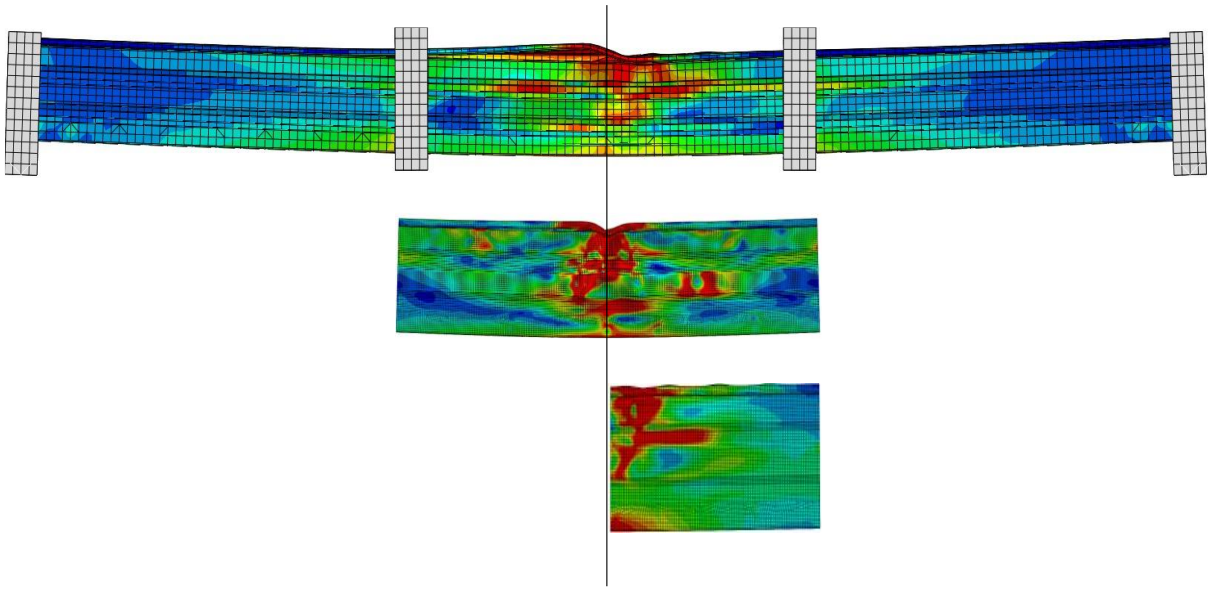

Figure 4-7: Comparison of deformed shapes for all the cases.

4.4 Comparison of computational time

Table 4-1: Comparison of computational time

Model name	Number of elements [44]	Mesh size (mm)	Moment capacity (kN · m)	CPU time (sec) [44]
Experimental results	-	-	39.50	-
Four-point bending	1059844	5×5	40.60	265367.3
Pure bending	64515	5×5	39.85	14339.0
Simplified	30703	5×5	39.00	5811.4

To demonstrate the comparison, a computational study was conducted where all models were assigned a fine mesh with dimensions of 5×5 mm (length by width). The data presented in Table 4-1 was extracted from the “Storm and Sanitary Analysis Data file” (.dat file). To obtain this data, an additional line was added to the ABAQUS .inp file (** JOB TIME SUMMARY _ USER TIME (SEC) _ SYSTEM TIME (SEC) _ TOTAL CPU TIME (SEC) _ WALLCLOCK TIME (SEC)). Among the various times available from the .inp file, "TOTAL CPU TIME (SEC)" was selected to facilitate comparison with previous studies. Table 4-1 indicates that the number of elements required for the simplified model is 97.10% less compared to the four-point bending model, resulting in a 97.81% reduction in CPU time for the simplified model without compromising on the moment capacity.

4.5 Effect of screws in the web of the built-up beam

The study was further extended to replicate practical conditions, such as beam-column connections. In real-world scenarios, connections exist in beams that are often subjected to various loads. This study specifically considered bending. The practical condition was achieved by constraining the built-up section with screws on the web of the stiffened single-channel

members, as shown in Figure 4-8. In the earlier simplified model, one side was fixed while a moment was applied to the other. In this case, the fixed side has been replaced with screws, while a moment is applied to the other side. The fixity conditions for both the simplified model and the current screw-web model are shown in Figure 4-9. The details of the FEM and the boundary conditions used to simulate the screws in the web are described in the following sections.

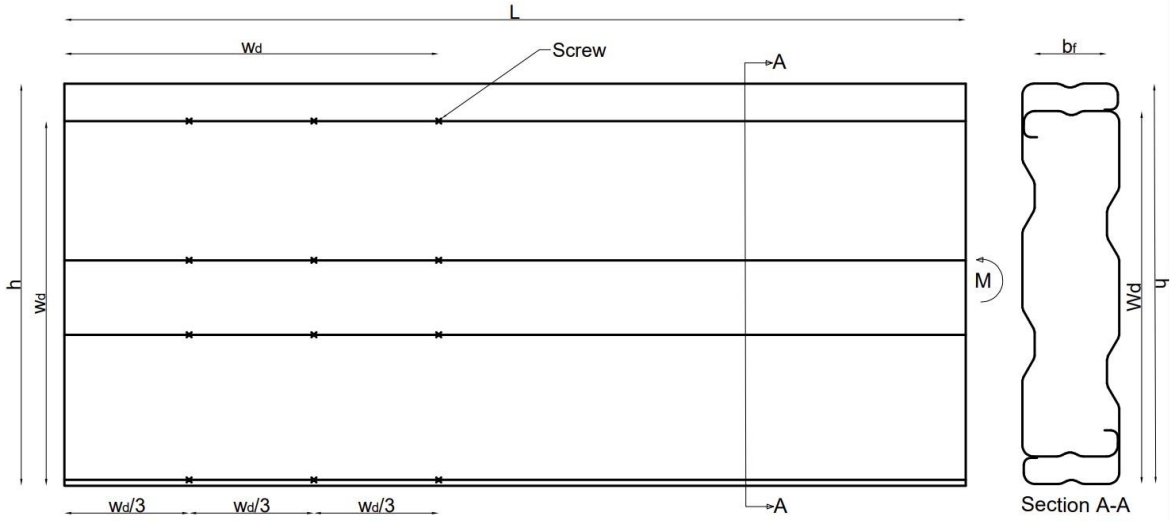

*h = depth of the built-up section, w_d = web depth, L = length of beam, b_f = flange width, M = Moment
**dimensions of the members are mentioned in Table 2-4

Figure 4-8: Schematic of the screw placement in the web region of the built-up section.

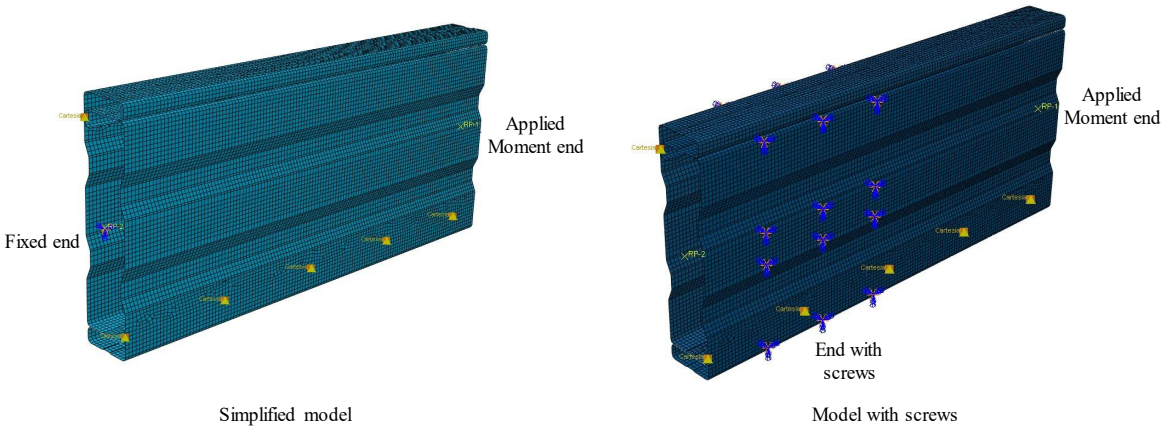

Figure 4-9: Left: Simplified model, right: Screw-web model.

4.5.1 Numerical study

The modelling techniques described in this section are similar to those mentioned for the simplified model in section 4.3.1. As illustrated in Figure 4-10, a reference point (RP1) was assigned at the midpoint of one end of the section, while the other end was equipped with screws in the web. The positioning and spacing of the screws are shown in Figure 4-8.

As shown in Figure 4-10, the screws are restrained in all three directions for both displacements and rotations. A rotational displacement was also applied in the UR_X direction at RP1.

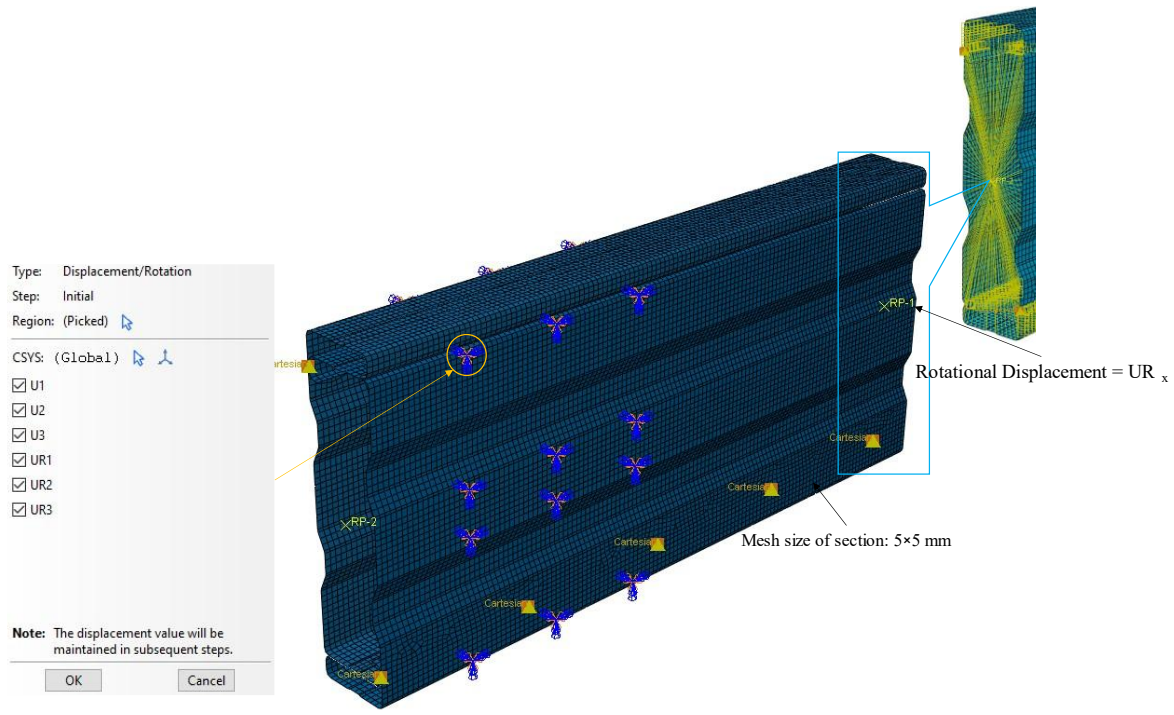

Figure 4-10: Loading and boundary conditions for the screw-web model.

4.5.2 Comparison of results with the simplified model

The model developed with screws in the web had similar geometric properties to the four-point bending model described in Table 2-4. The only difference was the added screws in the web region to simulate the practical condition, as shown in Figure 4-9. The moment capacity of the simplified model and screw-web model is shown in Figure 4-11. Geometric

imperfections were not incorporated into this model because the screws themselves created imperfections.

Additionally, when comparing the FEA results of this model to the simplified model, a 19.26% decrease in the moment capacity is observed. This can be attributed to the fact that the load transfer mechanism in CFS screw moment connections is mainly through the screw group in the web of built-up beam elements., which may lead to relatively large bimoment and warping deformations. A similar reduction in the moment capacity (20% in Lim and Nethercot [5], 25% in Phan et al. [40]) in the CFS connections has been observed in previous experimental and numerical studies.

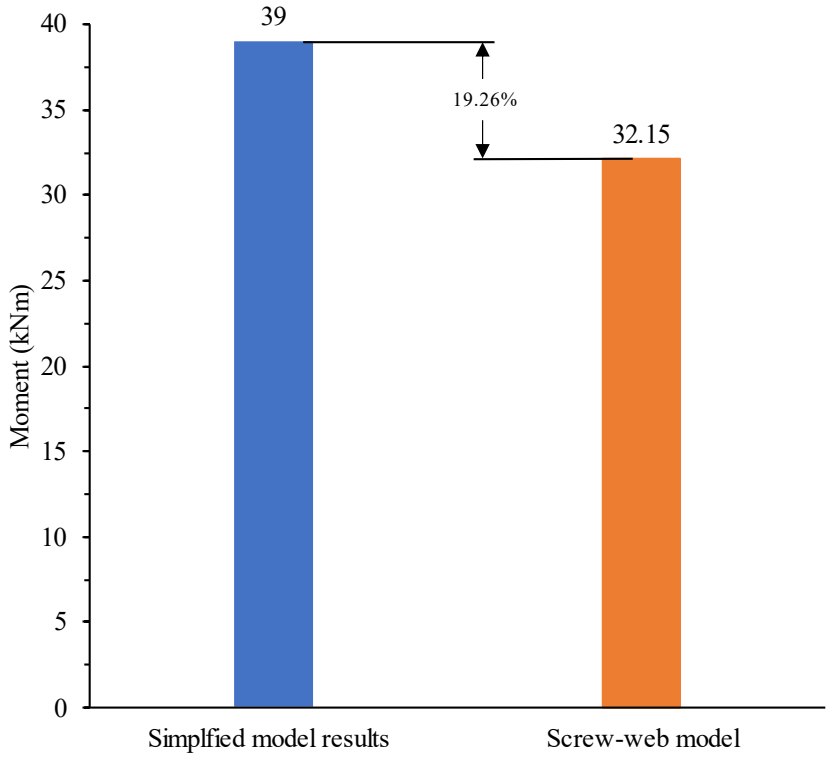

Figure 4-11: Comparison of moment capacities.

4.6 Concluding remark

This chapter presents the development of a simplified model, derived from a four-point bending model, designed to determine the moment capacity of various built-up sections without the need for comparison with experimental results. As illustrated in Figure 4-6, the simplified

model efficiently calculates moment capacity with significantly less computational time without compromising the accuracy of the results compared to the full four-point bending model. The simplified model exhibited reasonable agreement with both FEA and experimental results, showing percentage differences in moment capacity of 2.16% and 1.27%, respectively.

The developed simplified model does not require any specific calibration to match the moment capacity observed in testing. The only necessary adjustments are to the boundary conditions, as described in this chapter. As a result, this model can be used to predict the moment capacity of various built-up beams without the need for experimental testing. This will allow engineers and researchers to efficiently determine the moment capacity of these complex built-up beams, as well as predict their failure modes, without the lengthy process of experimental setups or the complexity of finite FE modelling for the entire four-point bending test. This approach facilitates faster and more reliable studies on built-up CFS sections.

Furthermore, a model incorporating screws (screw-web model), as depicted in Figure 4-10, was developed to simulate the practical conditions of a beam-beam or beam-column connection. The results indicated that the moment capacity of the screw-web model was lower than that of the simplified model due to the large number of warping deformations and bimoment. Consequently, both the simplified and screw-web models will be employed in a comprehensive parametric study to determine the moment capacity of the built-up sections in the subsequent chapter.

Chapter 5 – Application of the proposed modelling technique

5.1 Introduction

In this chapter, the application of the simplified model has been extended to built-up beams with different cross-sections. This robust and efficient numerical model successfully simulates the behaviour of the four-point bending model in determining the moment capacity of built-up cross-sections for both face-to-face (FTF) and back-to-back (BTB) beams. The modelling approach used here is consistent with the technique described in Section 4.3. The FE models developed using the proposed method showed good agreement with the available test results for CFS BTB and FTF beams, highlighting the potential of the simplified model for accurately determining the moment capacity of built-up sections.

5.2 Summary of the experimental study conducted by Wang and Young [25]

Wang and Young [25] conducted an experimental study to evaluate the performance of built-up section beams with both BTB and FTF configurations, as illustrated in Figure 5-1. The beams were subjected to a four-point bending loading condition. These built-up sections were fabricated by connecting two channel sections using self-tapping screws, which were positioned either in the flanges or webs. The study included FTF and BTB sectional arrangements.

In Figure 5-1 and Table 5-1, h_w denotes the overall depth of the beam, b_f refers to the width of the flange, e indicates the position of the screw on the section, b_l represents the depth of the lip, r_i is the inner radius of the rounded corner sections, t refers to the thickness of the plate.

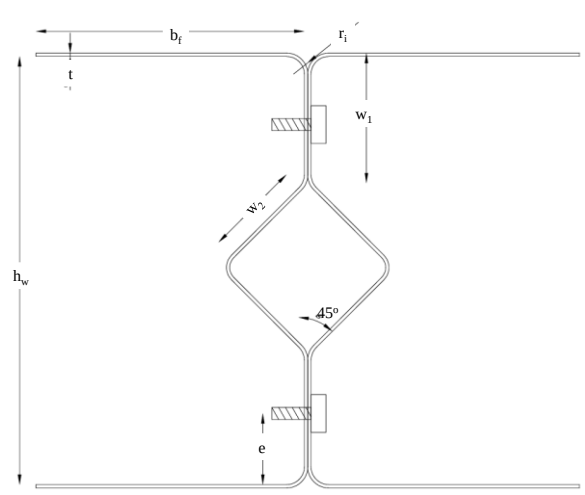

(a) BTB section (OV section)

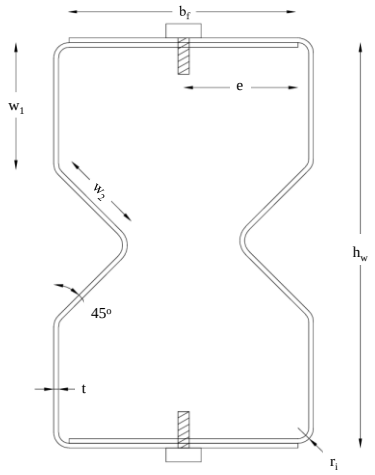

(b) FTF section with intermediate stiffeners (CV section)

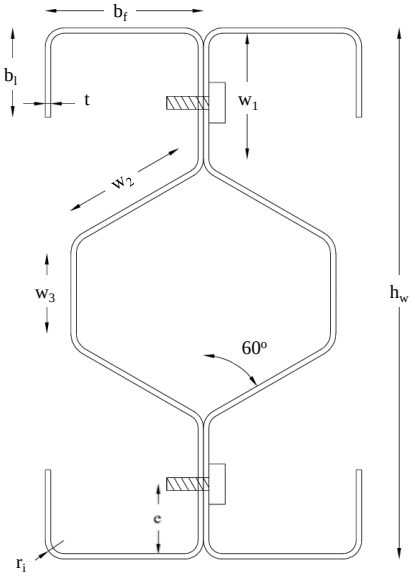

(c) BTB section with lip (OI section)

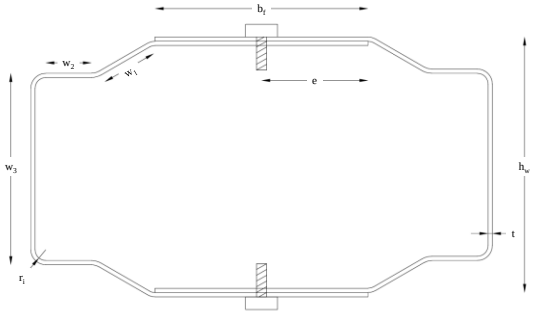

(d) FTF section without intermediate stiffeners (COF section – bending about X-axis, COW section – bending about Y-axis)

Figure 5-1: BTB and FTF sections.

Table 5-1: Dimensional details of the sections employed for numerical validation [25].

Specimen Id (as per literature)	b_l	b_f	h_w	w_1	w_2	w_3	t	$t*$	r_i
	mm	mm	mm	mm	mm	mm	mm	mm	mm
OV-0.48-B4	-	53.2	85.0	25.0	23.9	-	0.570	0.480	3.5
CV-1.0-B4	-	52.1	85.6	27.3	22.7	-	1.046	1.008	3.3
OI-1.0-B4	16.5	29.2	99.2	26.3	27.1	18.7	1.034	0.992	3.4
COW-1.0-B4	-	50.5	71.7	15.2	14.8	44.9	1.060	1.014	3.5
COF-1.0-B4	-	51.9	70.2	15.0	15.4	44.8	1.065	1.019	3.5

5.2.1 Test setup

Five different cross-sections [25], including both BTB (OV and OI sections) and FTF (CV, COF, and COW) configurations, were tested using a four-point bending setup, as depicted in Figure 5-2. The built-up sections were assembled using self-tapping screws. The material properties of all the built-up sections are provided in Table 5-2, while the cross-sectional dimensions for each section are detailed in Table 5-1.

Figure 5-2: Typical experimental setup for four-point bending test setup [25].

5.2.2 Material properties and cross-sectional dimensions

As shown in Table 5-2, Young's modulus is represented by (E), the 0.2% proof stress by ($\sigma_{0.2}$), the ultimate tensile strength by (σ_u), and the strain at fracture by (ε_f). The measured cross-sectional dimensions (Table 5-1) and material properties (Table 5-2) were utilized for validating the finite-element model and estimating the strength.

Table 5-2: Material properties of the sections [26].

Sections	E	$\sigma_{0.2}$	σ_u	ε_f
	GPa	**MPa**	**MPa**	**%**
OV-0.48	213	661	690	2.0
CV-1.0	213	598	599	9.7
OI-1.0	216	592	599	8.6
COF-1.0 / COW-1.0	216	572	583	9.6

5.3 Development of FE model

The FE models of all the sections, using the proposed simplified model, were developed and validated against the test results reported in [25]. The simplifications from the four-point bending model to simplified model are illustrated in the schematic diagram shown in Figure 5-3. A similar modelling approach, as described in Section 4.3, was employed, with two reference points assigned at either end of the built-up beams. These reference points were coupled with the nodes of the beams. As depicted in Figure 5-4, one end of the beam was fully restrained in all three directions for both displacements and rotations, while a rotational displacement was applied in the UR_x direction at the opposite end. The CFS built-up sections were modelled using four-noded quadrilateral S4R shell elements. Surface-to-surface contacts were defined between the two single-channel sections, and screw connections were simulated using a simplified method with "Cartesian" beam connectors between two nodes (see Figure 5-4). The material properties outlined in Table 5-2 were incorporated into the FE model.

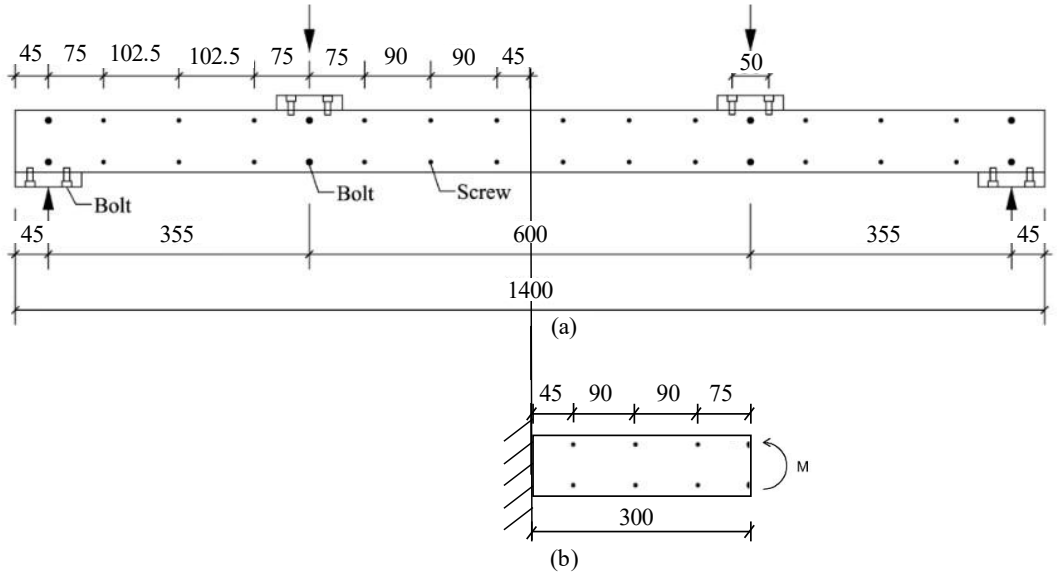

Figure 5-3: Schematics of (a) four-point bending model [25] and (b) simplified model.

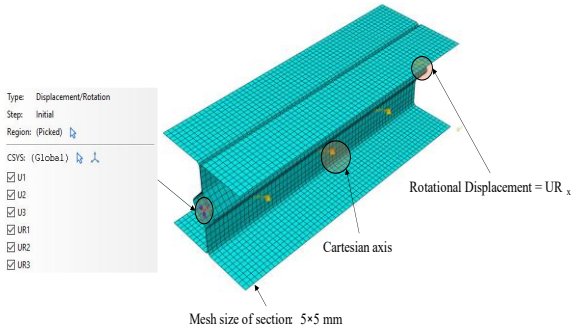

(a) OV section

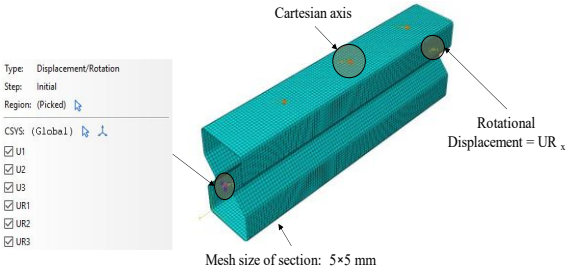

(b) CV section

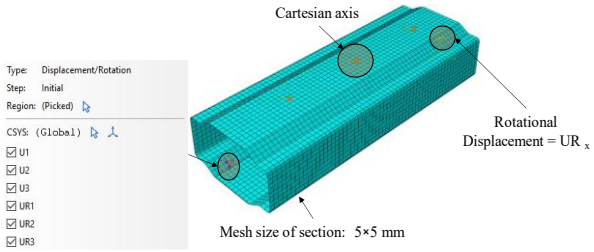

(c) COF section

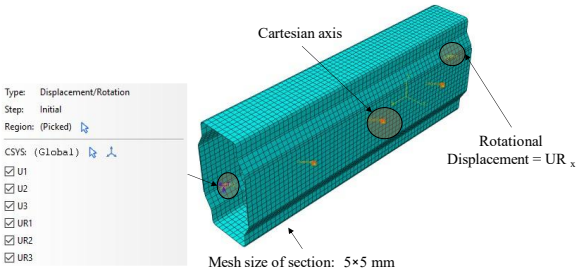

(d) COW section

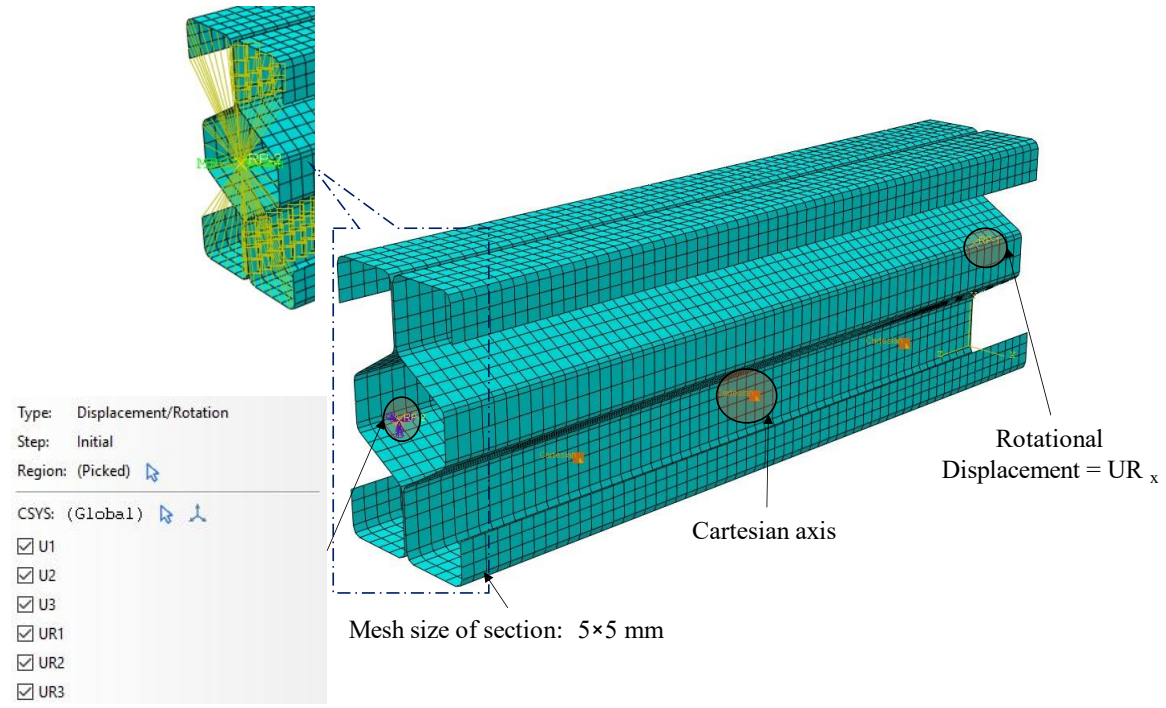

(e) OI section

Figure 5-4: Boundary conditions and FE meshing.

5.4 FE results and validation

The moment capacities obtained from both the experimental tests and FE models are presented in Table 5-3. As can be seen, the FE models show reasonable agreement with the experimental results in predicting the ultimate moment capacity. The average ratio of the

moment capacities from the experimental data to the FE models is 1.00, with a coefficient of variation (COV) of 11%.

Figure 5-5 compares the deformation shapes from the tests and FE models, showing that the FE models accurately replicate the observed deformations. The FE validation confirms that the proposed numerical method in the FE models can efficiently simulate cold-formed built-up beams with complex cross-sectional shapes. Additionally, the simplified model provides accurate predictions while reducing computational time, making it suitable for various cross-sectional configurations.

Table 5-3: Comparison of experimental and FEA results.

Specimen Id (as per literature)	**Moment capacities (kNmm)**		$\frac{M_{EXP}}{M_{FEA_S}}$
	M_{EXP} [25]	M_{FEA_S}	
OV-0.48-B4	1246	1336	0.93
CV-1.0-B4	4088	3937	1.04
OI-1.0-B4	6092	6067	1.00
COW-1.0-B4	4691	5459	0.86
COF-1.0-B4	3749	3156	1.19
Mean			1.00
COV			0.11

Note: M_{FEA_S} = Moment capacity predicted by the simplified FEA model

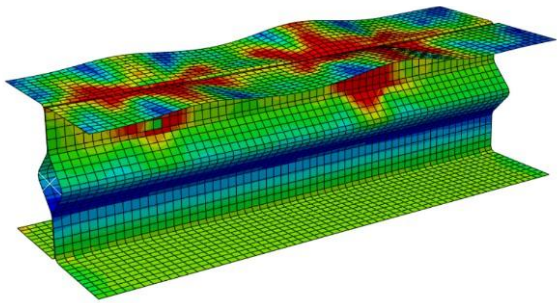

(a) Comparison of experimental [25] and numerical observations of specimen OV-0.48-B4.

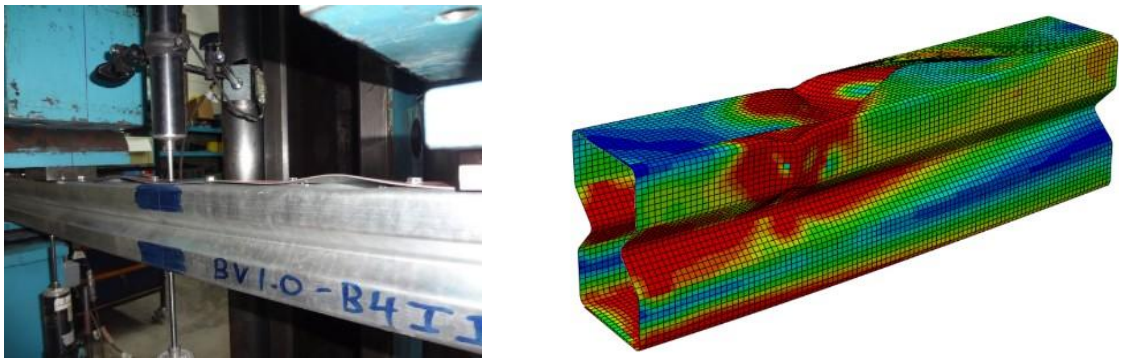

(b) Comparison of experimental [25] and numerical observations of specimen CV-1.0-B4.

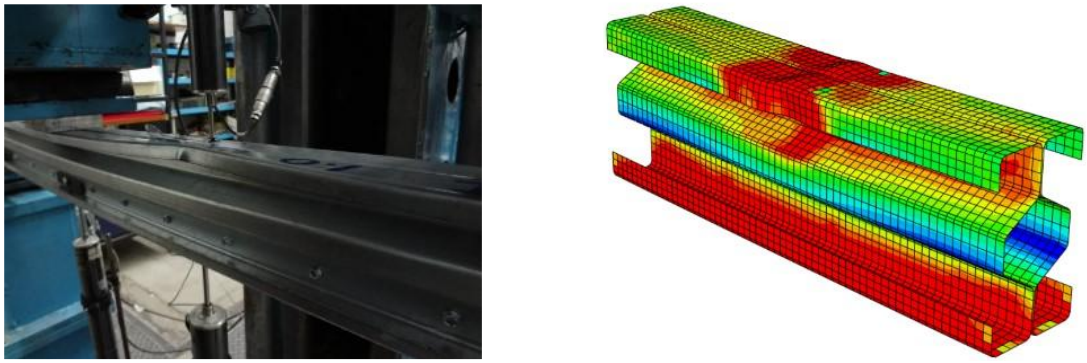

(c) Comparison of experimental [25] and numerical observations of specimen OI-1.0-B4.

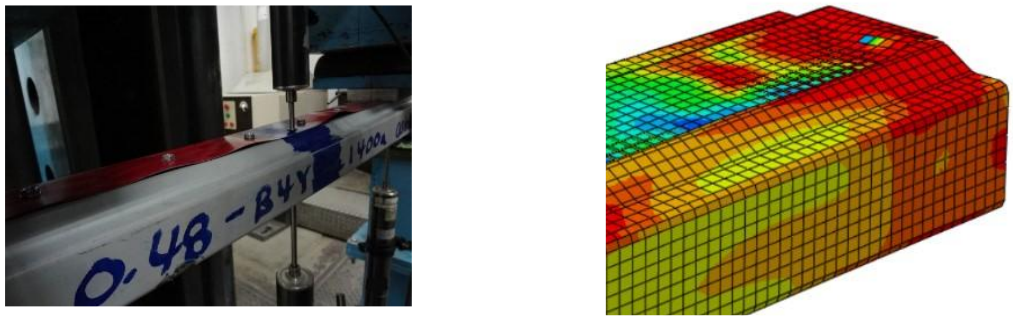

(d) Comparison of experimental [25] and numerical observations of specimen COF-1.0-B4.

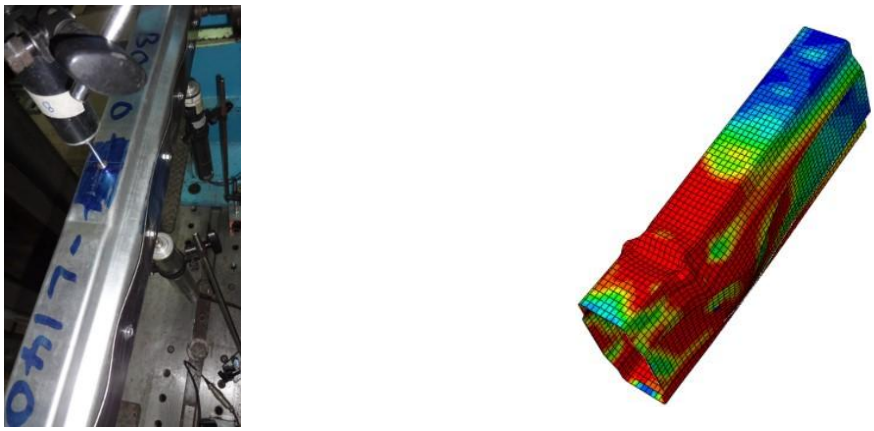

(e) Comparison of experimental [25] and numerical observations of specimen COW-1.0-B4.

Figure 5-5: Comparison of experimental and numerical observations of specimens.

5.5 Concluding remark

Modelling of the cold-formed steel (CFS) built-up sections subjected to four-point bending is computationally expensive due to their intricate structural behaviour, which involves material non-linearities, imperfections, and surface-to-surface contacts. In this chapter, a robust numerical approach developed in Chapter 4, capable of accurately replicating the behaviour of CFS built-up sections, was extended to the experimental test results from several CFS FTF and BTB built-up section connections.

The comparisons demonstrate that the proposed numerical method effectively captures both the structural behaviour and moment capacity of the built-up sections. At the structural level, the approach proves to be computationally efficient in terms of analysis time, accuracy, and easier converge. Moreover, this method can be applied to simulate other types of CFS built-up sections. Consequently, using a similarly efficient computational method, an extensive parametric study is conducted in Chapter 6.

Chapter 6 – Parametric Study

6.1 In general

A parametric study based on 190 validated FE models was conducted on CFS built-up sections with stiffened single channel sections connected with screws in the lip as shown in Figure 6-1. The validated FEA model presented in Chapter 4 was used for this study. The parametric study was divided into two parts: the first part involved a parametric study using the simplified model mentioned in Section 4.3, for which 150 FE models were developed. The second part examined the effect of screws in the web region, as described in Section 4.4, generating 40 FE models. The material properties obtained from the coupon testing mentioned in Appendix "A" were used for both parametric studies. A semi-automated approach was used in which the base models were generated in ABAQUS [44], and then the thickness of the models was changed with Python scripting to generate all the FE models for the parametric study (refer Appendix B-B.2). Additionally, a Python script (refer Appendix B-B.4) was written for post-processing of the data from the generated from the ABAQUS output database (.odb) file. Four types of cross-sections were considered, as shown in Figure 6-1. To determine the moment capacity of the different sections, the following parameters were varied: thicknesses (t) from 0.75 mm to 3 mm, web depths (w_d) from 150 mm to 600 mm, and screw spacing (s) of 75 mm, 150 mm, and 300 mm. The moment capacities of the built-up CFS sections obtained from the FEA are presented in Table 6-1.

Three types of labels were used for the labelling of specimens, as shown in Figure 6-2. For the parametric study, the specimens were labelled to indicate the type of section, web depth, member length, and thickness. For example, the label "N500-L650-S150-T0.75" denotes the specifics as illustrated in Figure 6-2.

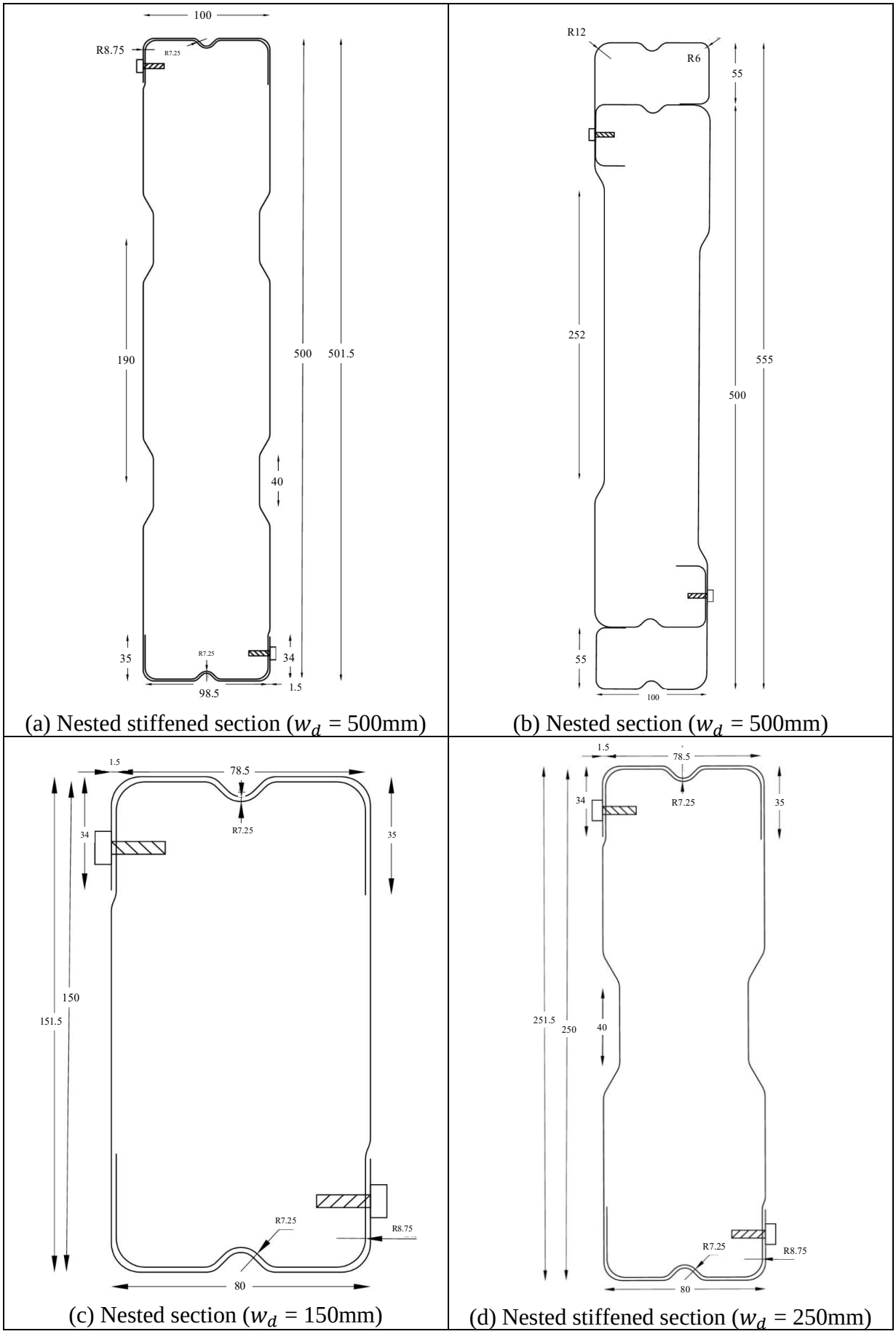

(a) Nested stiffened section (w_d = 500mm)

(b) Nested section (w_d = 500mm)

(c) Nested section (w_d = 150mm)

(d) Nested stiffened section (w_d = 250mm)

Figure 6-1: Cross-sections used in parametric study.

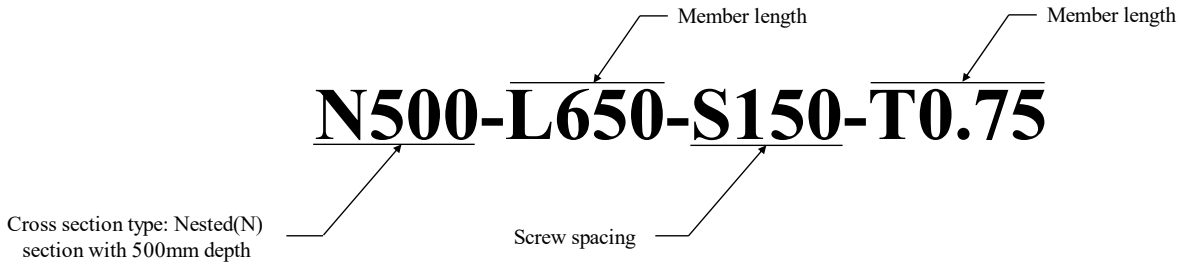

(a) Labelling for Nested section

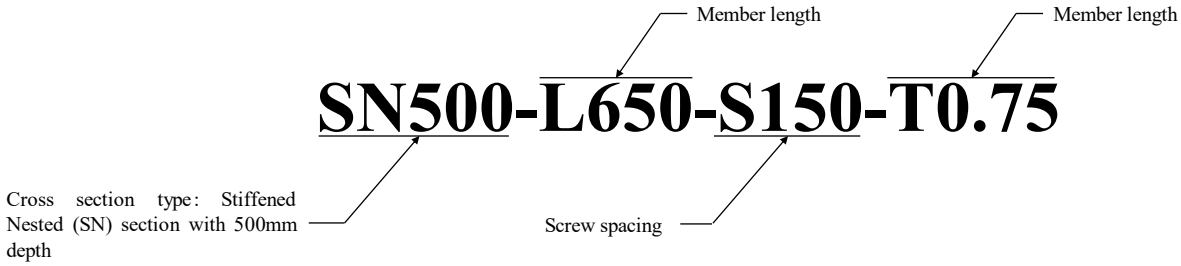

(b) Labelling for Stiffened Nested section

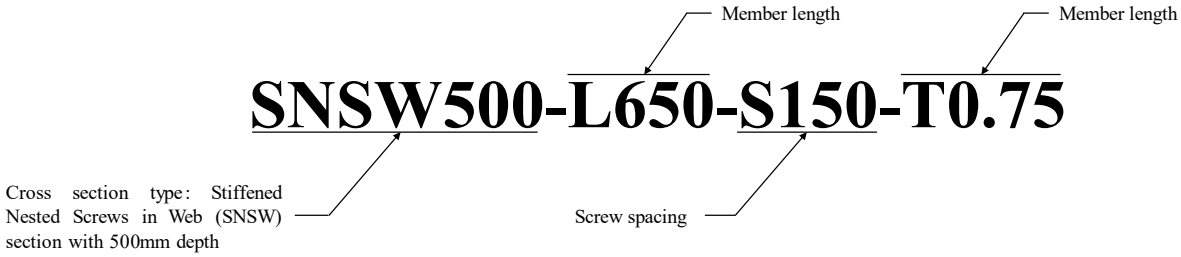

(c) Labelling for Stiffened Nested section with screws in web as shown in Figure 4-10

Figure 6-2: Labelling of specimen.

6.2 Parametric study results

The Table 6-1 presents the results of the parametric study, and the outcomes from the table are discussed in further sections.

Table 6-1: Parametric study results.

Specimen	w_d	l	s	t	M_{FEA}
	mm	mm	mm	mm	$kN \cdot m$
SN500-L650-S75-T0.75	500	650	75	0.75	61.71
SN500-L650-S150-T0.75	500	650	150	0.75	60.87
SN500-L650-S300-T0.75	500	650	300	0.75	59.46
SN500-L650-S75-T1.0	500	650	75	1.00	90.76
SN500-L650-S150-T1.0	500	650	150	1.00	89.26
SN500-L650-S300-T1.0	500	650	300	1.00	90.15
SN500-L650-S75-T1.5	500	650	75	1.50	158.88
SN500-L650-S150-T1.5	500	650	150	1.50	158.31
SN500-L650-S300-T1.5	500	650	300	1.50	157.41
SN500-L650-S75-T2.0	500	650	75	2.00	233.48
SN500-L650-S150-T2.0	500	650	150	2.00	234.05
SN500-L650-S300-T2.0	500	650	300	2.00	235.09
SN500-L650-S75-T3.0	500	650	75	3.00	374.06
SN500-L650-S150-T3.0	500	650	150	3.00	374.14
SN500-L650-S300-T3.0	500	650	300	3.00	374.62
SN450-L650-S75-T0.75	450	650	75	0.75	52.33
SN450-L650-S150-T0.75	450	650	150	0.75	52.18
SN450-L650-S300-T0.75	450	650	300	0.75	53.03
SN450-L650-S75-T1.0	450	650	75	1.00	80.96
SN450-L650-S150-T1.0	450	650	150	1.00	79.39
SN450-L650-S300-T1.0	450	650	300	1.00	79.85
SN450-L650-S75-T1.5	450	650	75	1.50	140.62
SN450-L650-S150-T1.5	450	650	150	1.50	141.92
SN450-L650-S300-T1.5	450	650	300	1.50	141.95
SN450-L650-S75-T2.0	450	650	75	2.00	198.35
SN450-L650-S150-T2.0	450	650	150	2.00	204.87
SN450-L650-S300-T2.0	450	650	300	2.00	204.61
SN450-L650-S75-T3.0	450	650	75	3.00	311.17
SN450-L650-S150-T3.0	450	650	150	3.00	321.60
SN450-L650-S300-T3.0	450	650	300	3.00	320.60
SN400-L650-S75-T0.75	400	650	75	0.75	47.68
SN400-L650-S150-T0.75	400	650	150	0.75	47.71
SN400-L650-S300-T0.75	400	650	300	0.75	47.61
SN400-L650-S75-T1.0	400	650	75	1.00	70.51
SN400-L650-S150-T1.0	400	650	150	1.00	69.49
SN400-L650-S300-T1.0	400	650	300	1.00	70.83
SN400-L650-S75-T1.5	400	650	75	1.50	122.22
SN400-L650-S150-T1.5	400	650	150	1.50	122.09
SN400-L650-S300-T1.5	400	650	300	1.50	122.17
SN400-L650-S75-T2.0	400	650	75	2.00	174.83
SN400-L650-S150-T2.0	400	650	150	2.00	172.72

Specimen	w_d	l	s	t	M_{FEA}
	mm	mm	mm	mm	$kN \cdot m$
SN400-L650-S300-T2.0	400	650	300	2.00	173.76
SN400-L650-S75-T3.0	400	650	75	3.00	272.44
SN400-L650-S150-T3.0	400	650	150	3.00	270.74
SN400-L650-S300-T3.0	400	650	300	3.00	271.14
SN350-L650-S75-T0.75	350	650	75	0.75	42.01
SN350-L650-S150-T0.75	350	650	150	0.75	40.65
SN350-L650-S300-T0.75	350	650	300	0.75	40.86
SN350-L650-S75-T1.0	350	650	75	1.00	60.56
SN350-L650-S150-T1.0	350	650	150	1.00	58.88
SN350-L650-S300-T1.0	350	650	300	1.00	59.42
SN350-L650-S75-T1.5	350	650	75	1.50	105.50
SN350-L650-S150-T1.5	350	650	150	1.50	104.94
SN350-L650-S300-T1.5	350	650	300	1.50	105.27
SN350-L650-S75-T2.0	350	650	75	2.00	143.75
SN350-L650-S150-T2.0	350	650	150	2.00	143.71
SN350-L650-S300-T2.0	350	650	300	2.00	144.32
SN350-L650-S75-T3.0	350	650	75	3.00	225.10
SN350-L650-S150-T3.0	350	650	150	3.00	220.44
SN350-L650-S300-T3.0	350	650	300	3.00	213.10
SN300-L650-S75-T0.75	300	650	75	0.75	33.80
SN300-L650-S150-T0.75	300	650	150	0.75	32.66
SN300-L650-S300-T0.75	300	650	300	0.75	32.43
SN300-L650-S75-T1.0	300	650	75	1.00	48.20
SN300-L650-S150-T1.0	300	650	150	1.00	48.27
SN300-L650-S300-T1.0	300	650	300	1.00	48.19
SN300-L650-S75-T1.5	300	650	75	1.50	84.61
SN300-L650-S150-T1.5	300	650	150	1.50	83.77
SN300-L650-S300-T1.5	300	650	300	1.50	85.05
SN300-L650-S75-T2.0	300	650	75	2.00	114.89
SN300-L650-S150-T2.0	300	650	150	2.00	114.83
SN300-L650-S300-T2.0	300	650	300	2.00	114.81
SN300-L650-S75-T3.0	300	650	75	3.00	179.09
SN300-L650-S150-T3.0	300	650	150	3.00	178.17
SN300-L650-S300-T3.0	300	650	300	3.00	176.56
SN250-L650-S75-T0.75	250	650	75	0.75	11.81
SN250-L650-S150-T0.75	250	650	150	0.75	11.56
SN250-L650-S300-T0.75	250	650	300	0.75	11.50
SN250-L650-S75-T1.0	250	650	75	1.00	16.50
SN250-L650-S150-T1.0	250	650	150	1.00	16.37
SN250-L650-S300-T1.0	250	650	300	1.00	16.37
SN250-L650-S75-T1.5	250	650	75	1.50	28.62
SN250-L650-S150-T1.5	250	650	150	1.50	28.56
SN250-L650-S300-T1.5	250	650	300	1.50	28.56

Specimen	w_d	l	s	t	M_{FEA}
	mm	mm	mm	mm	$kN \cdot m$
SN250-L650-S75-T2.0	250	650	75	2.00	39.43
SN250-L650-S150-T2.0	250	650	150	2.00	39.12
SN250-L650-S300-T2.0	250	650	300	2.00	39.12
SN250-L650-S75-T3.0	250	650	75	3.00	60.99
SN250-L650-S150-T3.0	250	650	150	3.00	60.46
SN250-L650-S300-T3.0	250	650	300	3.00	60.46
SN200-L650-S75-T0.75	200	650	75	0.75	17.67
SN200-L650-S150-T0.75	200	650	150	0.75	17.56
SN200-L650-S300-T0.75	200	650	300	0.75	17.23
SN200-L650-S75-T1.0	200	650	75	1.00	25.59
SN200-L650-S150-T1.0	200	650	150	1.00	25.23
SN200-L650-S300-T1.0	200	650	300	1.00	25.17
SN200-L650-S75-T1.5	200	650	75	1.50	42.49
SN200-L650-S150-T1.5	200	650	150	1.50	42.17
SN200-L650-S300-T1.5	200	650	300	1.50	42.15
SN200-L650-S75-T2.0	200	650	75	2.00	57.80
SN200-L650-S150-T2.0	200	650	150	2.00	57.39
SN200-L650-S300-T2.0	200	650	300	2.00	57.55
SN200-L650-S75-T3.0	200	650	75	3.00	93.35
SN200-L650-S150-T3.0	200	650	150	3.00	93.00
SN200-L650-S300-T3.0	200	650	300	3.00	88.55
N150-L650-S75-T0.75	150	650	75	0.75	11.81
N150-L650-S150-T0.75	150	650	150	0.75	11.56
N150-L650-S300-T0.75	150	650	300	0.75	11.50
N150-L650-S75-T1.0	150	650	75	1.00	16.50
N150-L650-S150-T1.0	150	650	150	1.00	16.37
N150-L650-S300-T1.0	150	650	300	1.00	16.37
N150-L650-S75-T1.5	150	650	75	1.50	28.62
N150-L650-S150-T1.5	150	650	150	1.50	28.56
N150-L650-S300-T1.5	150	650	300	1.50	28.56
N150-L650-S75-T2.0	150	650	75	2.00	39.43
N150-L650-S150-T2.0	150	650	150	2.00	39.12
N150-L650-S300-T2.0	150	650	300	2.00	39.12
N150-L650-S75-T3.0	150	650	75	3.00	60.99
N150-L650-S150-T3.0	150	650	150	3.00	60.46
N150-L650-S300-T3.0	150	650	300	3.00	60.46
N350-L650-S300-T0.75	350	650	300	0.75	47.04
N350-L650-S300-T1.0	350	650	300	1.00	69.05
N350-L650-S300-T1.5	350	650	300	1.50	112.86
N350-L650-S300-T2.0	350	650	300	2.00	157.69
N350-L650-S300-T3.0	350	650	300	3.00	240.17
N400-L650-S300-T0.75	400	650	300	0.75	55.93
N400-L650-S300-T1.0	400	650	300	1.00	79.25

Specimen	w_d	l	s	t	M_{FEA}
	mm	mm	mm	mm	$kN \cdot m$
N400-L650-S300-T1.5	400	650	300	1.50	134.16
N400-L650-S300-T2.0	400	650	300	2.00	192.21
N400-L650-S300-T3.0	400	650	300	3.00	300.34
N450-L650-S300-T0.75	450	650	300	0.75	64.63
N450-L650-S300-T1.0	450	650	300	1.00	95.26
N450-L650-S300-T1.5	450	650	300	1.50	160.59
N450-L650-S300-T2.0	450	650	300	2.00	227.94
N450-L650-S300-T3.0	450	650	300	3.00	354.68
N500-L650-S300-T0.75	500	650	300	0.75	70.47
N500-L650-S300-T1.0	500	650	300	1.00	112.53
N500-L650-S300-T1.5	500	650	300	1.50	190.97
N500-L650-S300-T2.0	500	650	300	2.00	272.85
N500-L650-S300-T3.0	500	650	300	3.00	425.96
N550-L650-S300-T0.75	550	650	300	0.75	81.67
N550-L650-S300-T1.0	550	650	300	1.00	131.65
N550-L650-S300-T1.5	550	650	300	1.50	214.94
N550-L650-S300-T2.0	550	650	300	2.00	325.52
N550-L650-S300-T3.0	550	650	300	3.00	515.68
N600-L650-S300-T0.75	600	650	300	0.75	93.67
N600-L650-S300-T1.0	600	650	300	1.00	152.39
N600-L650-S300-T1.5	600	650	300	1.50	262.61
N600-L650-S300-T2.0	600	650	300	2.00	387.73
N600-L650-S300-T3.0	500	650	300	3.00	617.18
SNSW500-L650-S75-T0.75	500	650	75	0.75	54.04
SNSW500-L650-S75-T1.0	500	650	75	1.00	78.27
SNSW500-L650-S75-T1.5	500	650	75	1.50	133.64
SNSW500-L650-S75-T2.0	500	650	75	2.00	197.20
SNSW500-L650-S75-T3.0	500	650	75	3.00	339.92
SNSW450-L650-S75-T0.75	450	650	75	0.75	38.76
SNSW450-L650-S75-T1.0	450	650	75	1.00	59.49
SNSW450-L650-S75-T1.5	450	650	75	1.50	112.26
SNSW450-L650-S75-T2.0	450	650	75	2.00	165.73
SNSW450-L650-S75-T3.0	450	650	75	3.00	278.38
SNSW400-L650-S75-T0.75	400	650	75	0.75	33.07
SNSW400-L650-S75-T1.0	400	650	75	1.00	50.51
SNSW400-L650-S75-T1.5	400	650	75	1.50	95.45
SNSW400-L650-S75-T2.0	400	650	75	2.00	141.00
SNSW400-L650-S75-T3.0	400	650	75	3.00	231.83
SNSW350-L650-S75-T0.75	350	650	75	0.75	28.07
SNSW350-L650-S75-T1.0	350	650	75	1.00	41.80
SNSW350-L650-S75-T1.5	350	650	75	1.50	54.39
SNSW350-L650-S75-T2.0	350	650	75	2.00	68.88
SNSW350-L650-S75-T3.0	350	650	75	3.00	121.94

Specimen	w_d	l	s	t	M_{FEA}
	mm	mm	mm	mm	$kN \cdot m$
SNSW300-L650-S75-T0.75	300	650	75	0.75	23.86
SNSW300-L650-S75-T1.0	300	650	75	1.00	36.28
SNSW300-L650-S75-T1.5	300	650	75	1.50	62.98
SNSW300-L650-S75-T2.0	300	650	75	2.00	90.73
SNSW300-L650-S75-T3.0	300	650	75	3.00	150.99
SNSW250-L650-S75-T0.75	250	650	75	0.75	15.36
SNSW250-L650-S75-T1.0	250	650	75	1.00	23.94
SNSW250-L650-S75-T1.5	250	650	75	1.50	41.33
SNSW250-L650-S75-T2.0	250	650	75	2.00	60.71
SNSW250-L650-S75-T3.0	250	650	75	3.00	101.75
SNSW200-L650-S75-T0.75	200	650	75	0.75	12.01
SNSW200-L650-S75-T1.0	200	650	75	1.00	17.64
SNSW200-L650-S75-T1.5	200	650	75	1.50	30.55
SNSW200-L650-S75-T2.0	200	650	75	2.00	45.22
SNSW200-L650-S75-T3.0	200	650	75	3.00	74.11
NSW150-L650-S75-T0.75	150	650	75	0.75	6.33
NSW150-L650-S75-T1.0	150	650	75	1.00	9.58
NSW150-L650-S75-T1.5	150	650	75	1.50	17.52
NSW150-L650-S75-T2.0	150	650	75	2.00	26.74
NSW150-L650-S75-T3.0	150	650	75	3.00	45.69

6.3 Effect of web depth (w_d)

Figure 6-3 and Figure 6-4 demonstrates the influence of web depth on the moment capacity of CFS built-up box sections under bending. As shown in Figure 6-3, the moment capacity of stiffened nested sections increased by 249.24% for a web depth increase from 200 mm to 500 mm with a thickness of 0.75 mm, and by 374.06% for a thickness of 3.00 mm. A similar trend is observed in Figure 6-4, where the moment capacity of the nested section increased by 99.15% and 156.98% for web depth increases from 350 mm to 600 mm for thicknesses of 0.75 mm and 3.00 mm, respectively.

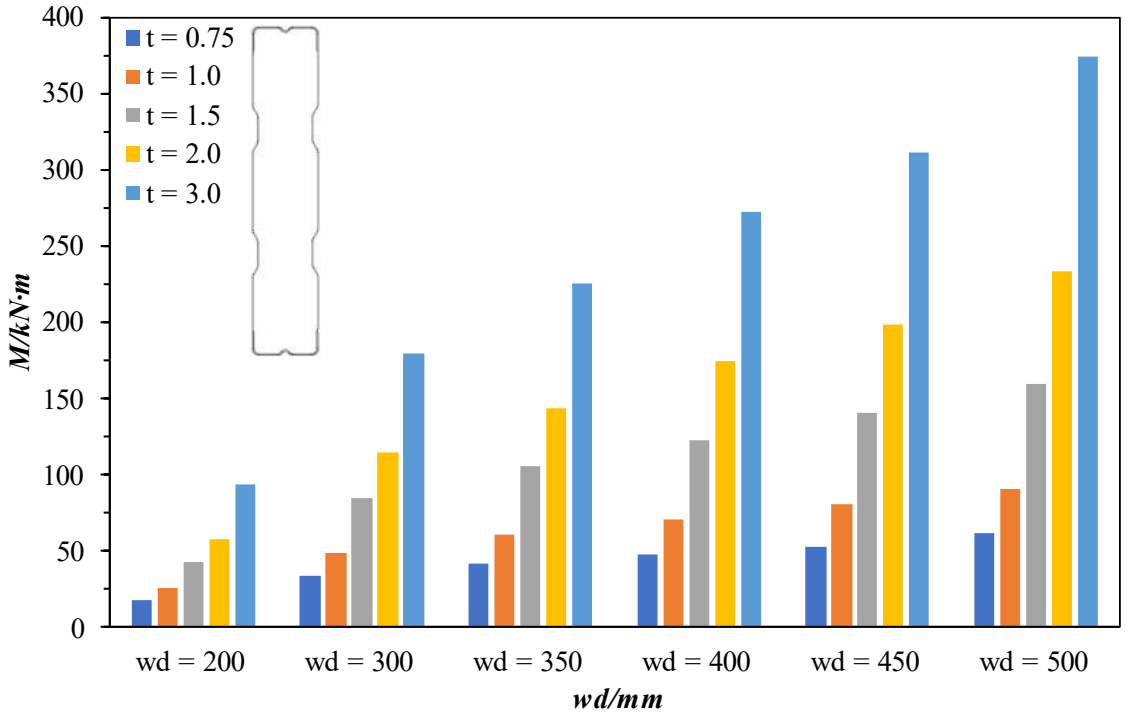

Figure 6-3: Effect of change in w_d for stiffened nested section.

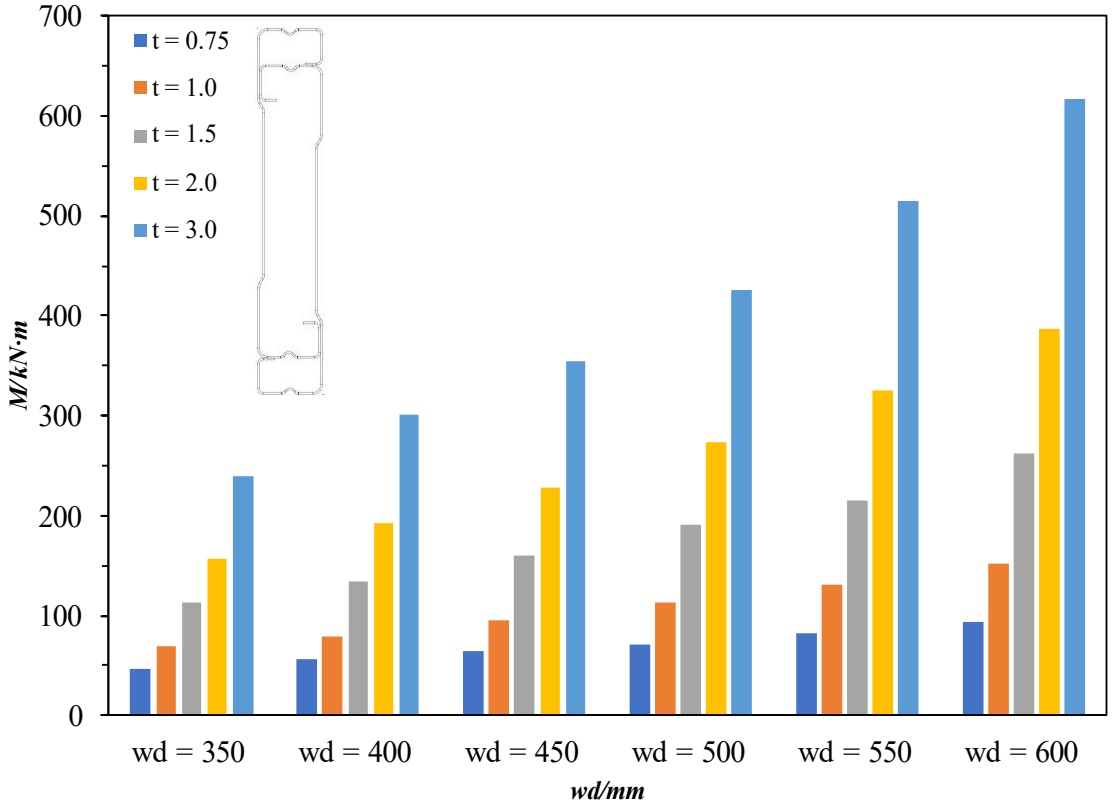

Figure 6-4: Effect of change in w_d for nested section.

6.4 Effect of section thickness (t)

Figure 6-5 demonstrates the influence of section thickness on the moment capacity of CFS built-up stiffened box sections under bending. For a section with a web depth of 500 mm, an increase in thickness leads to a corresponding increase in moment capacity. Specifically, the moment capacities for thicknesses of 0.75 mm, 1.00 mm, 1.5 mm, 2.00 mm, and 3.00 mm are 61.71 kN·m, 90.76 kN·m, 158.88 kN·m, 233.48 kN·m, and 374.06 kN·m, respectively. This shows a 157.46% increase in moment capacity when the thickness is raised from 0.75 mm to 1.5 mm. A further increase to 3 mm results in an additional 118.44% increase in moment capacity compared to the 1.5 mm thickness. Overall, the moment capacity increases by 462.41% when the thickness is increased from 0.75 mm to 3.00 mm.

Similarly, for the same cross-section with a web depth of 200 mm, the moment capacities for thicknesses of 0.75 mm, 1.00 mm, 1.5 mm, 2.00 mm, and 3.00 mm are 17.67 kN·m, 25.59 kN·m, 42.49 kN·m, 57.80 kN·m, and 93.35 kN·m, respectively. This indicates a 140.46% increase in moment capacity when the thickness is increased from 0.75 mm to 1.5 mm. Additionally, increasing the thickness to 3 mm leads to a further 119.7% increase in moment capacity compared to the 1.5 mm thickness. Overall, the moment capacity increases by 428.30% when the thickness is raised from 0.75 mm to 3.00 mm. These findings clearly indicate that section thickness significantly impacts the moment capacity of stiffened box sections under bending.

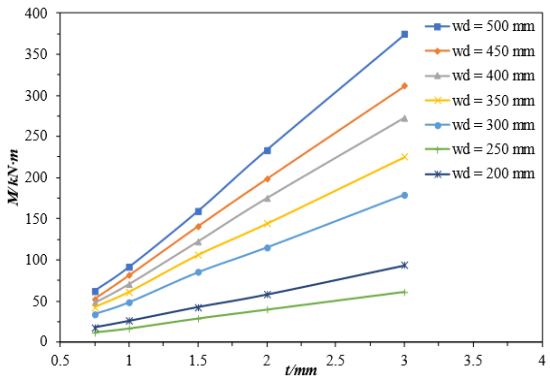

(a) S = 75 mm

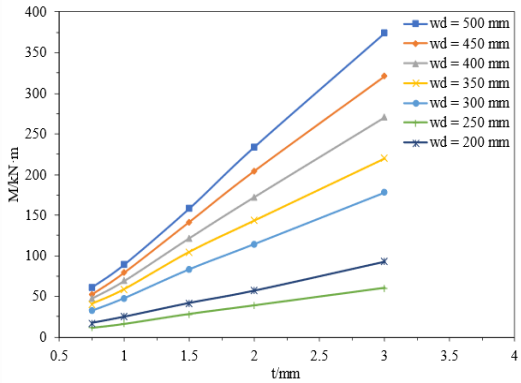

(b) S = 150 mm

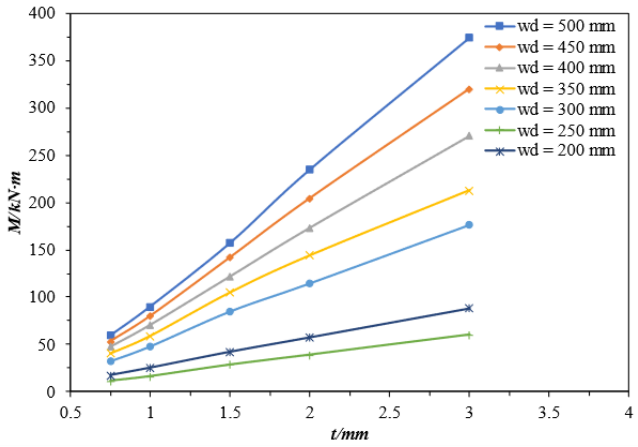

(c) S = 300 mm

Figure 6-5: Effect of thickness on the moment capacity of the built-up CFS stiffened beam.

6.5 Effect of change in the positioning of the channel sections

Figure 6-6 shows the impact of changing the position of the channel sections referred to as nested and stiffened nested built-up box sections (as shown in Figure 6-1) on the moment capacity of the sections with web depths of 350 mm, 400 mm, 450 mm, and 500 mm. The data shows that the moment capacity of the nested box section increases by 13.70%, 10.63%, 10.77%, and 12.70% compared to the stiffened nested box section for web depths of 350 mm, 400 mm, 450 mm, and 500 mm respectively. On average, the moment capacity of the nested box section is 11.95% higher than that of the stiffened nested box section. The reason for this increase could be attributed to the flange of the channel section functioning as a stiffener in the nested box section.

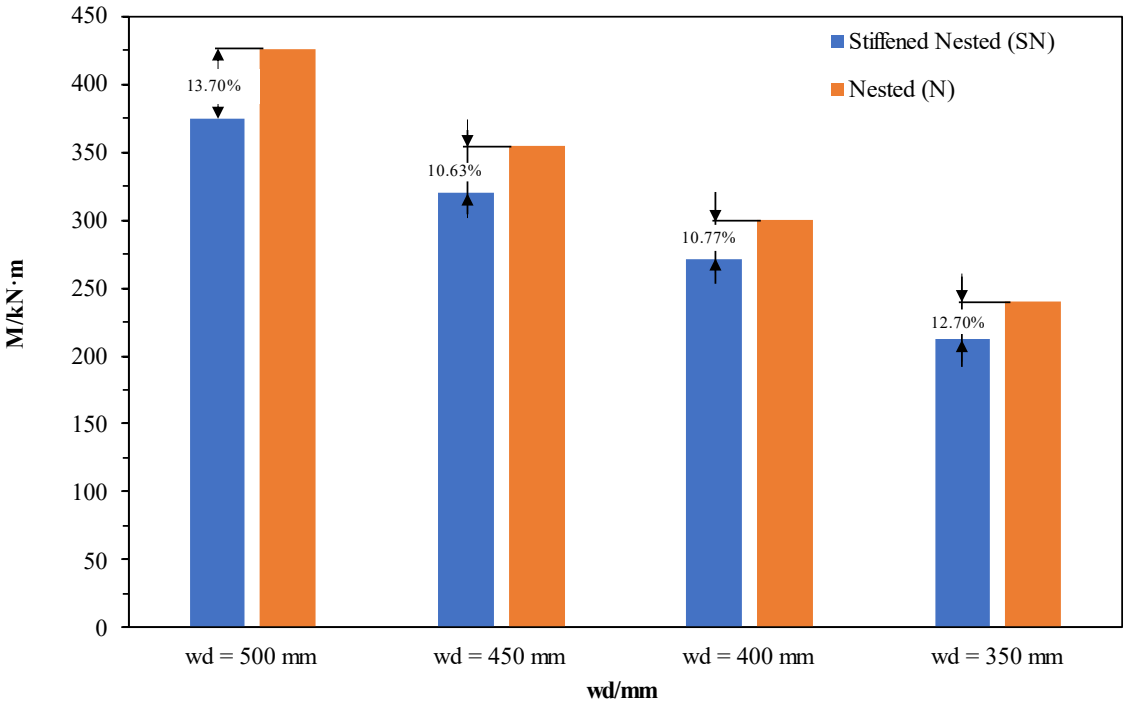

Figure 6-6: Effect of change in the positioning of the channel sections.

6.6 Effect of screw spacing on CFS built-up section

Figure 6-7 shows the effect of screw spacing (75 mm, 150 mm, and 300 mm) on the moment capacity of cold-formed steel (CFS) built-up stiffened box sections with web depths of 200 mm, 250 mm, 300 mm, 350 mm, 400 mm, 450 mm, and 500 mm under bending. The data indicates that screw spacing has a minimal effect on the moment capacity of the built-up box sections, with the percentage change in capacity being less than 2%. Furthermore, previous studies have shown a similar negligible impact on the moment capacity of built-up beams when screw spacing exceeds 300 mm [7].

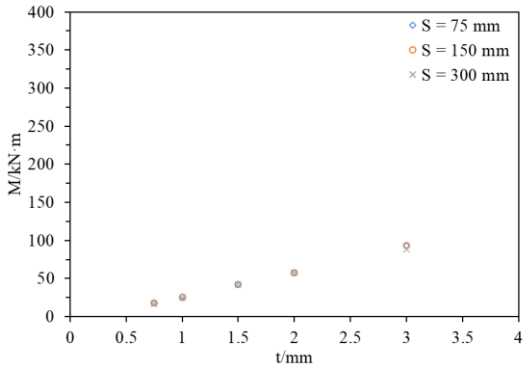

(a) SN200

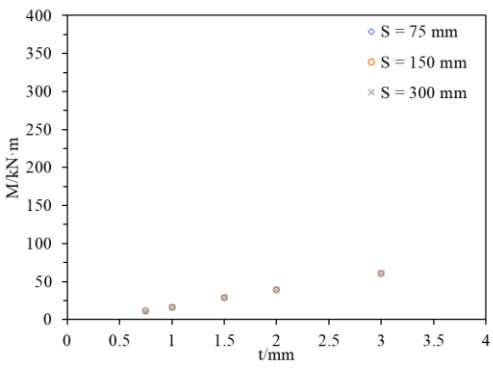

(b) SN250

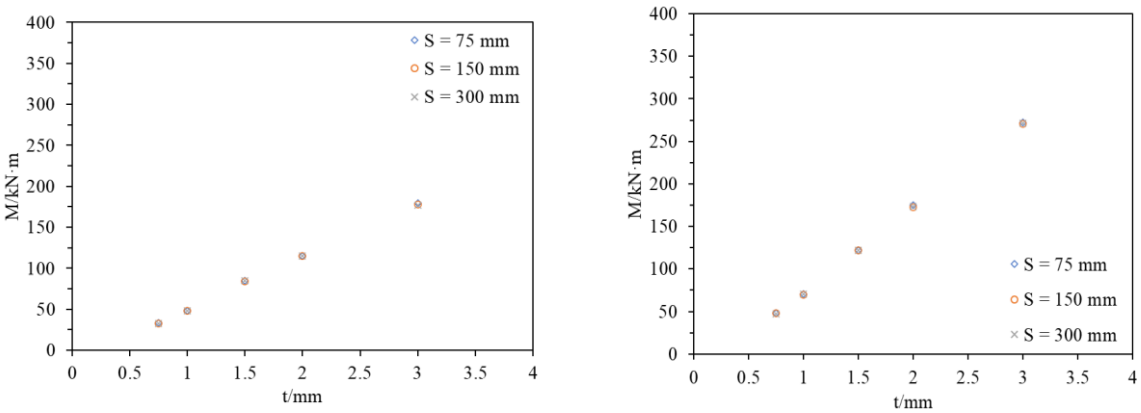

(c) SN300

(d) SN350

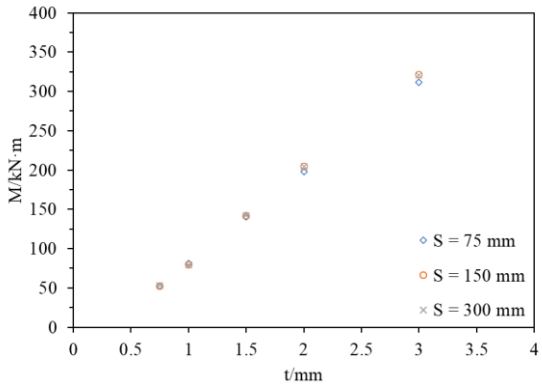

(e) SN400

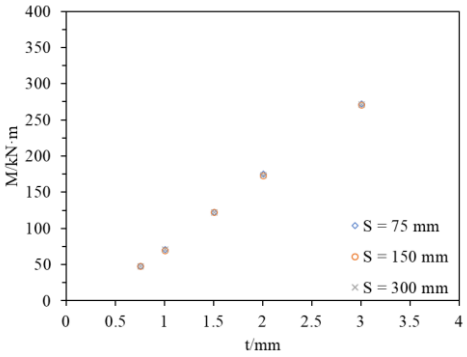

(f) SN450

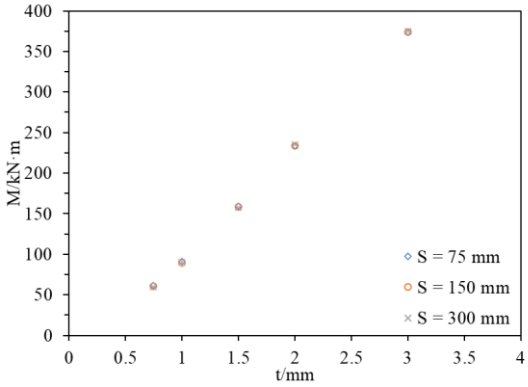

(g) SN500

Figure 6-7: Effect of screw spacing on moment capacity of SN sections for varying web depth.

6.7 Effect of longitudinal screws on the built-up sections

Furthermore, to simulate the practical condition a parametric study was carried out presented in Table 6-2 to see the effect of screws in the web regions as described in section 4.4. As can be seen, the moment capacity of the stiffened nested section with screws in the web has a lesser moment capacity than the corresponding stiffened nested sections this was accounted due to the effect of large warping deformations and bimoment as detailed in section 4.5.2. The

average ratio of moment capacity ($M_{FEA_{SNSW}}$ / $M_{FEA_{SN}}$) for the web depth of 150 mm, 200 mm, 300 mm, 350 mm, 400 mm, 450 mm, 500 mm is 0.63, 0.73, 0.77, 0.58, 0.77, 0.80, 0.87, respectively.

Table 6-2: Effect of screws in the longitudinal direction.

Specimen		w_d	l	s	t	$M_{FEA_{SN}}$	$M_{FEA_{SNSW}}$	$M_{FEA_{SNSW}}$ / $M_{FEA_{SN}}$
SN	SNSW	mm	mm	mm	mm	$kN \cdot m$	$kN \cdot m$	
SN500-L650-S75-T0.75	SNSW500-L650-S75-T0.75	500	650	75	0.75	61.71	54.04	0.88
SN500-L650-S75-T1.0	SNSW500-L650-S75-T1.0	500	650	75	1.00	90.76	78.27	0.86
SN500-L650-S75-T1.5	SNSW500-L650-S75-T1.5	500	650	75	1.50	158.88	133.64	0.84
SN500-L650-S75-T2.0	SNSW500-L650-S75-T2.0	500	650	75	2.00	233.48	197.20	0.84
SN500-L650-S75-T3.0	SNSW500-L650-S75-T3.0	500	650	75	3.00	374.06	339.92	0.91
SN450-L650-S75-T0.75	SNSW450-L650-S75-T0.75	450	650	75	0.75	52.33	38.76	0.74
SN450-L650-S75-T1.0	SNSW450-L650-S75-T1.0	450	650	75	1.00	80.96	59.49	0.73
SN450-L650-S75-T1.5	SNSW450-L650-S75-T1.5	450	650	75	1.50	140.62	112.26	0.80
SN450-L650-S75-T2.0	SNSW450-L650-S75-T2.0	450	650	75	2.00	198.35	165.73	0.84
SN450-L650-S75-T3.0	SNSW450-L650-S75-T3.0	450	650	75	3.00	311.17	278.38	0.89
SN400-L650-S75-T0.75	SNSW400-L650-S75-T0.75	400	650	75	0.75	47.68	33.07	0.69
SN400-L650-S75-T1.0	SNSW400-L650-S75-T1.0	400	650	75	1.00	70.51	50.51	0.72
SN400-L650-S75-T1.5	SNSW400-L650-S75-T1.5	400	650	75	1.50	122.22	95.45	0.78
SN400-L650-S75-T2.0	SNSW400-L650-S75-T2.0	400	650	75	2.00	174.83	141.00	0.81
SN400-L650-S75-T3.0	SNSW400-L650-S75-T3.0	400	650	75	3.00	272.44	231.83	0.85
SN350-L650-S75-T0.75	SNSW350-L650-S75-T0.75	350	650	75	0.75	42.012	28.07	0.67
SN350-L650-S75-T1.0	SNSW350-L650-S75-T1.0	350	650	75	1.00	60.56	41.80	0.69
SN350-L650-S75-T1.5	SNSW350-L650-S75-T1.5	350	650	75	1.50	105.5	54.39	0.52
SN350-L650-S75-T2.0	SNSW350-L650-S75-T2.0	350	650	75	2.00	143.75	68.88	0.48
SN350-L650-S75-T3.0	SNSW350-L650-S75-T3.0	350	650	75	3.00	225.1	121.94	0.54
SN300-L650-S75-T0.75	SNSW300-L650-S75-T0.75	300	650	75	0.75	33.8	23.86	0.71
SN300-L650-S75-T1.0	SNSW300-L650-S75-T1.0	300	650	75	1.00	48.2	36.28	0.75
SN300-L650-S75-T1.5	SNSW300-L650-S75-T1.5	300	650	75	1.50	84.61	62.98	0.74
SN300-L650-S75-T2.0	SNSW300-L650-S75-T2.0	300	650	75	2.00	114.89	90.73	0.79
SN300-L650-S75-T3.0	SNSW300-L650-S75-T3.0	300	650	75	3.00	179.09	150.99	0.84
SN200-L650-S75-T0.75	SNSW200-L650-S75-T0.75	200	650	75	0.75	17.67	12.01	0.68
SN200-L650-S75-T1.0	SNSW200-L650-S75-T1.0	200	650	75	1.00	25.59	17.64	0.69
SN200-L650-S75-T1.5	SNSW200-L650-S75-T1.5	200	650	75	1.50	42.49	30.55	0.72
SN200-L650-S75-T2.0	SNSW200-L650-S75-T2.0	200	650	75	2.00	57.8	45.22	0.78
SN200-L650-S75-T3.0	SNSW200-L650-S75-T3.0	200	650	75	3.00	93.35	74.11	0.79
N150-L650-S75-T0.75	NSW150-L650-S75-T0.75	150	650	75	0.75	11.81	6.33	0.54
N150-L650-S75-T1.0	NSW150-L650-S75-T1.0	150	650	75	1.00	16.5	9.58	0.58
N150-L650-S75-T1.5	NSW150-L650-S75-T1.5	150	650	75	1.50	28.62	17.52	0.61
N150-L650-S75-T2.0	NSW150-L650-S75-T2.0	150	650	75	2.00	39.43	26.74	0.68
N150-L650-S75-T3.0	NSW150-L650-S75-T3.0	150	650	75	3.00	60.99	45.69	0.75

Chapter 7 – Conclusion and future works

7.1 Introductory remarks

The aim of this research was to develop a computationally efficient simplified model without compromising the accuracy of results. The study focused on investigating the moment capacity of CFS built-up sections, specifically looking at both stiffened nested and nested configurations. The simplified FE model incorporated nonlinear material properties and initial geometric imperfections. It was validated against experimental results reported by Dai et al. [7] and Wang and Young [25], showing good agreement in terms of failure modes and ultimate moment capacity. Following validation, a comprehensive parametric study was conducted using 190 FE models based on the validated simplified FE model. The validated FE models were used to examine the effects of web depth, section thickness, channel section positioning, and the impact of screws on the web in determining the reduction in moment capacity under practical conditions, such as beam-beam or beam-column connections.

7.2 Conclusion

A simplified nonlinear finite-element modelling technique was developed to evaluate the moment capacity of cold-formed steel (CFS) built-up beams. This method was subsequently used to validate experimental test results for both moment capacity and failure modes. The simplified model demonstrated strong agreement in predicting moment capacity and accurately representing failure modes when compared to the experimental results.

However, the limitations and conditions of the FE models can be summarized as follows: (1) the boundary conditions in the simplified FE models were calibrated based on those used in the four-point bending model, (2) the friction factor was determined through the calibration of the FE models, (3) screw connections were simplified and idealized in the FE models rather than physically modelling the screws.

The validated FE models were then utilized to conduct a parametric study with 190 models to explore how various parameters affect the bending capacity of CFS built-up stiffened nested and nested sections. The results of this study revealed that key factors such as thickness, web depth, the positioning of the channel section, and the impact of screws on the web significantly influence the moment capacity of these sections.

The conclusions from the present study are given as follows:

- A simplified model was developed as an alternative to the traditional four-point bending model and was validated based on its moment capacity and deformed shape.
- The simplified model was derived from the full-scale four-point bending setup by applying the appropriate boundary conditions. A key simplification involved reducing the length of the section by about 18% compared to the full model. This reduction also minimized the contact area between the single-channel sections forming the built-up section, thereby decreasing the number of screws required for connections. Furthermore, simplified boundary conditions were applied to assess the moment capacity of the section. The resulting model, with these adjustments, accurately predicted the moment capacity with a negligible margin of error when compared to both experimental results and FEA outcomes from the full-scale four-point bending model.
- A study was conducted to compare the reduction in computational time across all three models (i.e., the four-point bending model, pure-bending model, and simplified model). The results demonstrated a significant decrease in CPU time for analysis. The simplified model required 97.81% less computational time than the four-point bending model, while maintaining the accuracy of the results when compared to experimental tests. This substantial reduction in computational time was attributed to the decreased number of elements needed to develop the simplified FE model.

- The simplified model was modified to include screws at one end to simulate beam-beam and beam-column connections. The moment capacity of the screw-web model was lower than that of the simplified model. This difference was attributed to the load transfer mechanism in CFS screw moment connections, which primarily occurs through the screw group in the web of the built-up beam elements, leading to significant bimoment and warping deformations. To analyse the variation in moment capacity, both models were used in an extensive parametric study.
- A parametric study for varying range of parameters was conducted, including web depths (w_d) from 150 to 600 mm, screw spacings (s) from 75 to 300 mm (used to connect two single-channel sections to form the built-up section), thicknesses (t) from 0.75 to 3.00 mm, and the impact of longitudinal screws in the web. Two types of sections were analysed: stiffened nested and nested sections.
- The parametric study results showed that increasing web depth improved the moment capacity for both stiffened nested and nested sections. For stiffened nested sections with web depths between 200 mm and 500 mm, the average increase in moment capacity was 26.01% for thicknesses ranging from 0.75 mm to 3.00 mm. Similarly, for nested sections with web depths between 350 mm and 600 mm, the average moment capacity increased by 16.63% for the same range of thicknesses. Therefore, the study revealed that section thickness has a significant effect on moment capacity. The spacing between screws used to connect channel sections for forming built-up beams had a negligible effect on the moment capacity under bending. However, the longitudinal screws in the web had a significant influence on the moment capacity of the built-up beams, with an average reduction of 26.43% in capacity observed.

- The study also found that the stiffened nested sections exhibited lower moment capacity compared to nested sections, indicating that the positioning of the sections affects the moment capacity of built-up beams.

7.3 Limitations of the study

These are the limitations of the current study:

- Only one channel length (l = 650 mm, which is half the length of the pure bending model with a length of 1300 mm, as shown in Figure 4-1) was considered. However, previous research suggests that the length of the sections also influences the structural behaviour and moment capacity of built-up sections.
- The structural performance of the built-up sections was evaluated only for bending, excluding other loading conditions such as shear, web crippling, and combinations of bending, shear, and web crippling.
- In this study, screws in the longitudinal direction of the web were arranged in a linear pattern with three screws horizontally and four vertically. For a more practical scenario, a circular pattern of screws could also be used. Additionally, the distance between the screws was set to one-third of the web depth, which can be adjusted based on specific requirements.

7.4 Recommendations

- To determine the moment capacity of the box section, it is important to understand the effect of screws in the longitudinal direction. This will help determine the true moment capacity of the section under bending, allowing designers to create safer cross-sections. Since there are no existing design guidelines for these built-up sections, performing a FE analysis on such sections with screws in the web can provide an accurate measure of their moment capacity. Also, the designer can consider various screw patterns which

will be required according to the on-site conditions to accurately measure the strength of the section.

- Additionally, the simplified model developed in this study can help designers assess the moment capacity of various types and shapes of built-up sections more efficiently. This approach reduces both computational time and the effort needed to set up a full four-point bending test in any finite element software. By using this model, designers can save time and streamline their analysis process.
- Furthermore, screw spacing does not significantly impact the moment capacity of the built-up sections, so a larger spacing between screws can be used. However, it is important to consider other criteria such as serviceability criteria when determining the optimal screw spacing to be used.
- Finally, the placement of the single-channel section within the built-up sections significantly influences the moment capacity. Based on this study, it is recommended to use a configuration similar to the Nested section, as shown in Figure 6-1 (b), rather than the Stiffened Nested section depicted in Figure 6-1 (a). This is because the moment capacity of the Nested section was found to be greater than that of the Stiffened Nested section for the same depth.

7.5 Future works

From the present study and previous observed studies, future scopes are found.

1. The study can be extended to investigate the effects of various loading conditions, including shear, web crippling, and combinations of bending, shear, and web crippling.
2. The built-up sections can be tested under dynamic loads to observe the behaviour of such beams with various configurations and cross-sectional dimensions.
3. The research could be expanded to explore different materials.

4. Different screw configurations on the web can be analysed according to specific user needs and optimised as required.
5. The effects of varying thicknesses and lengths can be examined.
6. Web holes can be introduced in the built-up sections in different forms, such as slotted, edge-stiffened, or stiffened, to accommodate various utilities and services.
7. FE modelling of beam-beam and beam-column connections under cyclic loading can also be performed.
8. Cross-section optimisation can be explored.

References

[1] G. J. Hancock, "Cold-formed steel structures," *J Constr Steel Res*, vol. 59, no. 4, pp. 473–487, 2003, doi: 10.1016/S0143-974X(02)00103-7.

[2] Wei-Wen Yu, Roger A. Laboube, and Helen Chen, *Cold-formed steel design*. 2020.

[3] F. J. Meza, J. Becque, and I. Hajirasouliha, "Experimental Study of Cold-Formed Steel Built-Up Beams," *Journal of Structural Engineering*, vol. 146, no. 7, Jul. 2020, doi: 10.1061/(asce)st.1943-541x.0002677.

[4] Y. Dai, K. Roy, Z. Fang, G. M. Raftery, K. Ghosh, and J. B. P. Lim, "A critical review of cold-formed built-up members: Developments, challenges, and future directions," Oct. 01, 2023, *Elsevier Ltd*. doi: 10.1016/j.jobe.2023.107255.

[5] J. B. P. Lim and D. A. Nethercot, "Ultimate strength of bolted moment-connections between cold-formed steel members," *Thin-Walled Structures*, vol. 41, no. 11, pp. 1019–1039, Nov. 2003, doi: 10.1016/S0263-8231(03)00045-4.

[6] H. B. Blum and K. J. R. Rasmussen, "Experimental and numerical study of connection effects in long-span cold-formed steel double channel portal frames," *J Constr Steel Res*, vol. 155, pp. 480–491, Apr. 2019, doi: 10.1016/j.jcsr.2018.11.013.

[7] Y. Dai, G. M. Raftery, K. Roy, I. Hajirasouliha, Z. Fang, and B. Chen, "Flexural behavior of novel unsymmetrical cold-formed steel built-up stiffened box sections: experimental and numerical investigations 2."

[8] B. Chen, K. Roy, A. Uzzaman, and J. B. P. Lim, "Moment capacity of cold-formed channel beams with edge-stiffened web holes, un-stiffened web holes and plain webs," *Thin-Walled Structures*, vol. 157, Dec. 2020, doi: 10.1016/j.tws.2020.107070.

[9] "American Iron, Steel Institute, AISI, North American Specification for the Design of Cold-Formed Steel Structural Members, American Iron and Steel Institute, Washington, DC, 2016".

[10] Australia/New Zealand Standard (AS/NZS), Cold-Formed Steel Structures, AS/NZS 4600:2018. Standards Australia/ Standards New Zealand, 2018.

[11] C. D. Moen and B. W. Schafer, "Elastic buckling of cold-formed steel columns and beams with holes," *Eng Struct*, vol. 31, no. 12, pp. 2812–2824, Dec. 2009, doi: 10.1016/j.engstruct.2009.07.007.

[12] C. D. Moen, A. Schudlich, and A. von der Heyden, "Experiments on Cold-Formed Steel C-Section Joists with Unstiffened Web Holes," *Journal of Structural Engineering*, vol. 139, no. 5, pp. 695–704, May 2013, doi: 10.1061/(asce)st.1943-541x.0000652.

[13] J. Zhao, K. Sun, C. Yu, and J. Wang, “Tests and direct strength design on cold-formed steel channel beams with web holes,” *Eng Struct*, vol. 184, pp. 434–446, Apr. 2019, doi: 10.1016/j.engstruct.2019.01.062.

[14] N. ting Yu, B. Kim, W. bin Yuan, L. yuan Li, and F. Yu, “An analytical solution of distortional buckling resistance of cold-formed steel channel-section beams with web openings,” *Thin-Walled Structures*, vol. 135, pp. 446–452, Feb. 2019, doi: 10.1016/j.tws.2018.11.012.

[15] N. ting Yu, B. Kim, L. yuan Li, W. jian Hong, and W. bin Yuan, “Distortional buckling of perforated cold-formed steel beams subject to uniformly distributed transverse loads,” *Thin-Walled Structures*, vol. 148, Mar. 2020, doi: 10.1016/j.tws.2019.106569.

[16] K. Thirunavukkarasu *et al.*, “Flexural behaviour and design rules for SupaCee sections with web openings,” *Journal of Building Engineering*, vol. 63, Jan. 2023, doi: 10.1016/j.jobe.2022.105539.

[17] N. Degtyareva, P. Gatheeshgar, K. Poologanathan, S. Gunalan, K. D. Tsavdaridis, and S. Napper, “New distortional buckling design rules for slotted perforated cold-formed steel beams,” *J Constr Steel Res*, vol. 168, May 2020, doi: 10.1016/j.jcsr.2020.106006.

[18] N. Degtyareva, P. Gatheeshgar, K. Poologanathan, S. Gunalan, I. Shyha, and A. McIntosh, “Local buckling strength and design of cold-formed steel beams with slotted perforations,” *Thin-Walled Structures*, vol. 156, Nov. 2020, doi: 10.1016/j.tws.2020.106951.

[19] C. Yu, “Cold-formed steel flexural member with edge stiffened holes: Behavior, optimization, and design,” *J Constr Steel Res*, vol. 71, pp. 210–218, Apr. 2012, doi: 10.1016/j.jcsr.2011.09.008.

[20] Y. Dai, K. Roy, Z. Fang, B. Chen, G. M. Raftery, and J. B. P. Lim, “A novel machine learning model to predict the moment capacity of cold-formed steel channel beams with edge-stiffened and un-stiffened web holes,” *Journal of Building Engineering*, vol. 53, Aug. 2022, doi: 10.1016/j.jobe.2022.104592.

[21] B. Chea, T. Chaisomphob, W. Patwichaichote, and E. Yamaguchi, “Experimental and Numerical Study on Cold-formed Steel Built-up Box Beams.”

[22] L. Wang and B. Young, “Design of cold-formed steel built-up sections with web perforations subjected to bending,” *Thin-Walled Structures*, vol. 120, pp. 458–469, Nov. 2017, doi: 10.1016/j.tws.2017.06.016.

[23] “North American Specification for the Design of Cold-Formed Steel Structural Members and the Commentary”.

[24] L. Wang and B. Young, “Behaviour and design of cold-formed steel built-up section beams with different screw arrangements,” *Thin-Walled Structures*, vol. 131, pp. 16–32, Oct. 2018, doi: 10.1016/j.tws.2018.06.022.

[25] L. Wang and B. Young, “Behavior of Cold-Formed Steel Built-Up Sections with Intermediate Stiffeners under Bending. I: Tests and Numerical Validation,” *Journal of Structural Engineering*, vol. 142, no. 3, Mar. 2016, doi: 10.1061/(asce)st.1943-541x.0001428.

[26] M. Anbarasu, “Simulation of flexural behaviour and design of cold-formed steel closed built-up beams composed of two sigma sections for local buckling,” *Eng Struct*, vol. 191, pp. 549–562, Jul. 2019, doi: 10.1016/j.engstruct.2019.04.093.

[27] M. G. Sahab, A. F. Ashour, and V. V. Toropov, “Cost optimisation of reinforced concrete flat slab buildings,” *Eng Struct*, vol. 27, no. 3, pp. 313–322, Feb. 2005, doi: 10.1016/j.engstruct.2004.10.002.

[28] A. Kohoutkova and I. Broukalova, “Optimization of fibre reinforced concrete structural members,” in *Procedia Engineering*, Elsevier Ltd, 2013, pp. 100–106. doi: 10.1016/j.proeng.2013.09.018.

[29] S. Eleftheriadis, P. Duffour, P. Greening, J. James, B. Stephenson, and D. Mumovic, “Investigating relationships between cost and CO2 emissions in reinforced concrete structures using a BIM-based design optimisation approach,” *Energy Build*, vol. 166, pp. 330–346, May 2018, doi: 10.1016/j.enbuild.2018.01.059.

[30] H. Afshari, W. Hare, and S. Tesfamariam, “Constrained multi-objective optimization algorithms: Review and comparison with application in reinforced concrete structures,” *Applied Soft Computing Journal*, vol. 83, Oct. 2019, doi: 10.1016/j.asoc.2019.105631.

[31] R. Pierott, A. W. A. Hammad, A. Haddad, S. Garcia, and G. Falcón, “A mathematical optimisation model for the design and detailing of reinforced concrete beams,” *Eng Struct*, vol. 245, Oct. 2021, doi: 10.1016/j.engstruct.2021.112861.

[32] G. Chobe, S. Selvaraj, and M. Madhavan, “Numerical Study on Retrofitting of Hot Rolled Steel Beams with Cold-formed Steel Encased Channels-Design Concept using Machine Learning Method,” *Eng Struct*, vol. 297, Dec. 2023, doi: 10.1016/j.engstruct.2023.116972.

[33] H. Liang, K. Roy, Z. Fang, and J. B. P. Lim, “A Critical Review on Optimization of Cold-Formed Steel Members for Better Structural and Thermal Performances,” Jan. 01, 2022, *MDPI*. doi: 10.3390/buildings12010034.

[34] S. M. Mojtabaei, J. Ye, and I. Hajirasouliha, “Development of optimum cold-formed steel beams for serviceability and ultimate limit states using Big Bang-Big Crunch optimisation,” *Eng Struct*, vol. 195, pp. 172–181, Sep. 2019, doi: 10.1016/j.engstruct.2019.05.089.

[35] “Eurocode 3-Design of steel structures-Part 1-3: General rules-Supplementary rules for cold-formed members and sheeting,” 2006.

[36] J. Ye, I. Hajirasouliha, J. Becque, and A. Eslami, “Optimum design of cold-formed steel beams using Particle Swarm Optimisation method,” *J Constr Steel Res*, vol. 122, pp. 80–93, Jul. 2016, doi: 10.1016/j.jcsr.2016.02.014.

[37] H. Parastesh, I. Hajirasouliha, H. Taji, and A. Bagheri Sabbagh, “Shape optimization of cold-formed steel beam-columns with practical and manufacturing constraints,” *J Constr Steel Res*, vol. 155, pp. 249–259, Apr. 2019, doi: 10.1016/j.jcsr.2018.12.031.

[38] L. Laím, J. Mendes, H. D. Craveiro, A. Santiago, and C. Melo, “Structural optimization of closed built-up cold-formed steel columns,” *J Constr Steel Res*, vol. 193, Jun. 2022, doi: 10.1016/j.jcsr.2022.107266.

[39] S. M. Mojtabaei, J. Becque, and I. Hajirasouliha, “Structural Size Optimization of Single and Built-Up Cold-Formed Steel Beam-Column Members,” *Journal of Structural Engineering*, vol. 147, no. 4, Apr. 2021, doi: 10.1061/(asce)st.1943-541x.0002987.

[40] D. T. Phan, ; Seyed, M. Mojtabaei, I. Hajirasouliha, ; T L Lau, and J. B. P. Lim, “Design and Optimization of Cold-Formed Steel Sections in Bolted Moment Connections Considering Bimoment,” 2020, doi: 10.1061/(ASCE)ST.1943.

[41] S. M. Mojtabaei, I. Hajirasouliha, and J. Ye, “Optimisation of cold-formed steel beams for best seismic performance in bolted moment connections,” *J Constr Steel Res*, vol. 181, Jun. 2021, doi: 10.1016/j.jcsr.2021.106621.

[42] S. J. Qadir, V. B. Nguyen, and I. Hajirasouliha, “Design optimisation for cold rolled steel beam sections with web and flange stiffeners,” *J Constr Steel Res*, vol. 213, Feb. 2024, doi: 10.1016/j.jcsr.2023.108375.

[43] C. Karthik and M. Anbarasu, “Cold-formed ferritic stainless steel closed built-up beams: Flexural behaviour and numerical parametric study,” *Thin-Walled Structures*, vol. 164, Jul. 2021, doi: 10.1016/j.tws.2021.107816.

[44] ABAQUS, “ABAQUS Analysis User’s Manual-Version 6.14–2, ABAQUS Inc,” 6.14–2.

[45] K. Roy, T. C. H. Ting, H. H. Lau, and J. B. P. Lim, “Experimental and numerical investigations on the axial capacity of cold-formed steel built-up box sections,” *J Constr Steel Res*, vol. 160, pp. 411–427, Sep. 2019, doi: 10.1016/j.jcsr.2019.05.038.

[46] Y. Dai, K. Roy, Z. Fang, G. M. Raftery, and J. B. P. Lim, “Web crippling resistance of cold-formed steel built-up box sections through experimental testing, numerical simulation and deep learning,” *Thin-Walled Structures*, vol. 192, Nov. 2023, doi: 10.1016/j.tws.2023.111190.

[47] B. W. Schafer, ; A Sarawit, and T. Peköz, “Complex Edge Stiffeners for Thin-Walled Members”, doi: 10.1061/ASCE0733-94452006132:2212, 2006.

[48] Kankanamge, Nirosha Dolamune. "Structural behaviour and design of cold-formed steel beams at elevated temperatures." PhD diss., Queensland University of Technology, Brisbane, 2010.

[49] C. Yu and B. W. Schafer, “Simulation of cold-formed steel beams in local and distortional buckling with applications to the direct strength method,” *J Constr Steel Res*, vol. 63, no. 5, pp. 581–590, May 2007, doi: 10.1016/j.jcsr.2006.07.008.

[50] N. Dolamune Kankanamge and M. Mahendran, “Behaviour and design of cold-formed steel beams subject to lateraltorsional buckling,” *Thin-Walled Structures*, vol. 51, pp. 25–38, Feb. 2012, doi: 10.1016/j.tws.2011.10.012.

Appendix "A" – Coupon testing for material properties

To determine the material properties of the samples provided coupon testing was conducted, and the results were used to carry out the parametric study as mentioned in the Chapter 5. The details of the Instron machine are provided in the Figure A-1. The deformed shape of the coupon samples is shown in the Figure A-2.

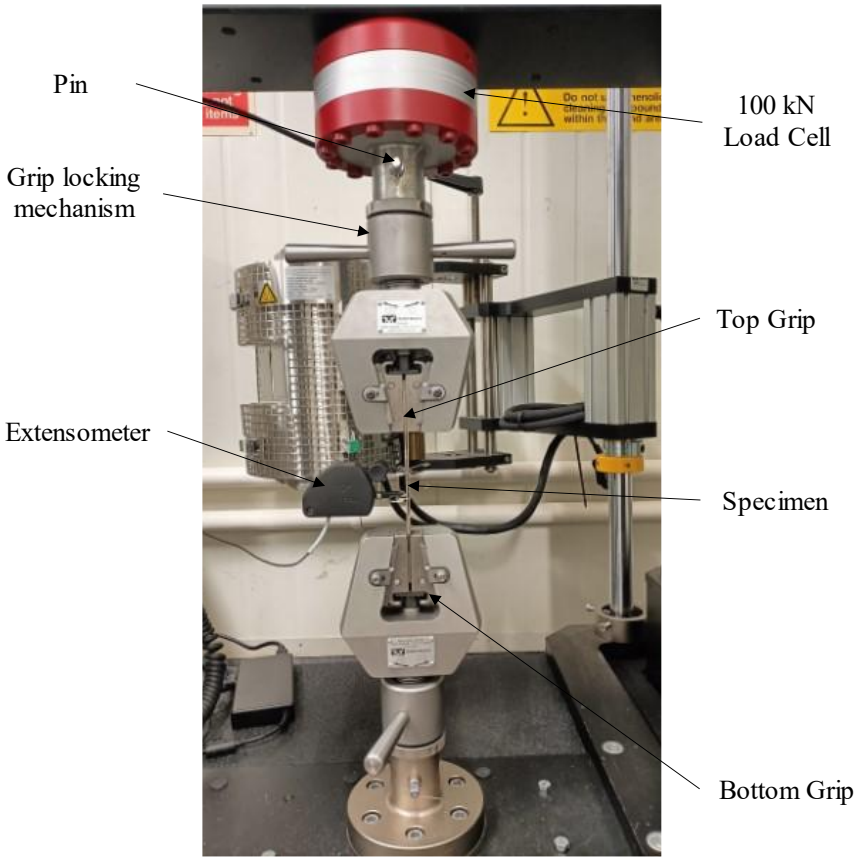

Figure A-1: Instron testing machine

Figure A-2: Deformed shape of the coupons

Material properties obtained from the coupon testing can be seen in the Figure A-3.

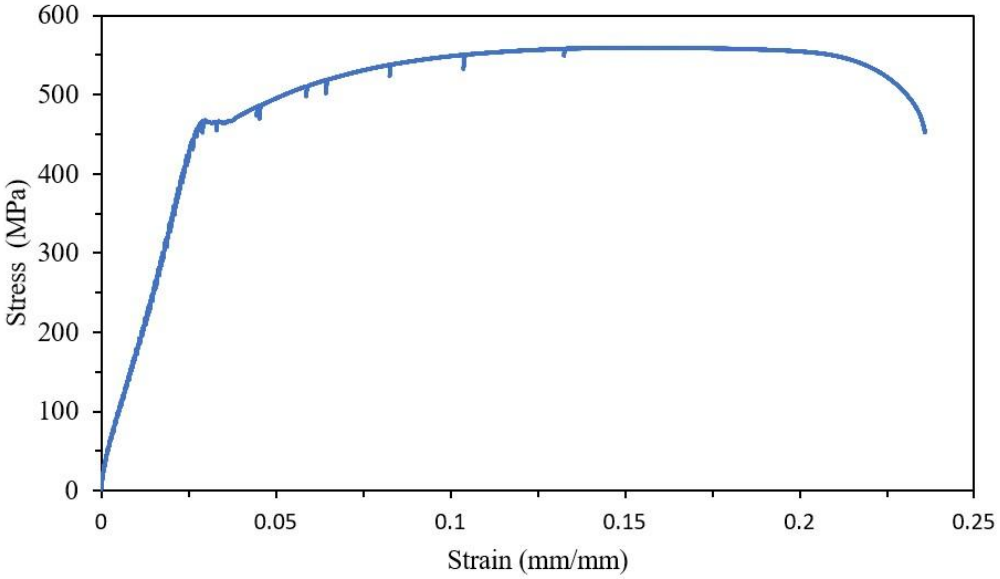

Figure A-3: Stress-strain curve from the coupon testing

Appendix "B" – Python scripts

B.1 Flow chart for the post-processing of data

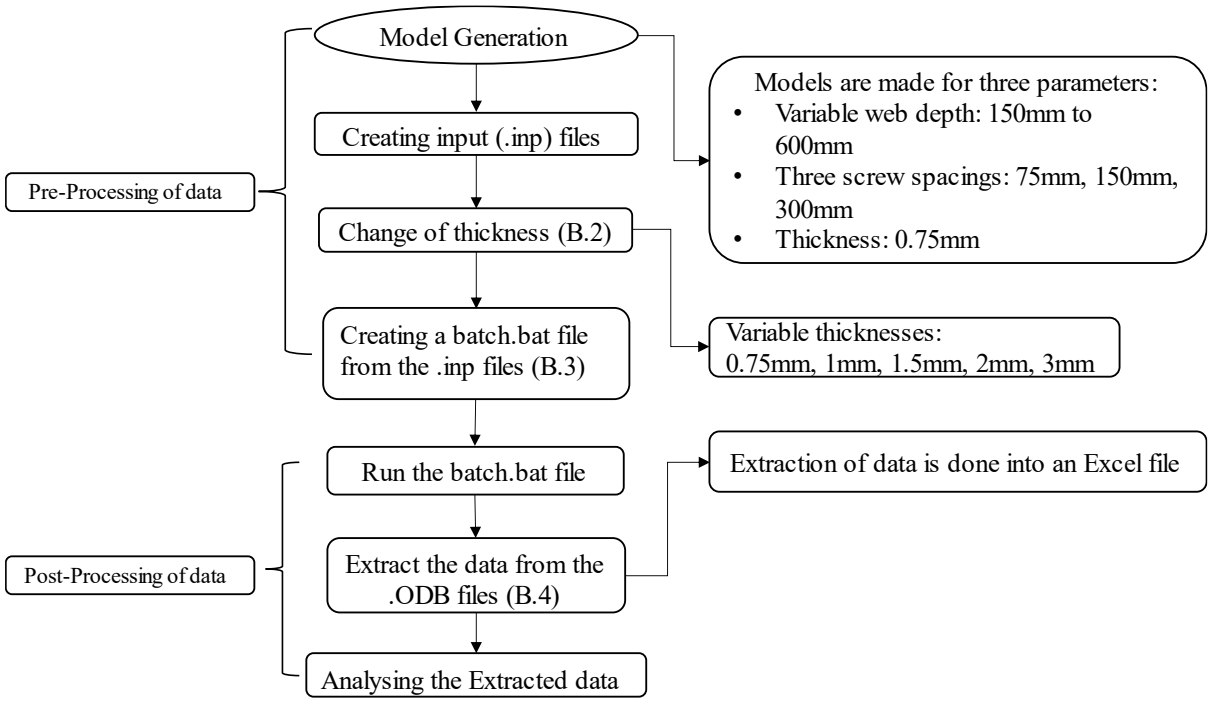

Figure B-1: Flowchart used for model generation and data extraction

B.2 Python script for changing the thickness of the built-up sections for conducting a parametric study

```
import os

# Get the current directory where the script is located
current_folder = os.path.dirname(os.path.abspath(__file__))

# Get all .inp files in the directory
inp_files = [file for file in os.listdir(current_folder) if file.endswith(".inp")]

if inp_files:
    for inp_file in inp_files:
        inp_path = os.path.join(current_folder, inp_file)

        # Read the file content
        with open(inp_path, 'r') as file:
            lines = file.readlines()

        # Prepare the lines to search and replace
        search_lines = [
            "*Shell Section, elset=_PickedSet7, material=Steel\n",
            "2., 5\n"  #Replace with thickness that is to be changed
```

```
        ]
        replace_lines = [
            "*Shell Section, elset=_PickedSet7, material=Steel\n",
            "1., 5\n" #Replace with thickness that is required
        ]

        # Replace the lines if found
        with open(inp_path, 'w') as file:
            i = 0
            while i < len(lines):
                if lines[i:i + len(search_lines)] == search_lines:
                    file.writelines(replace_lines)
                    i += len(search_lines)
                else:
                    file.write(lines[i])
                    i += 1

        print(f"File '{inp_file}' has been updated.")
else:
    print("No .inp files found in the directory.")


print("completed")
```

B.3 Python script for creating batch files

```
# This code takes the ABAQUS input files and generates the batch file.

# File paths
commands_text_file = r'Command.txt'
commands_batch_file = r'Batch.bat'

# Range of job numbers
start = 2
end = 121

# Generate the commands text file
with open(commands_text_file, 'w') as file:
    for i in range(start, end + 1):
        if i<10:
            file.write(f'call abaqus job={i:03} cpus=4 int\n')
        elif 10<=i<100:
            file.write(f'call abaqus job={i:04} cpus=4 int\n')
        else:
            file.write(f'call abaqus job={i:05} cpus=4 int\n')

print("Commands text file generated successfully.")

# Convert the text file to a batch file
```

```
with open(commands_text_file, 'r') as text_file:
    with open(commands_batch_file, 'w') as batch_file:
        batch_file.write('@echo off\n')
        for line in text_file:
            batch_file.write(line)

print("Batch file created successfully.")
```

B.4 Python script for extracting the data from the Output Database (.odb) file

```
import re
import openpyxl

def extract_maximum_value(file_path):
    max_value = float('-inf')
    read_values = False

    with open(file_path, 'r') as file:
        for line in file:
            line = line.strip()
            if line.startswith('MAXIMUM'):
                max_value_line = re.search(r'MAXIMUM\s+(-?\d+\.?\d*(?:[Ee][+-]?\d+)?)',
line)
                if max_value_line:
                    max_value = max(max_value, abs(float(max_value_line.group(1))))
            elif line.startswith('NODE'):
                read_values = True
            elif read_values:
                value_match = re.search(r'-?\d+\.?\d*(?:[Ee][+-]?\d+)?', line)
                if value_match:
                    value = abs(float(value_match.group()))
                    max_value = max(max_value, value)
                else:
                    read_values = False

    return max_value

# Range of files to process
start = 2
end = 121

# Create a new Excel workbook and sheet
wb = openpyxl.Workbook()
sheet = wb.active

# Set the header
sheet.cell(row=1, column=1, value="File")
sheet.cell(row=1, column=2, value="Maximum Value")
```

```
# Process each file in the range
for file_num in range(start, end + 1):
    if file_num < 10:
        file_path = fr'Z:\Arthur_study\Ryan\6.ShearModels\1.N500\\{file_num:03}.dat'
        max_value = extract_maximum_value(file_path)
    elif 10 <= file_num < 100:
        file_path = fr'Z:\Arthur_study\Ryan\6.ShearModels\1.N500\\{file_num:04}.dat'
        max_value = extract_maximum_value(file_path)
    else:
        file_path = fr'Z:\Arthur_study\Ryan\6.ShearModels\1.N500\\{file_num:05}.dat'
        max_value = extract_maximum_value(file_path)

    # Write file number and maximum value to Excel
    row = file_num - start + 2
    sheet.cell(row=row, column=1, value=f"{file_num:03}")
    sheet.cell(row=row, column=2, value=max_value / 1000000)

# Save the workbook
wb.save(r"Z:\Arthur_study\Ryan\6.ShearModels\1.N500\\Compressive_strength1.xlsx")
print("Extraction completed and saved to 'Compressive_strength1.xlsx'.")
```